

The Quantum Walk Microscope

Dissertation

zur
Erlangung des Doktorgrades (Dr. rer. nat.)
der
Mathematisch-Naturwissenschaftlichen Fakultät
der
Rheinischen Friedrich-Wilhelms-Universität Bonn

vorgelegt von

Stefan Brakhane

aus
Alhausen



Bonn, 2016-09-26

Angefertigt mit Genehmigung
der Mathematisch-Naturwissenschaftlichen Fakultät
der Rheinischen Friedrich-Wilhelms-Universität Bonn

1. Gutachter: Prof. Dr. Dieter Meschede
2. Gutachter: Prof. Dr. Stefan Linden

Tag der Promotion: —

Erscheinungsjahr: 2016

Contents

1. Introduction	3
2. Ultra-High Vacuum Chamber With Ultra-Low Birefringence Glass Cell	5
2.1. A Small Prelude on Birefringence	5
2.2. Vacuum Apparatus	8
2.3. Ultra-Low Birefringence Glass Cell	11
2.3.1. Manufacturing of the Cell	11
2.3.2. Characterizing the Vacuum Properties	14
2.3.3. Determining the Optical Properties	15
2.4. Vacuum Window	18
2.5. Long-Term Vacuum Pressure	19
3. Control of Magnetic Fields and Magneto-Optical Trapping	21
3.1. Magnetic Shielding	23
3.1.1. Design and Simulation	23
3.1.2. Ion Pump Shielding	26
3.2. Magnetic Coils	27
3.2.1. Compensation Coils	27
3.2.2. Gradient Coils	27
3.3. Magneto-Optical Trapping of Cesium Atoms	30
3.3.1. Laser Sources	30
3.3.2. Beam Shaping	32
3.3.3. Discussion: Two-Color Magneto-Optical Trapping	35
3.3.4. Cooling and Trapping of Atoms	35
4. Fluorescence Imaging of Atoms in a 3D Optical Lattice	39
4.1. Development of a High Numerical Aperture Objective Lens	40
4.1.1. Optical Design	40
4.1.2. Mechanical Design	41
4.1.3. Clean Room Assembly	42
4.1.4. Optical Characterization	43
4.2. Optical Setup to Image Individual Atoms	45
4.2.1. Optical Lattice Setup	45
4.2.2. Illumination Setup	48
4.3. Fluorescence Imaging of Atoms	48
4.3.1. Determining the Position of Single Atoms	49
4.3.2. Analyzing the Point Spread Function with Pictures of Single Atoms	51
4.3.3. Outlook: Selecting a Single Plane of Atoms	55

4.4.	Characterization of the Optical Lattice	57
4.4.1.	Detection Precision	57
4.4.2.	Tilt and Spacings	58
4.5.	Detecting the Occupation of Lattice Sites	61
4.5.1.	Horizontal Drifts of the Optical Lattice	63
4.6.	Storage Time of Atoms in a 3D Optical Lattice	64
5.	State-Dependent Transport in Two Dimensions	67
5.1.	State-Dependent Transport Revisited	67
5.1.1.	Optical Dipole Potentials	67
5.1.2.	State-Dependent Transport in One Dimension	69
5.2.	State-Dependent Transport in Two Dimensions	71
5.2.1.	Potential Depth and Trap Frequencies	73
5.2.2.	Distortions of the Optical Lattice	74
5.2.3.	Alternative Scheme: Perpendicularly-Oriented Quantization Axis	79
5.3.	State-Dependent Transport in Three Dimensions	80
5.4.	Technical Implementation of the Polarization Synthesis	82
6.	Conclusion and Outlook	85
6.1.	Atoms as Qubits	85
6.1.1.	Population Relaxation Time	85
6.1.2.	Microwave Driven Transitions	86
6.2.	Addressing Individual Atoms	87
6.3.	Vibrational Ground State Cooling	87
6.4.	Quantum Simulation Enabled by Quantum Walks in Two Dimensions	88
6.4.1.	Topologically Protected Edge States	88
6.4.2.	Artificial Magnetic Fields	89
A.	Error Propagation	91
B.	Personal Additions to the Laboratory Infrastructure	93
B.1.	Computer Control	93
B.2.	Power Meter	96
B.3.	Temperature Interlock	97
B.4.	Window Comparator	98
B.5.	Controlled Vacuum Baking	99
B.6.	Circuit for Plasma Cleaning	101
B.7.	Amplifier Box for Fast Photodiode	103
B.8.	Modulation Board for Interference Filter Laser	105

Abstract

In this thesis, I present single-site detection of neutral atoms stored in a three-dimensional optical lattice using a numerical aperture objective lens ($\text{NA}_{\text{design}} = 0.92$). The combination of high-resolution imaging with state-dependent trapping along two-direction of the lattice opens up the path towards quantum simulations via quantum walks. Suppressing the interactions of a quantum system with the environment is essential for all quantum simulation experiments. It demands a precise control of both the external magnetic (stray) fields and the polarization properties of laser beams inside the vacuum chamber. I designed a metal shielding to reduce magnetic field fluctuations and designed, assembled and characterized a novel ultra-high vacuum glass cell. The glass cell consists of special glass material and exhibits an ultra-low birefringence Δn of a few times 10^{-8} to highly suppress polarization disturbances originating from stress birefringence in vacuum windows. Furthermore, anti-reflection coatings avoid reflections on all window surfaces. The cell hosts the assembled vacuum-compatible objective, that exhibits a diffraction limited resolution of up to 453 nm and allows to optically resolve the spacing of the optical lattice. Fluorescence images of single trapped atoms are used to characterize the imaging system. The filling, orientation and geometry of the optical lattice is precisely reconstructed using positions of atoms that can be determined from fluorescence images. Furthermore, I present a scheme to realize state-dependent transport and discuss its robustness against experimental imperfections in a technical implementation. This transport scheme enable the realization of discrete-time quantum walks with neutral atoms in two dimensions. These quantum walks pave the way towards the simulation of artificial magnetic fields and topologically protected edge states.

Parts of this thesis have been published in the following articles:

- S. Brakhane and A. Alberti, *Technical Note: Stress-Induced Birefringence in Vacuum Systems*, available online (June, 2016)
- T. Groh, S. Brakhane, W. Alt, D. Meschede, J. Asbóth and A. Alberti, *Robustness of topologically protected edge states in quantum walk experiments with neutral atoms*, *Physical Review A* **94**, 013620 (2016)
- S. Brakhane, W. Alt, D. Meschede, C. Robens, G. Moon and A. Alberti, *Ultra-low birefringence dodecagonal vacuum glass cell*, *Rev. Sci. Instrum.* **86**, 126108 (2015)
- S. Brakhane, W. Alt, D. Meschede, C. Robens and A. Alberti, *Polarisationserhaltende Vakuum-Zelle zur Anwendung oder Messung elektromagnetischer Wellen im Vakuum*, Patent pending, (2015)

Zusammenfassung

Die vorliegende Arbeit berichtet über die Erkennung von neutralen Atomen in einem zweidimensionalen, zustandsabhängigen optischen Gitter mit Einzelplatzauflösung, welche durch ein vakuumkompatibles Objektiv hoher numerischer Apertur ermöglicht wird. Es findet Einsatz im Bereich der Quantensimulation, wo ein besonderes Augenmerk auf einer effektiven Unterdrückung der Wechselwirkung eines Quantensystems mit seiner Umgebung gerichtet ist. Dabei ist, unter anderem, die Kontrolle über magnetische (Streu-) Felder und über die Polarisation von Laserlicht innerhalb der Vakuumkammer von entscheidender Bedeutung.

Aus diesem Grund ist von mir sowohl eine magnetische Abschirmung zur Unterdrückung magnetischer Feldfluktuationen konstruiert worden als auch eine polarisationserhaltende Vakuumzelle mit äußerst geringer Doppelbrechung (Δn im Bereich von 10^{-8}) ausgelegt, konstruiert und produziert worden. Dadurch konnten Abweichungen der Polarisation durch (spannungsinduzierte) Doppelbrechung im Glas des Vakuumfensters vermieden werden. Zudem sind störende Reflexion an Glasoberflächen weitestgehend durch optische Beschichtungen abgeschwächt.

Das Objektiv hoher numerischer Apertur ist an das Deckglas der Glaszelle geflanscht und ermöglicht ein beugungslimitiertes Auflösungsvermögen von bis zu 453 nm, womit die beiden Gitterkonstanten der optischen Falle optisch aufgelöst werden können. Selbst ohne genaue Kenntnis der Punktspreizfunktion des Abbildungssystems ist damit eine präzise Bestimmung der optischen Gitterparameter (z.B. Gitterkonstante, Orientierung, Belegung mit Atomen) über eine Positionsbestimmung der Atome in einer Fluoreszenzaufnahme möglich. Die Fluoreszenzaufnahmen erlauben es zusätzlich das optische Mikroskop zu charakterisieren.

Weiterhin, wird in dieser Arbeit ein Schema zum zweidimensionalen, zustandsabhängigen Transport neutraler Atome vorgestellt und im Hinblick auf Toleranzen einer technischen Umsetzung untersucht.

Der deterministische, zustandsabhängige Transport gestattet uns „Quantenwalks“ mit einzelnen neutralen Atome durchzuführen, die eine Möglichkeit schaffen künstliche Magnetfelder oder topologisch geschützte Randzustände zu untersuchen.

1. Introduction

Today's quantum technologies are no longer an exclusive playground for scientists but they offer the premise of having strong technological influence on society [1]: Among these are a fundamentally secure encryption, sensors with unprecedented sensitivity, quantum computers for solving hard problems and quantum simulators for the understanding of nature. Recently, the importance of quantum technologies has been recognized by various national and international funding agencies leading to a dramatic increase in research programs. These programs aim to strengthen fundamental science and to advance existing proof of principle experiments to commercial products [2–6].

For physicists, quantum computers and simulators offer the opportunity to gain insight into multi-particle quantum systems which are fundamentally not accessible by classical computers due to the exponential scaling of the Hilbert space with the number of constituents [7]. Since the universal quantum computer is still not available, one can use a well controlled quantum system to simulate a mathematically similar – but physically different – quantum system [8]. Proof of principle experiments on quantum simulation have already been achieved in various systems, e.g. photons [9], ions [10], solid state systems [11], and neutral atoms in optical lattices [12] where a typical solid state electron tunneling Hamiltonian is naturally realized. The time evolution of a quantum system is typically simulated [10] by either using qubits and gate operations with a Trotter expansion (digital quantum simulator) or by mimicking a Hamiltonian via tweaking external tuning parameters of a similar well-controlled system (analog quantum simulator).

In contrast, our idea to realize quantum simulations consists in the use of a quantum walk, i.e. the quantum analog of classical random walks. Quantum walks offer the benefit of a quadratically faster information spread due to multi-path interference effects [13]. Thus, they are ideal candidates to explore a wide range of interesting physics, including transport phenomena [14], novel topological effects [15] and quantum computation [16,17]. A physical realization of quantum walks has already been achieved in quantum systems consisting of neutral atoms in state-dependent optical lattices [18–20], photons [21,22], and trapped ions [23,24]. A quantum walk is characterized by at least two operations: a coin and a shift. A coin creates a superposition of internal states while a shift translates parts of the wavefunction conditioned on the internal state into different (spatial) directions. In our group, we realize quantum walks with neutral atoms in polarization synthesized optical lattices which enable state-dependent transport [18,25–27].

Within this thesis I will present a new apparatus for the realization of quantum walks in two spatial dimensions. Unlike other optical lattice experiments [19,28], the transport employed in our group is fully deterministic and does not depend on tunneling. In order to gain information of our system, we need to determine the state and position of atoms in the optical lattice. Recent advances in the imaging of atoms in optical lattices allow for single-site detection in lattices with a spacing around the imaging wavelength

[19, 29–33]. While a medium numerical aperture system is sufficient to detect atoms in a 1D optical lattice using super-resolution techniques [34, 35], it obeys the shortcoming of a relatively long exposure time due to the low number of collected photons. In addition, the corresponding low optical resolution limits the minimal size of projected light patterns onto the atoms [15].

Besides detection, all experiments dealing with quantum systems face the challenge to enable state initialization and detection of all particles, as well as controlling interactions between them. At the same time unintentional interactions with the environment need to be kept at an absolute minimum to guarantee long coherence times of the system.

The predominant sources of decoherence affecting optical lattice experiments are discussed in references [36–38]. Among them are magnetic field fluctuations and temporal variations in the lattice intensity which can arise from laser instabilities and from changes of the polarization state of light. In a strong three-dimensional confinement, ground state cooling [27, 39] is – in principle – able to suppress these effects and to enhance coherence times in the system.

The outline of this thesis is as follows: In chapter 2, I will present the vacuum system of our experimental apparatus including the design, construction and characterization of a ultra-high vacuum cell exhibiting an ultra-low birefringence in order to avoid the distortion of light polarization. To reduce decoherence, the suppression of magnetic fields via a metal shielding and simulations of magnetic field distribution of various coil systems will be discussed in chapter 3. Furthermore, cooling and trapping of neutral atoms in a magneto-optical trap in close proximity to a high numerical aperture objective lens will be demonstrated. These atoms serve as a source of cold atoms for this optical lattice experiment. In chapter 4, I will investigate how to image single atoms in a three-dimensional optical lattice with a high-resolution microscope featuring an objective lens with the highest numerical aperture in the field of cold atoms physics. The imaging system will allow us to determine the position of atoms with high precision and to extract important lattice parameters. A new scheme and a possible experimental implementation of a state-dependent transport in an effective two-dimensional optical lattice system will be presented in chapter 5. In the future, these tools will finally allow us to realize 2D discrete quantum walks utilizing neutral atoms and to achieve quantum simulations with quantum walk, see chapter 6.

2. Ultra-High Vacuum Chamber With Ultra-Low Birefringence Glass Cell

Every modern experiment designed for the investigation of cold atom ensembles needs to fulfill the requirement of trapping atoms in an isolated environment in which unintentional interactions between the atoms and the environment are suppressed. Above all the atom densities need to be kept low such that scattering events with other background atoms are unlikely to occur. At the same time, the density needs to be large enough to efficiently collect atoms from the background gas as a source of desired atoms for the experiment. Typical pressures in experiments with Bose-Einstein condensates reach values of 1×10^{-11} mbar which is similar to the pressure in the interaction regions of the Large Hadron Collider [40].

In addition, a very large optical access to the chamber is highly desirable since these experiments typically require a large number of separated beams for cooling and trapping, as well as for the manipulation of the internal states of (individual) atoms [28]. For the regions of optical access it is of utmost importance that the properties of the transmitted laser and light beams – such as the wavefront quality and the state of polarization – are preserved [41, 42]: Wavefront distortion degrades the resolution for optical imaging and cause aberrations to the shape of optical potentials. A distortion of the polarization state of light can lead to a decrease in the preparation fidelity of quantum states [43] and can induce differential as well as vector tensor light shifts [44, 45] which limit the precision and coherence properties of state of the art experiments in quantum optics.

In our case, a birefringence need to be suppressed to reduce decoherence effects during transport operations of neutral atoms in state-dependent in a optical lattice (see chapter 5). I will present a compact epoxy-bonded glass cell made of SF57 glass that exhibits ultra-low birefringence and is compatible with ultra-high vacuum as presented in reference [46]. Furthermore, it allows for large optical access from up to twelve radial directions with optical coatings on all window surfaces and it enables hosting of a high-resolution objective.

2.1. A Small Prelude on Birefringence

Unlike in crystals, such as calcite, where the birefringence is caused by the atomic lattice structure itself, ideal glasses are isotropic and do not exhibit birefringence. However, mechanical stress induces inhomogeneous birefringence in the glass material, as shown in figure 2.1(a). In general, the amount of birefringence is a function of the glass annealing conditions, external forces, and glass type. Commercially available optical glasses undergo an annealing process [47] that reduces the temperature gradients in the material to a minimum in order to suppress the internal stress.

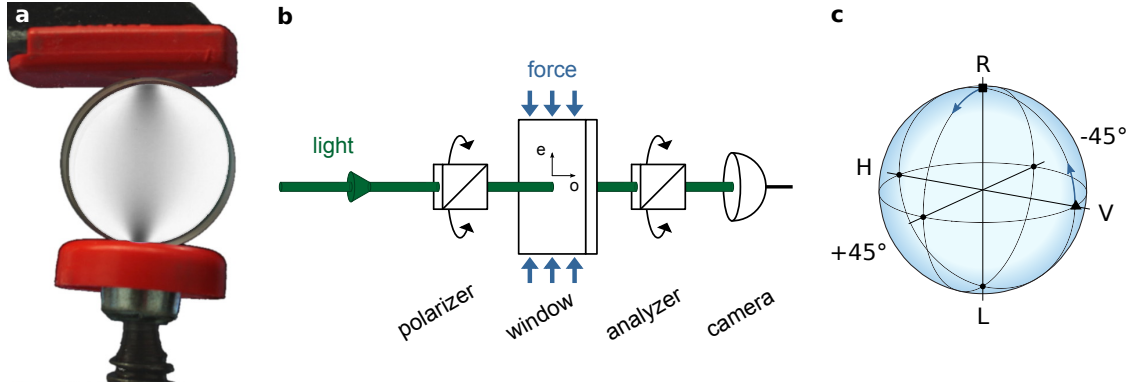


Figure 2.1.: Picture (a) and setup (b) of stress birefringence inside a N-BK7 glass window. The image is recorded using homogeneous linear polarized light which passes through the sample and an analyzer. Dark areas in the glass correspond to regions of strong birefringence whereas bright areas indicate low birefringence. (c) Poincaré sphere as a visualization of the polarization state of light.

External forces originate from mounting screws, the pressure difference between the inside and outside of the chamber as well as unmatched expansion coefficients of the glass window and the metal flange of the vacuum system. To reduce the birefringence, properly annealed gaskets made of copper or indium in combination with low clamping forces should be used to match the thermal expansion coefficients of the glass and the viewport flanges. While indium has the advantage of requiring lower clamping forces than copper, its melting point around $150\text{ }^{\circ}\text{C}$ limits its application to systems that do not depend on high bake-out temperatures. In addition, the thermal expansion coefficients of flange material and window should be matched. If necessary, this can be done by inserting intermediate materials of different thermal expansion coefficient.

The differential mechanical shear stress $\sigma = \sigma_o - \sigma_e$ within the glass converts into a birefringence Δn by a material dependent proportional constant called stress-optical coefficient K

$$\Delta n = K \times \sigma \quad (2.1)$$

Here, the birefringence $\Delta n = |n_o - n_e|$ is defined as the difference in the refractive index of the ordinary and extraordinary beam which correspond to the normal and colinear direction of the stress tensor and can be identified with the two polarization axes of uniaxial crystals. Typical values for K are in the order of $1 \times 10^{-6} \text{ mm}^2/\text{N}$ and show a weak dependence on wavelength and temperature.

According to ISO 10110-2 [48], stress birefringence for optical components is specified by

$$\Delta n = \text{OPD}/L \quad (2.2)$$

in units of $[\text{nm}/\text{cm}]$ where OPD denotes the relative optical path difference between ordinary and extraordinary beam and L the thickness of the sample. The technical standard also defines classes of permissible stress birefringence values for typical applications such

as polarization or interference instruments ($< 2 \text{ nm/cm}$), precision or astronomical optics ($< 5 \text{ nm/cm}$), and photographic or microscope optics ($< 10 \text{ nm/cm}$).

Typical values for the birefringence of commercially available vacuum windows are 10^{-6} (20 nm/cm) and 10^{-7} (2 nm/cm) for well annealed vacuum glass cells [49]. The latter barely reaches the value recommended by ISO 10110-2 [48] for interference instruments. However, while distortions of the wavefront are typically specified in commercial products, there is, to our knowledge, no specification available for any commercially available glass cell or vacuum viewport in terms of birefringence.

The measurement of the extinction ratio η allows a precise determination of the birefringence as well as of the orientation of the optic axes (see section 2.3.3). This ratio is defined as $\eta = P_{\min}/P_{\max}$, where the minimum power (P_{\min}) and maximum power (P_{\max}) of a transmitted laser beam are recorded for a full rotation of the analyzer. This measurement is based on a setup where the device under test is placed between a polarizer and an analyzer as shown in figure 2.1(b).

The extinction ratio is expected to vanish when the polarizer, and thus the linear input polarization, is exactly aligned to one of the polarization axes of the material. The maximum value of the extinction ratio is instead observed when the polarizer is aligned under 45° , which corresponds to an equal splitting of the input power onto the two axes. The birefringence is given by the amplitude variation $\Delta\eta$ of the extinction ratio for different angles of the input polarizer whereas the axes are given by the angle at which the extinction ratio is minimum or maximum. In the case of small birefringence, we have

$$\Delta n \approx 2\sqrt{\Delta\eta}/(kL), \quad (2.3)$$

where $k = 2\pi/\lambda$ is the wave vector of light showing the quadratic dependence of the signal amplitude $\Delta\eta$ on the birefringence [46]. Measured extinction ratios are in most cases limited to 10^{-7} due to imperfections of the polarizers and inhomogeneities in the substrate material.

Some types of dense flint glass show a value for the stress optical coefficient that are two orders of magnitude smaller than these of commonly used glasses: N-BK7 or Pyrex. Using these glass types, it is possible to enter the regime of ultra-low birefringence below 10^{-8} (0.2 nm/cm) even for the complex geometry of the vacuum cell, see section 2.3.

What does this amount of stress birefringence mean for practical purposes? Assume that we want to transmit a perfectly right-handed circularly polarized light beam through a standard vacuum viewport exhibiting a birefringence of $\Delta n = 20 \text{ nm/cm}$ (at a wavelength of $\lambda = 852 \text{ nm}$) and a thickness of $L = 5 \text{ mm}$. Due to the birefringence, the polarization acquires a slight change in ellipticity. A widely used figure of merit to quantify the distortion from pure circular polarization is the polarization purity

$$\Pi \equiv \frac{P_{\text{rh}}}{P_{\text{lh}}}, \quad (2.4)$$

defined as the power ratio between right-handed (P_{rh}) and left-handed polarization (P_{lh}). In the case of an initially circular polarization, it can be shown that

$$\Pi = \frac{1}{\Delta\eta} \approx \left(\frac{\lambda}{\pi \Delta n L} \right)^2, \quad (2.5)$$

which yields a value of $\sim 3 \times 10^3$ for our example. Thus, a perfectly circular polarized input beam with 1 mW power exhibits an unwanted circular component of 330 nW after the window. In quantum optics, this amount of power in the wrong polarization mode is already sufficient to considerably reduce the fidelity of quantum state manipulations. In contrast, using the ultra-low birefringence vacuum glass cell respectively, this value is correspondingly reduced by four orders of magnitude down to 33 pW.

Another way often employed to characterize circular polarization is to measure the contrast

$$C \equiv \frac{P_{\max} - P_{\min}}{P_{\max} + P_{\min}} = 2 \frac{\sqrt{\Delta\eta}}{1 + \Delta\eta} \quad (2.6)$$

by determining the minimum P_{\min} and maximum power P_{\max} behind a rotating analyzer, likewise as for the extinction measurement of linear polarization.

The effect of a retardance due to stress birefringence can also be visualized on the Poincaré sphere, see figure 2.1(c), where circular polarization is geometrically represented by points at the poles and all possible linear polarizations are mapped onto the great circle at the equator. A small amount of birefringence rotates the circular polarization of light (square) closer to the equatorial plane bestowing a slight change in ellipticity on the polarization state. For thin vacuum windows (i.e. no optical activity), the corresponding rotation axis is located in the equatorial plane with an angle that is given by the direction of the stress tensors. The same effect occurs in the case of linear polarized light (triangel), where the rotation results in a movement out of the horizontal plane which also indicates a slight change in ellipticity. For small birefringence the rotation angle α is given by

$$\alpha \approx 2\sqrt{\Delta\eta}. \quad (2.7)$$

Spatially inhomogeneous stress birefringence results in a different amount of rotations depending on the position, which obviously cannot be compensated by additional homogeneous wave plates. While it is in principle possible to compensate spatially inhomogeneous birefringence, it is highly demanding under realistic conditions, since the vacuum viewports or cell windows would need to be individually characterized over the desired area. As we have seen, stress birefringence in vacuum glass viewports or glass cells needs to be considered during the design phase of an experiment when a high polarization purity is required. A later compensation of the birefringence is not feasible due to the inherent inhomogeneity of the stress tensor and to the demanding requirements for its accurate determination under vacuum.

2.2. Vacuum Apparatus

In cold atoms physics, the standard procedure to achieve a ultra-high vacuum environment with large optical access is to combine of a metal vacuum chamber with single viewports or, as an alternative, with a single glass cell. Both approaches suffer from birefringence caused by clamping forces and the pressure difference inside and outside the chamber. However, special procedures have been developed to reduce the mounting forces of the viewport [50–52] or the use of glass materials with extremely low stress-optical coefficients [53].

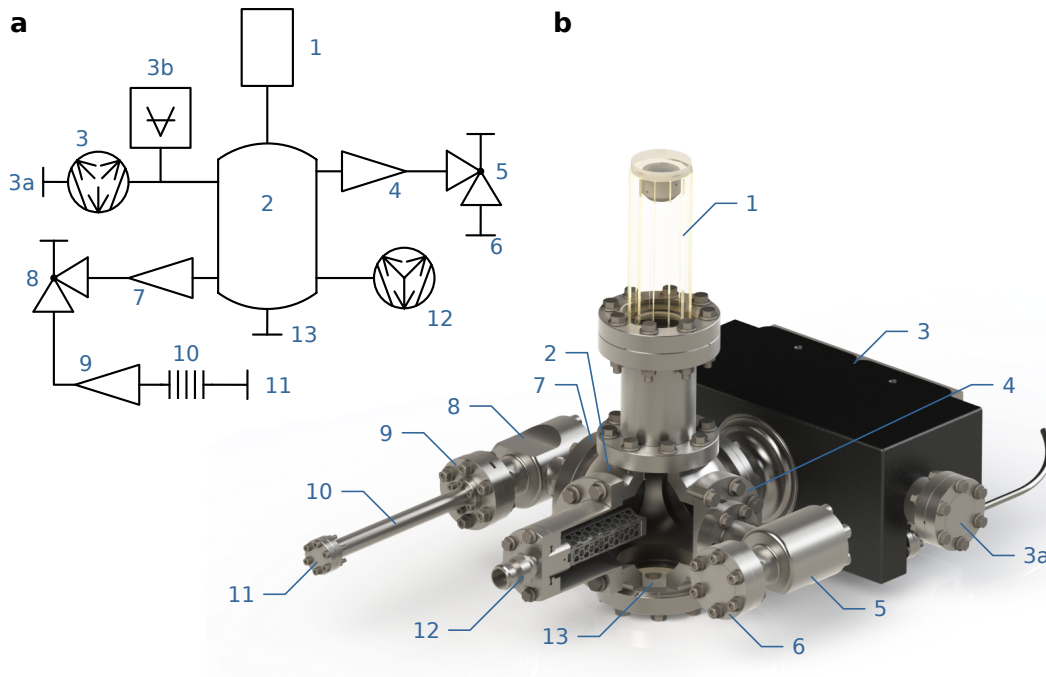


Figure 2.2.: Schematic (a) and rendering picture (b) of the vacuum chamber with additional opening. The chamber consists of the glass cell (1), a vacuum cube (2), an ion pump with side port (3a) and pressure reading (3b), a non-evaporable getter pump (12), reducers (4,7,9) and all-metal edge-valves (5,8) to connect to an external turbo molecular pump during preparation and to separate the cesium reservoir which is placed inside a small beatable bellow (10). Residual openings are closed by blind flanges (11,6) The total height of the system amounts to approximately 50 cm.

It has been reported in the literature [49] that vacuum glass cells exhibit less birefringence resulting from careful tempering during production and the use of a tubing to interconnect the glass cell with the metal flange where mounting forces are applied.

Glass cells are also widely used because of their compact geometry and their electromagnetic properties, which allows them to be used in the cases where strong magnetic fields [54] and field gradient [19] need to be switched on short time scales. The typical glass cell is produced by diffusion bonding of individual windows [55] – a process that prohibits the use of optical coating before the assembly due to the high temperatures during fusion. As a result, only surfaces at the outside of the cell can later be refined with an optically coating. Here, reflection may lead to stray light for optical imaging and additional standing waves resulting in a modulation of the lattice potentials which is highly undesirable for optical lattice experiments.

Just recently, a new technique has been developed to overcome the temperature limitation for the optical coating by a special surface treatment [56] and glass cells made by a new bonding method (optical contact [57,58]) have become commercially available. The first method employs nanostructures on the glass surface to achieve impedance match-

ing between air (or vacuum) and the glass material to suppress reflections over a large wavelength range [56]. Optical contact, on the other hand, requires the contact surfaces to be polished to highest precision and demands for a profound mechanical alignment of all constituents to form a leak tight cell. So far, optical contact has only been applied for glass cells up to eight facets using glass types like Pyrex or Sapphire. Still, both techniques are rather cost intensive.

For our chamber, we use a compact glass cell with large optical access that exhibits ultra-low birefringence and is compatible with ultra-high vacuum as presented in the next section. The glass cell is attached via an intermediate pipe to the main vacuum chamber (see figure 2.2) while a viewport is mounted on the opposite side of the chamber cube for optical access from the bottom. The viewport is made of the same glass material to also reduce birefringence along this direction. An ion getter pump (VacIon Plus 55 with StarCell¹) and a non-evaporable getter (NEG) pump (CapaciTorr CF35²) are attached to the cube to guarantee a vacuum pressure around 1×10^{-10} mbar. As it will be apparent later, the NEG pump is preferred due to its high pumping speed for water molecules. An external turbo molecular pumping stand (TSU 071 E³) is connected to the system through an all-metal edge-valve (Easy-close series 540⁴) for initial pumping and during bake-out. Cesium is introduced into the system by a glass ampule that is initially held in between two aluminum bars and positioned in a edge-welded bellow. The flow of atoms can be controlled via an edge-valve and heating of the cell once the ampule is successfully broken inside the established ultra-high vacuum.

A proper cleaning procedure is mandatory to achieve an ultra-high vacuum even though our chamber is not used in a particle accelerator where synchrotron radiation dramatically increases primary desorption of matter from chamber surfaces [40]. Since the vacuum pumps and the valve have been sealed and tested at the manufacturer, no further cleaning had to be performed. All other parts – except the glass cell and the viewport – were first cleaned with water and a solvent and subsequently with deionized water in an ultrasonic bath for 5 min each. In addition, all metal parts were tempered at a temperature of 1000° in a vacuum chamber to remove residual contamination. A high temperature bake-out up to 200° for the vacuum system where connections to glass components were sealed by blind flanges guaranteed cleanness and tightness of the system before the fragile glass components were attached. Care had to be taken to ensure small temporal and spatial temperatures differences at the fully assembled vacuum apparatus to a maximum temperature of 150° for two weeks up (see appendix B.5). A repeated bake-out became necessary after one of the edge-valves had to be exchanged under a helium atmosphere due to a minor leak. The helium atmosphere prevents the saturation of the activated NEG pump that might occur during exposure to gases other than noble gases.

¹Agilent Technologies, Inc.

²SAES Getters S.p.A

³Pfeiffer Vacuum GmbH

⁴VAT Germany GmbH

2.3. Ultra-Low Birefringence Glass Cell

As mentioned earlier, the cell is specially designed to fulfill the two requirements of ultra-low birefringence and ultra-high vacuum-compatibility in a compact dodecagonal cell geometry [46]. The twelve sides of the cell featuring double-sided anti-reflection coated windows are ideally suited for the application of laser beams in vacuum, e.g. optical lattice experiments where quite a few lattice and cooling beams are radially directed into the center of the cell. The SF57 glass material exhibits one of the lowest available stress-optical coefficients allowing us to construct vacuum cells with ultra-low birefringence ($\Delta n < 10^{-7}$) bonded by epoxy adhesive.

The reason for the low stress-optical coefficient arises from the fact that the refractive index for both polarization directions grows with the compressive stress while an increase in the amount of PbO leads to an asymmetric increase for both polarizations [59]. Thus, the stress-optical coefficient can be adjusted to vanish for a certain optical wavelength by varying the amount of lead oxide⁵. Furthermore, lead glasses like SF57 are particularly suited for vacuum applications due to their low permeability to hydrogen and helium [61], but care must be taken owing to their high sensitivity to temperature changes and mechanical shocks.

The use of epoxy adhesives is typically avoided in ultra-high vacuum system due to their outgassing and, even more important, due to their relatively large permeability towards water, i.e. the process of adsorption at the outer surface, diffusion through the material, and desorption at the inner surface [61, 62]. Yet, thermally-cured epoxy adhesives have been used in experiments where an atom chip encloses the vacuum chamber [63]. We find that the EpoTek H77 adhesive – which fulfills the NASA low outgassing standard (ASTM E595) and contains filling particles – yields a low water permeability as well as a lower stress-induced birefringence in the bonded glass material and is therefore well suited for vacuum glass cells.

2.3.1. Manufacturing of the Cell

The cell consists of twelve windows with a trapezoidal cross section (inner aperture size 13 mm \times 150 mm, thickness 5 mm) forming a cylinder-like structure, as shown in figure 2.3(b-c). The cylindrical structure is terminated on one side by a round cover glass (thickness 9 mm, outer diameter 56 mm) and on the other side by a glass ring of the same material (thickness 5 mm, inner diameter 40 mm, outer diameter 68 mm) that is bonded to a standard DN63CF metal flange. All glass components are polished to a surface flatness $\lambda/20$ ($\lambda = 866$ nm) and, except for the ring, offer an antireflection coating on both sides.

The cells are bonded by the slightly viscous and filled epoxy adhesive H77 that is advantageous for handling since its filling particles ensure a minimum thickness of the adhesive layer. This way, the appearance of droplets is highly reduced compared to the first gener-

⁵As a result of the directive “Restriction of Hazardous Substances Directive” issued by the European Commission [60] in 2003 and recalled in 2011, the use of lead is prohibited in commercial products. Nevertheless, lead in white glasses for use in optical application is exempted from this directive rendering the flint glass SF57 highly suited for polarization sensitive applications.

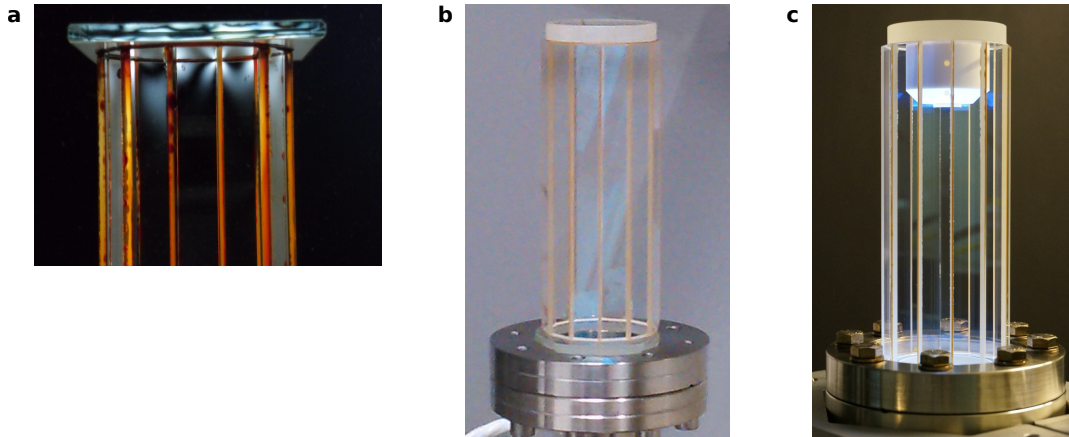


Figure 2.3.: Generations of vacuum cells: (a) A cell made of float glass showing strong birefringence; (b) SF57 glass cell attached to titanium flange; (c) SF57 glass cell attached to stainless steel flange via tantalum weld ring hosting an objective.

ation of the cell, where float glass in combination with the low viscosity adhesive EpoTek 353ND as well as its thixotropic version 353T have been applied, see figure 2.3(a). Furthermore, the H77 epoxy adhesive showed to be the best candidate for achieving low birefringence since a droplet of this adhesive caused lowest birefringence on a microscopy plate compared to the other two. A home-made, automated adhesive dispenser is used to plot a line of epoxy resin at the contact surfaces of each window in order to achieve a homogeneous and reproducible layer after contact, see figure 2.4(b). The progressive feed is set via a pulse-width modulated signal to a speed of 4 mm/s while the adhesive is extracted from a needle (diameter 0.9 mm) with a pressure of 8 bar of compressed air. The deposited line of adhesive amounts to a total volume per contact of $V = 45 \text{ mm}^3$. Small form deviations of individual windows, as well as surface roughness, are compensated by the adhesive volume such that relatively large tolerances in the glass cutting process are acceptable, leading to relatively low production costs.

During thermal curing, window glasses are supported by a special holder that guarantees the compliance with the later dodecagonal structure and exhibits a clearance at the position of the epoxy layers, see figure 2.4(a). For achieving good contact, all parts are contacted using and pushed into place by force of about 10 kN. The curing process employs a maximum temperature of 150 °C and utilizes of a slow cool down over several hours to minimize stress at the glass transition temperature of around $T_g = 80^\circ$ even though the epoxy adhesive itself can withstand temperatures up to 260 °C. The curing temperature is chosen such that its difference to the glass transition temperature amounts to a similar value as the difference between the transition temperature and the room temperature in order to limit the stress due to thermal expansion. A further reduction of the mechanical stress inside the glass material could, in principle, be realized by adhesives that are cured by ultraviolet light directly at room temperature. However, the transmittance of the glass material at the desired wavelength is low which complicates the complete curing of the adhesive at the inner side of the cell were thorough curing is mandatory to achieve a good

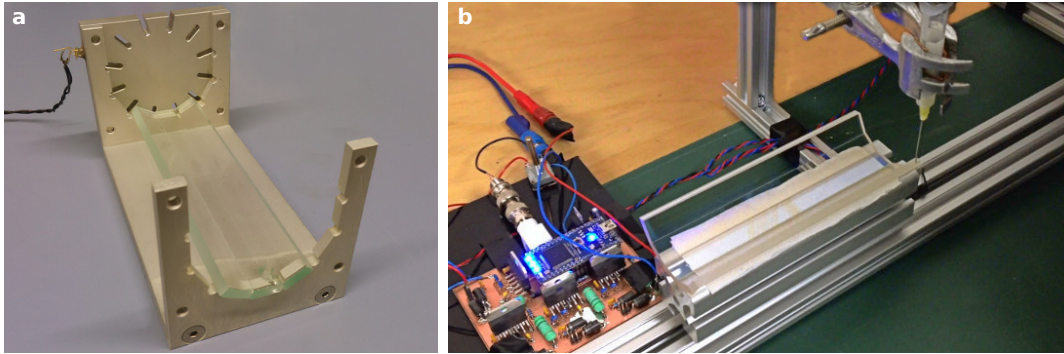


Figure 2.4.: Production utilities: (a) A holder to support the cell windows during gluing process including temperature sensor (red cable); (b) Automated deposition of adhesive using a motorized translation stage and compressed air powered nozzle (syringe) to apply the adhesive.

vacuum pressure. Optimal outgassing performance is achieved by degassing the epoxy adhesive before usage [64]. The curing process is repeated until all parts are combined to a complete cell structure following the procedure in figure 2.5.

Two different mounting procedures of the glass cell to a standard ConFlat flange are employed in this thesis for ultra-high vacuum systems. First (cell c), the glass structure (CTE⁶ $8.6 \times 10^{-6} \text{ K}^{-1}$ [65]) is glued to a commercially available non-magnetic stainless steel viewport flange (DN63CF, 316L stainless steel) featuring a tantalum weld ring (CTE $6.5 \times 10^{-6} \text{ K}^{-1}$ [66], inner diameter 48.5 mm), as shown in figure 2.3(c). The thin and relatively soft weld ring prevents the formation of critical stress levels within the glass material when the flange is deformed, e.g. during tightening of the bolts or temperature changes. For this purpose, we originally ordered a vacuum viewport from Torr Scientific, Ltd. featuring SF57 glass window and a 40 mm bore in its center, which is mounted to a tantalum lip on a stainless steel flange. However, after the assembly of the complete cell we became aware of a strong leak due to a failure of the glass to flange bonding⁷. I was able to fix this issue by detaching the metal flange from the glass structure using a high temperature of 150° and bonding both components using the H77 epoxy adhesive.

Alternatively, I manufactured a second glass cell (cell b), which is directly glued to a bored Titanium blind flange (CTE $8.4 \times 10^{-6} \text{ K}^{-1}$ [66,67]) with a hole diameter of 40 mm, see figure 2.3(b). In a first attempt to mount glass cell b on a metal flange, we used an elastomere gasket (viton) in between the glass ring of the glass cell and a stainless-steel (304) metal flange and achieved pressures down to circa 1×10^{-10} mbar after separate air-baking of the gasket. Like epoxy resin, viton gaskets are subjected to water diffusion [61]. Exchanging the elastomere gasket by a gold gasket caused a crack in the outer parts of the glass ring about two hours after sealing due to the required high clamping forces of about 150 N/mm. However, one of the cracks is continuously guided from one glass part

⁶Coefficient of Thermal Expansion

⁷The type of the white bonding substance is still unknown due to an insufficient information exchange from the manufacturer of the viewport.

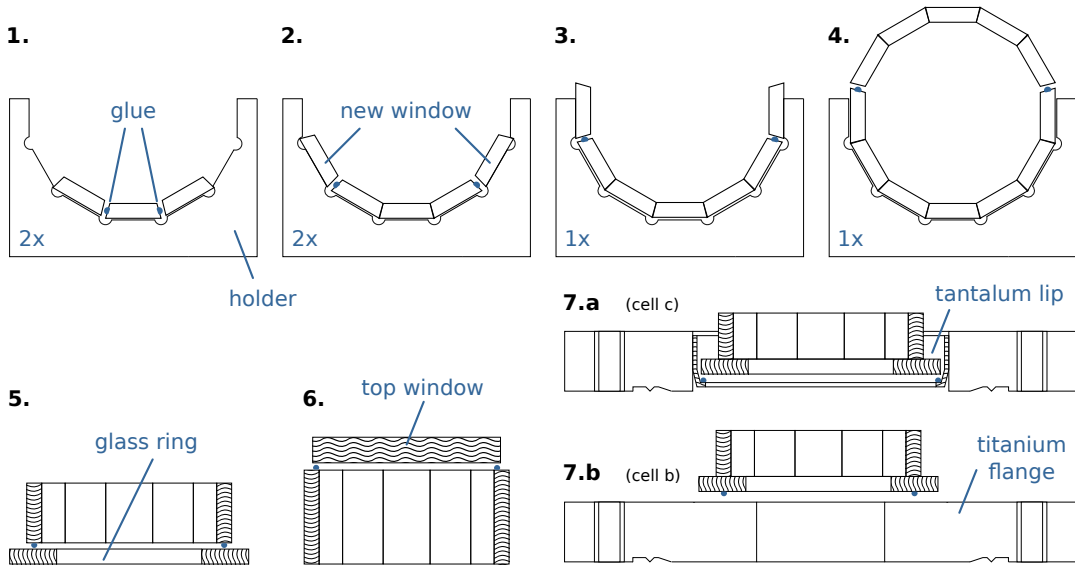


Figure 2.5.: Stages of assembly: All side windows are cured in six steps to form a cylindrical structure (1.-4.) that is closed on one side by a glass ring (5) and a top window (6). The resulting glass structure can then be glued into a titanium flange (7.b, cell b) or stainless steel flange with a tantalum weld ring (7.a, cell c).

to another indicating that the adhesive is indeed establishing a rigid bond.

2.3.2. Characterizing the Vacuum Properties

Achieving the lowest vacuum pressure requires maintaining of the cleanness of the coated surfaces of each cell window and flange components. Additionally, plasma cleaning has been used to reduce the coverage of adsorbed molecules on the wall surface of a test setup [68], which is shown in figure 2.6(a). The cell is attached to a cross hosting further detection equipment such as an residual gas analyzer (Vacscan Plus⁸) and a Bayard-Alpert ion gauge (UHV-24⁹) which can be read out by a gauge controller (sennTorr¹⁰). The pumping speed of a turbo pump can be controlled by means of a valve that separates the measurement chamber from a turbo pump (PM073073-T) and the pumping stand (TSU 071 E¹¹).

The cold plasma is generated by a self-resonant circuit, see section B.6, which uses the chamber as one electrode and aluminum foil wrapped around the top part of the glass cell as the second electrode. The plasma cleaning lasts up to 20 min for varying pressures (mostly argon) in the range from 1 mbar – 10 mbar to scan different glow discharges of purple (lowest pressure), white (intermediate pressure), and pink color (highest pressure). In principle, an oxygen plasma allows for an effective removal of thin films of hydrocarbon-

⁸Spectra Incorporated

⁹Agilent Technologies, Inc.

¹⁰Varian Vacuum Technologies

¹¹Pfeiffer Vacuum GmbH

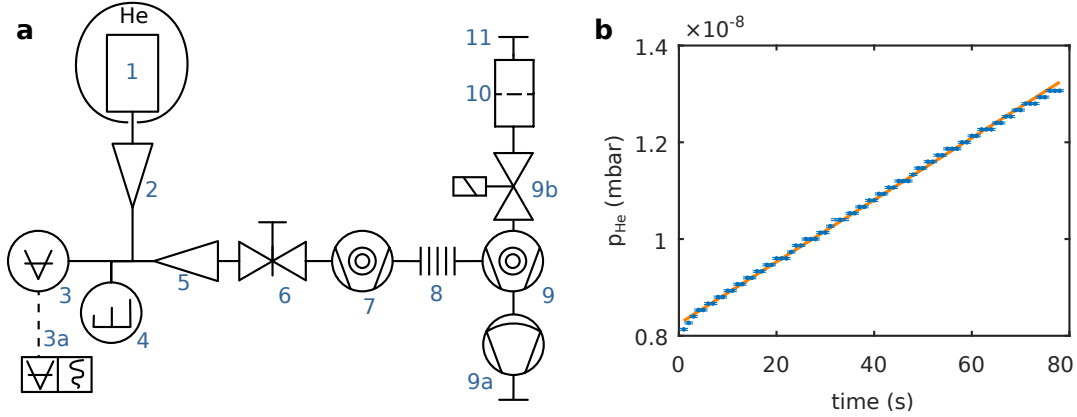


Figure 2.6.: Helium leak test: (a) The setup consists of a glass cell (1), reducer flanges (2,5), an ion gauge (ion) plus integrated logging device (3a), a residual gas analyzer (4), a valve (6) that is connected to a turbo molecular pump (7). A bellow (8) combines the system to a pumping stand with a turbo molecular pump (9) and membrane pump as a pre-pump (9a). The combined system can be vented via a valve (9b) nitrogen (11) which is dried beforehand (10). (b) The time evolution of partial helium pressure after closing the valve.

ates from aluminium and stainless steel chamber surfaces due to oxidization. In contrast, an argon plasma cleans surfaces similar to sand-blasting and is thus less selective towards the type of contamination [69]. Subsequent to the plasma cleaning, a bake-out procedure up to $150\text{ }^{\circ}\text{C}$ yields a final pressure of 2×10^{-10} mbar in this test system as well as in the main chamber. However, the fragility of the presented UHV cell towards temperature differences due to thermal expansion requires to limit the maximum baking temperature and to change the temperature during heating or cooling operations as much as possible. This is even more important when further components are bonded to the cell, for instance an objective which is made of different materials, see chapter 4).

We measured the integral leak rate of helium for cell b – the cell which is connected to the titanium flange – by covering the complete cell in a balloon filled with helium and observing the rise of the partial pressure of helium using the residual gas analyzer. As shown in figure 2.6(b), the partial pressure of helium is linearly increasing when the valve (6) is closed. The resulting slope of the partial pressure translates into a helium leak rate of $6(2) \times 10^{-11}$ mbar l/s where the confidence interval is dominated by the systematic error of estimating the volume $V = 0.95(2)$ l of the chamber.

2.3.3. Determining the Optical Properties

We determine the birefringence of the evacuated cell by measuring the polarization distortion of a linearly polarized probe laser beam crossing a single cell window as indicated in section 2.1. The laser beam probes a circular region of 2 mm diameter situated about 20 mm above the flange in cell b, shown in figure 2.3(b). The measurement procedure is illustrated in figure 2.7(b): For each choice of the polarization angle θ inside the cell,

we record the maximum $I_+(\theta)$ and minimum $I_-(\theta)$ laser intensity after a rotating polarization analyzer positioned behind the cell. The measured extinction ratio, which we define as $\eta(\theta) \equiv I_-(\theta)/I_+(\theta)$, exhibits a sinusoidal variation as a function of θ , as shown in figure 2.7(a). The amplitude of the recorded signal allows us to determine the amount of birefringence.

As reported in [46], we use Jones' calculus to model the transformation of polarization by the vacuum cell. We assume a transformation matrix M of the most general form [70]

$$M = R(\beta) \cdot R(\theta_0) \cdot \begin{pmatrix} e^{i\phi/2} & 0 \\ 0 & e^{-i\phi/2} \end{pmatrix} \cdot R(-\theta_0),$$

where ϕ is the phase retardation, θ_0 is the angle denoting the orientation of the optical axes parallel to the window's surface, and β is the angle characterizing the optical activity. $R(\gamma)$ is a 2×2 rotation matrix by an angle γ . We obtain for the intensities $I_+(\theta)$ and $I_-(\theta)$ of the setup in figure 2.7(b):

$$I_{\pm} = \frac{1}{2} \pm \frac{1}{2} \sqrt{1 - \sin^2(\phi) \sin^2(2(\theta - \theta_0))} \quad (2.8)$$

which are independent of β . The ratio of the two intensities yields $\eta(\theta)$, which is fitted to the experimental data shown in figure. 2.7 taking into account a possibly non-vanishing offset. The fitting procedure allows us to determine θ_0 and ϕ , where $\phi = kL\Delta n$ (L is the thickness of each glass window, $k = 2\pi/\lambda$ is the wave vector of the probe laser beam, and Δn is the amount of birefringence). The peak-to-peak amplitude A of the signal $\eta(\theta)$ is directly related to Δn according to the formula

$$A = \frac{1 - |\cos(kL\Delta n)|}{1 + |\cos(kL\Delta n)|}. \quad (2.9)$$

Note that in the case of small birefringence, there is a quadratic dependence of the amplitude of the extinction ratio A on the amount of birefringence Δn .

The offset is an indication for either residual stray light or an inhomogeneous birefringence since we effectively average the extinction ratio over the entire beam size. Careful blocking of the stray light is absolutely mandatory for this measurement since the transmitted power in the extinction configuration only yields a few nanowatts compared to the initially 70 mW of laser beam power after the first polarizer.

We further conclude from figure 2.7 that the additional stress caused by the differential pressure after evacuation of the cell lead to larger birefringences and a tilt of the polarization axis. However, for some windows we observed that the birefringence value at a wavelength of 866 nm is even reduced after evacuating the cell. Thus, we conclude that the residual stress in the cell is of a similar magnitude than the stress created by external forces. We further infer from repeated measurements that the birefringence does not change significantly within a few degrees deviation from normal incidence or within ± 2 mm offset from the center of the window.

All obtained values for Δn and θ_0 of each window of the glass cell b under vacuum conditions are listed in table 2.1. The birefringences are on the level of 10^{-8} while the two significantly larger birefringences are observed for two opposing windows (no. 5 and

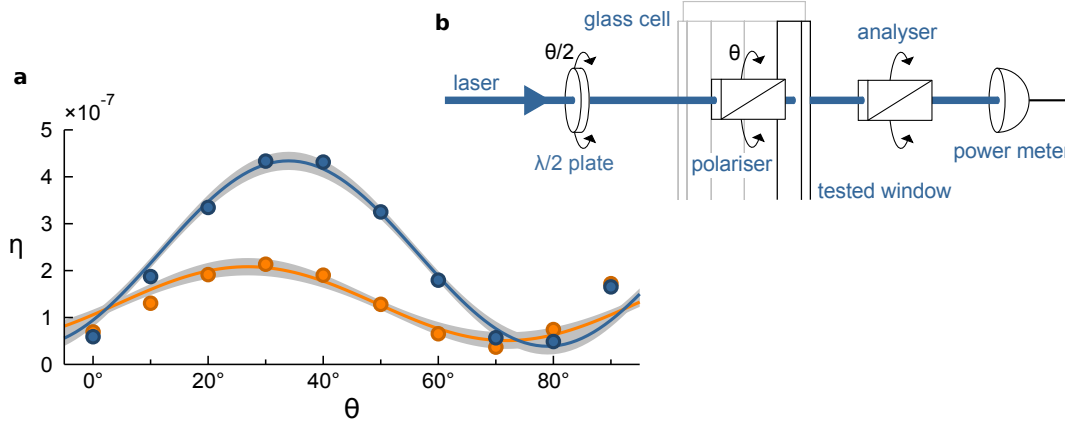


Figure 2.7.: Determination of the birefringence as presented in [46]: (a) Typical window birefringence under vacuum conditions (blue) and atmospheric pressure (orange) recorded for cell b. Instrumental uncertainties are below the size of the markers. The shaded area indicates the 0.68 confidence region. (b) Optical setup using two polarizers and a power meter.

no. 11). The higher birefringence for these two windows might arise from step 4 of the bonding procedure (Fig. 2.5) in which two larger cell parts are bonded to form the cylindrical glass structure. The discrepancies in the alignment of all windows accumulate up to this step such that the new adhesive layers need to eventually compensate larger distance variations along the contact surfaces – dominantly shearing effects. The measurement results shown in table 2.1 indicate that there is no obvious systematic behavior in the orientation of the polarization axis of the birefringences. Initially, we would guess that all axes were aligned with the symmetry axis of the cell if the adhesive contact layer were of similar shape for all windows and no droplets were formed.

The measured birefringence values are well below the typical values recorded with optical glass cells (10^{-7}) and viewports (10^{-6}) under vacuum conditions [49, 51]. Note that, the reported values were determined with a probe beam of smaller size which might result in a smaller measured birefringence if a small inhomogeneity is present. The amount of birefringence recorded in our vacuum cell translates into tiny retardances on the level of $\lambda/5000$. A compensation of small homogeneous birefringences could, in principle, be done by means of a Babinet–Soleil compensator, which consists of two retarder wedges translatable and an additional fixed plate of fixed retardance. However, an Ehringhaus compensator [71] might be better suited to compensate the birefringence of the glass cell due to its smaller dependence of the retardance on the tilt angle. Such a compensator consists of two identical quartz windows of identical retardance mounted in a way that their retardance vanishes when a beam is perpendicular to the window surface. A small tilt causes a different thickness along one direction leading to a small amount of birefringence.

In contrast, an in-situ measurement of the birefringence of the relevant glass cell c – the one mounted to the main vacuum chamber – is not feasible due to the absence of

Table 2.1.: Birefringence Δn and angle θ_0 of cell b are extracted from the measured extinction ratios for individual cell windows under vacuum conditions (< 10 mbar). The angle θ_0 is given with respect to the symmetry axis of the cell. The data is published in [46].

No.	1	2	3	4	5	6
Δn (10^{-8})	3.0(4)	1.6(4)	2.4(2)	1.8(4)	4.0(6)	0.8(4)
θ_0 ($^\circ$)	-2(1)	22(1)	-41(1)	22(1)	26(1)	45(1)
No.	7	8	9	10	11	12
Δn (10^{-8})	1.2(2)	3.4(4)	2.8(4)	1.6(2)	7.8(2)	1.0(4)
θ_0 ($^\circ$)	-18(1)	5(1)	-7(1)	43(1)	33(1)	1(1)

Table 2.2.: Birefringence Δn and angle α of cell c obtained from the measured extinction ratios of each pair of windows facing each other. The angle α is given with respect to the symmetry axis of the cell.

No.	1	2	3	4	5	6
Δn (10^{-8})	2.1(1)	4.5(1)	2.9(1)	3.1(1)	2.2(1)	8.2(2)
α ($^\circ$)	5(1)	5(1)	11(1)	8(1)	-5(1)	1(1)

a rotatable polarizer inside the cell. In the future, the birefringence can be obtained by spectroscopy methods where the atoms itself act as the probes [49]. So far, we were only able to determine the combined birefringence for each pair of opposing windows, see table 2.2. The listed values cannot be directly translated into the birefringence of a single window since the birefringence of opposite windows can, in principle, take any value between a full cancellation and an addition of the birefringences. Yet, we assume that the direction of the mechanical stress tensor in each window is oriented arbitrarily with respect to the symmetry axis of the cell, and thus, a full cancellation of the combined birefringence for a pair of opposing windows is unlikely to occur. Hence, we can infer that the birefringence of a single window is on the same order of magnitude.

2.4. Vacuum Window

Originally, we bought the glass cell flange for cell c and an additional viewport made of SF57 glass in a combined order from Torr Scientific Limited. Unfortunately, the bad quality (detached coating, schlieren at the glass surface, leak) of the delivered viewport did not fulfill our requirements even after having received a replacement part by the company. Thus, we separately ordered a stainless steel flange with a tantalum lip from Hositrad Holland B.V. and bonded it to a SF57 window (diameter 68 mm) using the same technique as for the flange of the cell. The requirements for the window are a thickness of 5 mm, surface quality of 40/20 (scratch/dig), surface flatness of $\lambda/8$, and a broadband anti-reflection coating ($R < 0.5\%$) for all wavelengths λ in the range between 850 nm and

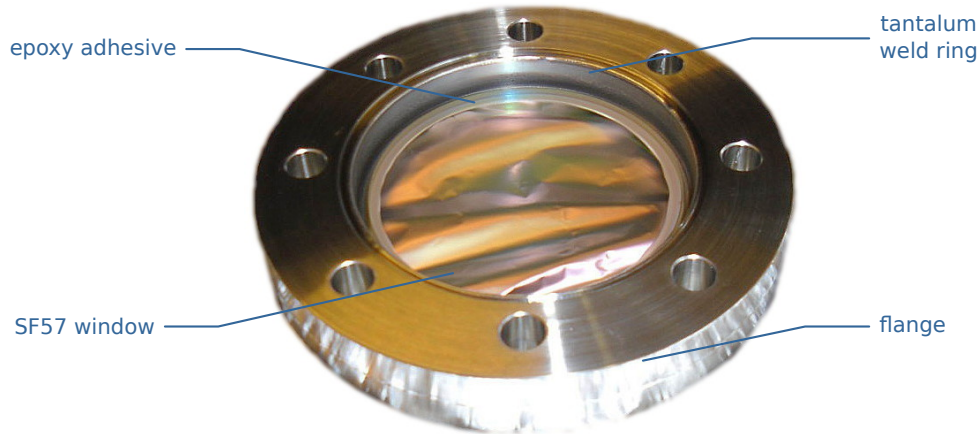


Figure 2.8.: Assembled vacuum window wrapped by aluminum foil for cleanliness

1064 nm.

2.5. Long-Term Vacuum Pressure

Up to now, the vacuum system has been operating for about two years in the ultra-high vacuum regime (3×10^{-10} mbar) similar to [63] but in stark contrast to an experimental apparatus at the University of Birmingham [62]. There, single windows glued to a metal chamber structure using EpoTek 353ND adhesive lead to a pressure increase from an ultra-high vacuum to high vacuum conditions over a time period of a few weeks due to permeation of water.

In our case, we observe a small increase in the total pressure (about 0.5×10^{-10} mbar) to a slightly higher equilibrium pressure when the glass cell is placed in a humid environment created by open water in a plastic bag. Furthermore, we measure a slightly lower vacuum pressure during the time period of about 40 days when the vacuum cell and the window are purged by a dry nitrogen flow (50l/min). Thus, we constantly employ a nitrogen purge into the magnetic shielding that is placed around the glass cell as shown in chapter 3. In addition, we observe that the loading of the magneto optical trap is becoming less efficient after a few weeks and that the vacuum pressure is increasing by 2×10^{-10} mbar if we stop the heating of the cesium reservoir. We attribute the continuous decay in the partial pressure of cesium to the permeation of water vapor into our vacuum chamber in combination with the strong chemical reaction of the two components. An equilibrium pressure of 2(1) mbar is found to allow for reasonable loading time of the magneto optical trap corresponding to a heating temperature of around 38 °C for the reservoir.

A reason for the relatively small effect of humidity onto the vacuum pressure might be given by the utilized filled adhesive as well as the plasma cleaning procedure which is reported to create diffusion barriers [72]. Exchanging the epoxy adhesive by the adhesive EpoTek 377 might further reduce the water permeation since it exhibits a water absorption which is about two times smaller than 353ND and better than H77 [73]. In

2. Ultra-High Vacuum Chamber With Ultra-Low Birefringence Glass Cell

general, adding protective layers or barriers on top of the epoxy adhesive can help to further suppress water permeation, for instance by vapor deposition of Al_2O_3 and SiN plasma-enhanced chemical vapor deposition [74].

Lower pressure could also be achieved by exchanging the bonding method to less permeable materials like indium for the price of a lower bake-out temperature which is limited by the melting temperature of 156° .

3. Control of Magnetic Fields and Magneto-Optical Trapping

In quantum optics, magnetic fields are widely used to define a quantization axis required for state-preparation and manipulation [17, 29, 36], to address single atoms in an optical lattice [75, 76], to select a two-dimensional lattice plane [31, 76–78], to employ Feshbach resonances [79] for controlling interactions in quantum gases, to trap [80–82] and to transport atoms [83, 84]. All of these techniques enforce a precise control of magnetic fields.

However, the coupling of quantum states to external fields is not always desirable. Examples are in optical clocks [85], where magnetic fields cause undesired frequency shifts, and optical lattices experiments on quantum simulation and computation, where a fluctuating field causes dephasing and decoherence of the quantum states [38]. Solutions to achieve negligible energy shifts and long coherence times consist of using magnetically-insensitive Zeeman substates [85] and a precise mitigation and stabilization of magnetic fields by passive [86, 87] and active [87–89] means. In our case, for implementing a state-dependent transport experiment, we are restricted to the outermost Zeeman sublevels of the cesium hyperfine ground states, and are thus very sensitive to static magnetic fields as well as field fluctuations [37].

In this chapter, I present the design and construction of a two-layer magnetic shielding made of a high permeability metal to suppress the effect of external magnetic fields by two orders of magnitude. To avoid saturation of the main shielding, an additional magnetic shielding is established around the ion pump. Inside the main shielding, three pairs of Helmholtz coils pointing along orthogonal directions (called “compensation coils”) enable the preparation of an arbitrarily directed homogeneous magnetic bias field to compensate or define a field direction. In addition, the compensation coils are encompassed by two larger aluminum coils, which generate a quadrupole magnetic field for use in magneto-optical trapping, transport, and selection of a plane in a three-dimensional lattice.

A rendered cutaway drawing of the complete setup including the main magnetic shielding and all coils, as well as the vacuum chamber from the previous chapter is shown in figure 3.1. The setup is built on top of a stable non-magnetic breadboard¹ (thickness 100 mm, size 1500 mm × 1500 mm) featuring a rectangular feedthrough in its center (size 150 mm × 150 mm). The breadboard is located 35 cm above a non-magnetic optical table (M-RS2000 with damping system S-2000A-423.5)². The vacuum chamber is mounted below the breadboard such that the high numerical aperture objective inside the vacuum glass cell is positioned at a height of 89 mm above the breadboard surface, which corresponds to the position of the optical lattice.

¹Opta GmbH

²Newport Corporation

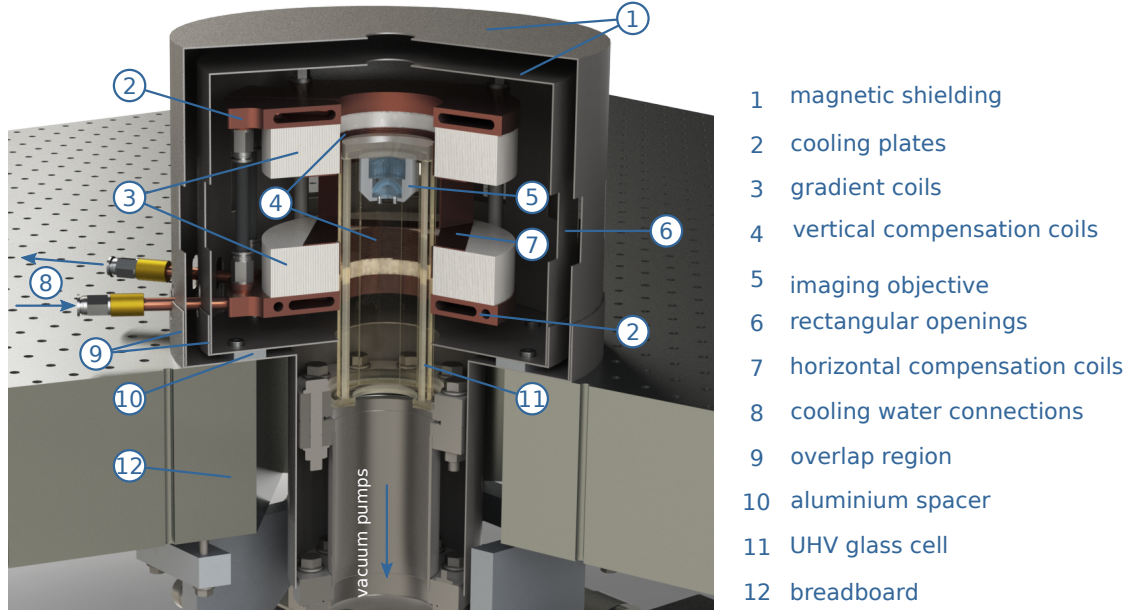


Figure 3.1.: Cutaway drawing of the mechanical setup of the experiment.

The magnetic quadrupole coils are made of aluminum and are in direct contact with copper plates for water cooling. The distance between the plates is enforced by stainless steel pillars to form a rigid structure that is mounted to the breadboard and can withstand the force caused by the magnetic fields. In the vertical direction, the compensation coils fit in between the gradient coils and the glass cell with direct contact to the gradient coils. The horizontal compensation coils are mounted in between the gradient coils in close proximity to the glass cell. This compact geometry of the coils allows for a fast switching of the magnetic fields and large optical access to the inner side of the chamber. All connections – electrical as well as water cooling – in between the gradient coils are aligned to the window edges of the dodecagonal glass cell to gain full optical access.

The two-layer magnetic shielding ($\varnothing_{\text{inner}} = 235 \text{ mm}$, $h_{\text{inner}} = 170 \text{ mm}$, $\varnothing_{\text{outer}} = 267 \text{ mm}$, $h_{\text{outer}} = 190 \text{ mm}$) encompasses the structure of the coils and the glass cell. While the inner layer possesses a large bore ($\varnothing = 65 \text{ mm}$) in its center, the outer layer is extended ($\varnothing = 120 \text{ mm}$, $h = 150 \text{ mm}$) further to the main vacuum cube to achieve a high attenuation of static, as well as low-frequency, magnetic fields. Both shielding layers (thickness 1 mm) feature twelve horizontal rectangular openings ($40 \text{ mm} \times 20 \text{ mm}$), as well as a circular opening ($\varnothing = 30 \text{ mm}$) on the top, that are aligned to the radial windows of the glass cell and the optical axis of the objective, respectively. Furthermore, two holes in the shielding layers on the left side of the drawing (see figure 3.1) act as feedthroughs for the pipes of the water cooling and for the electrical connections of the magnetic coils. To allow for positioning of the coil structure, both shielding layers comprise of two parts that are stacked close to the top surface of the breadboard. All inner surfaces of the shielding that might get in contact with stray light are coated with a matt dark paint to avoid reflection into the direction of atoms.

3.1. Magnetic Shielding

The shielding factor of a magnetic shielding is defined as

$$S = \frac{H_{\text{with}}}{H_{\text{without}}}, \quad (3.1)$$

where H_i denotes the magnitude of the magnetic field in the absence (H_{without}) and in the presence (H_{with}) of a magnetic shielding. In our system we aim for a shielding factor of at least 100 in the transverse and longitudinal direction to eliminate magnetic fields as a dominant source for decoherence [37]. In case of a closed cylinder made of single layer of a high permeability material, an approximation for the transverse field S_t and for the longitudinal field S_l yields [90]

$$S_t = \mu_r \frac{d}{D} + 1 \quad \text{and} \quad S_l = \frac{4N(S_q - 1)}{1 + \frac{D}{2L}}. \quad (3.2)$$

Here, d denotes the thickness of the shielding layer, D the diameter of the cylindrical shielding, L the length of the cylinder, μ_r the relative permeability of the shielding material, and N a demagnetization factor, which can be approximated by $N \approx 0.38(L/D)^{-1.3}$ if $1 < L/D < 10$. Note that in the following the term ‘‘magnetic field’’ refers solely to the quantity $B = \mu_r \mu_0 H$, where $\mu_0 = 4\pi \times 10^{-7} \text{N/A}^2$ is the vacuum permeability and μ_r is the relative permeability of the material.

We use a nickel–iron soft magnetic alloy called ‘‘Mu-metal’’, which possess a high relative permeability of typically $\mu_r = 30,000$. Hence, a shielding with the dimensions of the inner cylinder barely provides a transverse $S_t \approx 130$ and longitudinal $S_l \approx 100$ shielding factor according to the approximation of N especially since the condition $L/D = 0.8 < 1$ is not fully met. Note that the shielding factor of this material increases linearly with the thickness of the layer, at least for the case where openings are neglected. For a multi-layer shielding, the individual shielding factors of each layer multiply if the layer distance is large enough. Thus, two layers should provide the requested shielding factor of 100.

To study the influence of the openings, I performed a three-dimensional finite element simulation of static magnetic fields for the presented magnetic shielding using the software EMS³. The EMS add-on fully integrates into the CAD⁴ software Solidworks⁵, enabling a fast improvement of the design based on simulation results.

3.1.1. Design and Simulation

In the simulation, the shielding is placed between two large parallel blocks of permanent magnets to define a homogeneous background field in a direction orthogonal to the block surfaces if the shielding is not present. The magnetic field strength is calculated on an automatically generated mesh of a spatially dependent mesh size. However, the user is responsible for choosing the correct parameters for mesh generation, for instance, by

³ElectroMagneticWorks, Inc.

⁴Computer Aided Design

⁵Dassault Systemes Deutschland GmbH

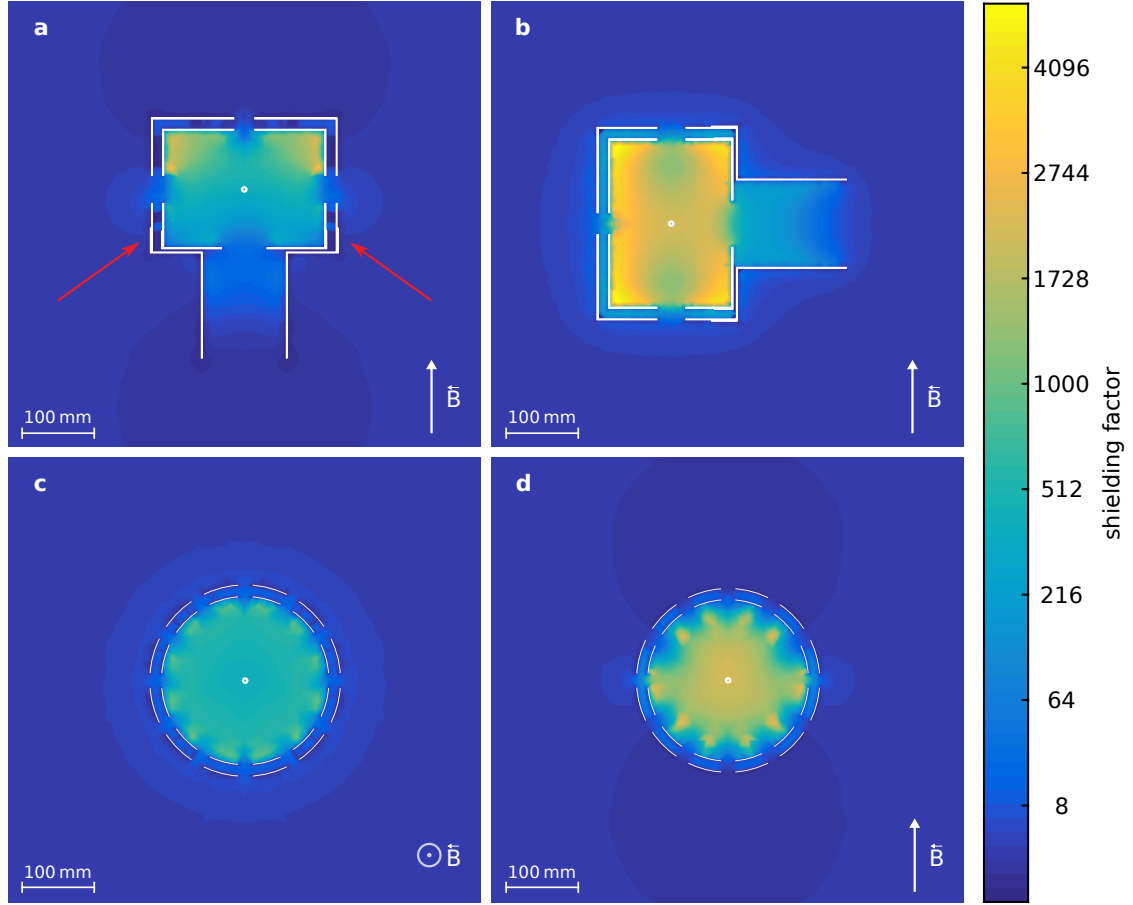


Figure 3.2.: Cuts of the three-dimensional attenuation of the magnetic shielding for vertical (=longitudinal) magnetic fields (a,c) and horizontal (=transverse) magnetic fields (b,d). The white circles indicate the later position of the atoms. Numerical artifacts close to the magnetic shielding (white lines) arise from linear interpolation of mesh nodes due to the cut drawing. The red arrows in in (a) indicate the overlap region of shielding parts.

adapting the mesh size for certain regions. Candidates for these regions are the shielding layers, due to their relatively small thickness, and the overlap region between two parts of the shielding, see figure 3.1. According to the production company (Sekels GmbH), the spacing between the upper and the lower part of each layer at the position of the overlap typically amounts to 0.5 mm. This spacing tolerance is of importance since a larger spacing reduces the maximum magnetic flux and, consequently, the shielding factor.

The simulation results in a transverse $S_t^s = 2000$ and longitudinal $S_l^s = 300$ shielding factor in the center of the shielding, shown as white circles in figure 3.2. Several conclusions emerge from this figure. First, the shielding factor depends on the direction of the magnetic field and is limited by the openings in the shielding. Second, adding pipes to an opening results in an improved shielding factor, as visible by the guiding of magnetic fields due to the extend of the outer shielding layer. Likewise, a larger distance between

the layers leads to an increased shielding factor up to the limiting case of the product of individual factors. Third, a double layer shielding is absolutely necessary to achieve a shielding factor of at least 100 for all directions of the magnetic field.

However, the dimensions of the shielding and the distance between layers is subjected to the mechanical constraint set by the inner coils and the position of focusing optics for the laser beams. Note that, a minimal overlap of 20 mm – we choose 25 mm (inner layer) and 35 mm (outer layer)– for two shielding parts is required for the given spacing between the bottom and the top parts at the overlap region to prevent a degradation of the shielding factor. The magnetic shielding factor for higher frequencies (50 Hz power grid, 16.6 Hz power grid for trains) is typically larger due to induced eddy currents in the shielding compared to the fully simulated static fields [90].

Physical Realization

It is known that simulation results may differ significantly from experimentally determined shielding factors [90]. Differences can arise from mechanical tolerances at the overlap region, magnetization of the shielding during transport, saturation of the high permeability material, and from residual inhomogeneities in the Mu-metal material.

I determined the shielding factor experimentally by measuring the three orthogonal field components using a three-axis fluxgate magnetometer Mag-03⁶ (full-scale range $\pm 70 \mu\text{T}$) outside of the shielding and in its center. For this measurement, the presence of the Earth's magnet field is compensated by determining the magnetic fields components for opposite directions of the dipole moment of a permanent magnet. The magnet is placed at a distance of about one meter in order to reduce the field strength and, thus, to utilize the full dynamic range of the sensor. The difference of each magnetic field component for different orientations of the permanent magnet yields the two shielding factors $S_t^e = 1530_{-100}^{+1620}$ and $S_l^e = 251_{-18}^{+234}$. The experimentally determined values coincide with the corresponding values resulting from the simulation. The errorbars correspond to a confidence interval of 0.68 and are calculated according to section A in the appendix. The large asymmetry results from the limited dynamic range of the detector since the residual field inside the shielding is only slightly larger than the resolution of the digital magnetic sensor. Yet, a more precise measurement could be performed using microwave spectra of single atoms, which determine the frequency shift of atom resonances (see chapter 6).

Regular Demagnetization

Optimal shielding performance is achieved when external fields or field fluctuations do not cause saturation inside the shielding material and when the permeability is at its maximum value, i.e. for low fields and no remanent magnetization. We follow the approach presented in reference [91] to reduce the remanence: The cross section of each shielding part is encompassed by a single loop of a wire ($\varnothing = 0.8 \text{ mm}$) such that the Mu-metal material forms the core of the loop. As a result, the magnetic field created by a current through the single loop is mainly guided by the shielding part. Starting from a

⁶Bartington Instruments Ltd.

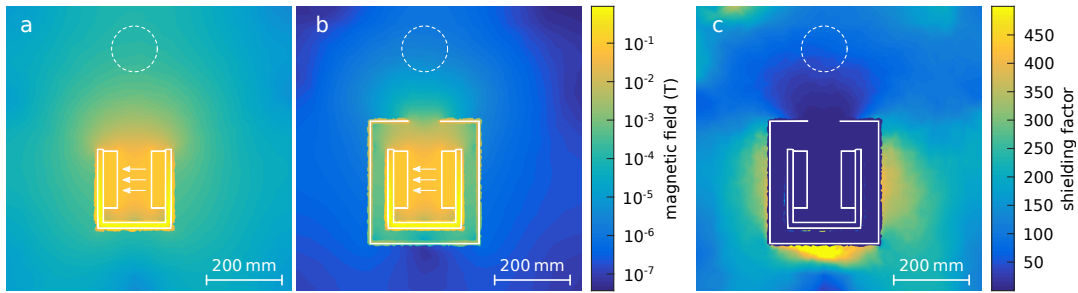


Figure 3.3.: (a) Magnitude of the assumed magnetic field distribution generated by the permanent magnets inside the ion pump. White lines indicate the relevant structure of the ion pump and the shielding white arrows mark the direction of the field and the dashed circles denote the projected position of the main shielding, which is located at a distance of about 50 mm to the visible plane. (b) Magnitude of the magnetic field for the same permanent magnet but with magnetic shielding. (c) Corresponding spatially varying shielding factor yielding a reduction of 50 of the stray magnetic field at the position of the main shielding.

high amplitude alternating current at 50 Hz that drives the material into saturation, we adiabatically lower the amplitude below the level of the ambient field.

The entire demagnetization process is controlled via our lab computer (see section B.1). Its signal is subsequently amplified by a TA FE530R⁷ stereo amplifier up to a maximum current of $I = 4$ A and impedance matched to the four demagnetization loops. The magnetic field B inside the shielding can be estimated using the approximation $B = \mu_r \mu_0 I / (\pi d)$, where the relative permeability of the material μ_r is, in general, a function of the external magnetic field B due to hysteresis. To overcome the Earth's magnetic field and to drive the system into saturation a minimum current of $I = 100$ mA is required for the demagnetization process.

3.1.2. Ion Pump Shielding

According to the manual of the pump, the permanent magnets mounted in the ion pump cause a magnetic field of about 10×10^{-4} T at the inlet of its main flange. To avoid saturation of the main shielding, an additional shielding is required. The magnetic field distribution in the absence and the presence of the shielding as well as the corresponding shielding factor is shown in figure 3.3. The extension of the main shielding is closest to the ion pump and its projection onto the plotted cut of the magnetic field is indicated by a white circle. The distance between this extension and the cut amounts to 50 mm. The attenuation amounts to circa 50 at this position, which yields a magnetic field less than the Earth's magnetic field, and to even about two orders of magnitude in the far distance.

⁷Sony Corporation

Table 3.1.: Generated magnetic fields for different coil pairs assembled in a Helmholtz-like configuration.

coil pair	field along axis (T/A)	field off axis (T/A)	variation (10^{-3})
horizontal	1.63×10^{-4}	$< 9 \times 10^{-7}$	< 5
vertical	2.90×10^{-4}	$< 1 \times 10^{-7}$	< 1
gradient	1.03×10^{-1}	$< 5 \times 10^{-6}$	< 0.02

3.2. Magnetic Coils

3.2.1. Compensation Coils

Inside the magnetic shielding, three orthogonal pairs of compensation coils compensate residual stray field components and generate a weak guiding field to define the quantization axis for the atoms. These coils are self-supporting and integrated between the gradient coils to minimize their impact on the optical access to the vacuum system (see figure 3.1). The vertical compensation coil pair possess a hollow cylindrical shape ($\varnothing = 65$ mm) to conform to the first winding of the gradient coil. The two pairs of the horizontal coils exhibit a rectangular shape (smallest dimensions 65 mm \times 40 mm) to fit in between the gradient coil pair. A picture of the structure of all horizontal compensation coils is shown in figure 3.4(a) and the full assembled coil setups in figure 3.4(c). I manufactured the coils by winding an enamelled copper wire ($\varnothing = 0.8$ mm) around a block of polytetrafluoroethylene and fixing its position by a small layer of two-component epoxy adhesive. Curing the adhesive at around 80 °C results in a solid self-supporting structure that can easily be separated from the polytetrafluoroethylene block.

Each compensation coil consists of 20 windings for the horizontal coils, as well as 21 windings for the vertical coils. This geometry theoretically corresponds to a relatively low inductance $L_{\text{comp}} \approx 1 \mu\text{H}$ and tiny Ohmic resistance $R_{\text{comp}} \approx 60 \text{ m}\Omega$ to allow for a fast switching of the coil current. The generated strength of the magnetic fields parallel and perpendicular to their geometry axis, as well as their relative variation over a cube of width 1 mm, are calculated using the same EMS software and are given in table 3.1. The coils are driven by EA-PS 3016⁸ power supplies delivering a maximum current of 16 A, which translates into a maximum field strength of $B_{\text{max}}^{\text{H}} = 26 \times 10^{-4}$ T and $B_{\text{max}}^{\text{V}} = 26 \times 10^{-4}$ T along the geometry for the horizontal and the vertical compensation coils, respectively.

3.2.2. Gradient Coils

Typical approaches for magnetic coils in cold atoms physics to generate a strong field or field gradients are solenoids made of copper wire or refrigeration tubing [92]. While removing the dissipated heat from a solenoid requires additional housing or tubing, refrigeration tubing is limited by the viscous resistance towards the flow of the coolant [93]. In contrast, we employ gradient coils comprising of 260 turns of an eloxidized aluminum

⁸Elektro Automatik GmbH

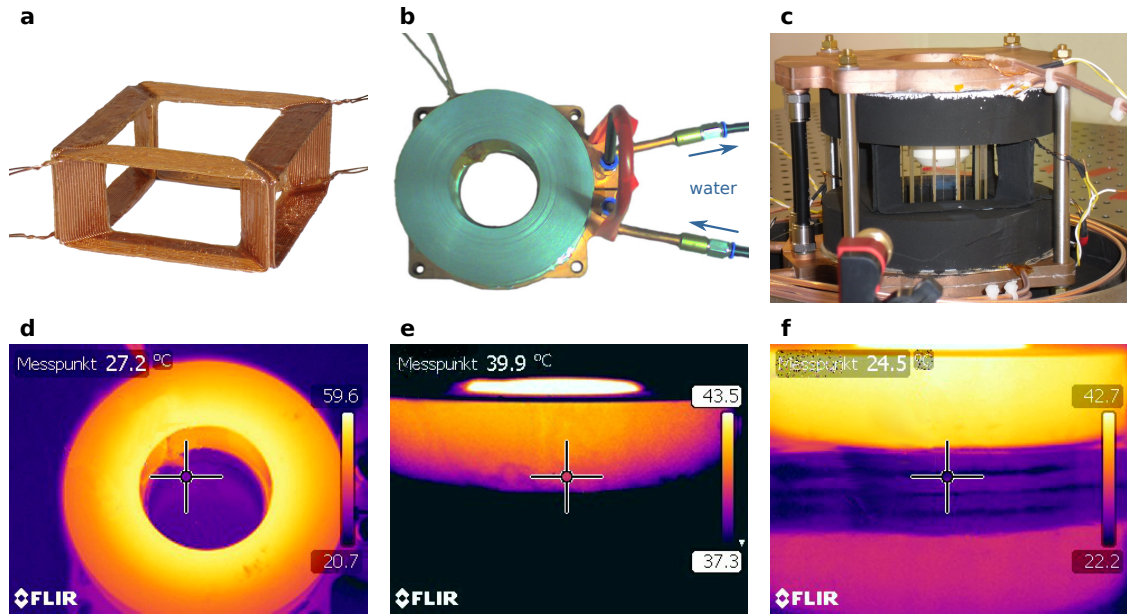


Figure 3.4.: (a) Horizontal compensation coils. (b) A gradient coil attached to a copper plate for water cooling. (c) Picture of complete assembly of all coils after they have been painted. (d-f) Thermographic pictures of a single gradient coil and cooling plate. The images have been corrected for about 5% of dead pixels on the camera chip.

strip in a single plane (height 30 mm, thickness 150 μm), which are manufactured by Steinert Elektromagnetbau GmbH and cooled by external cooling plates.

In general, the advantage of metal strips lies in their compact planar geometry that can easily be attached to cooling plate with fluid cooling. Neighboring turns are separated by insulating materials, for example, in standard copper stripes of polyimide or polytetrafluoroethylene, which increases the effective resistivity for the cross section of the coil. Even though copper exhibits a 54% larger electric conductivity than aluminum, the thin insulating layer created by anodization (thickness 6 μm for our coils) is about two orders of magnitude smaller than the insulation used for copper coils [62,94]. As a result, aluminum allows for a smaller effective resistivity for the total cross section of the coils leading to a more compact design. In addition, another advantage of the thin insulation is the improvement of the thermal contact to the cooling plates leading to a lower coil temperature or the possibility to increase the current.

We use a thin layer of thermally conductive epoxy adhesive (Arctic Silver Thermal Adhesive⁹) to bond the aluminum coils to the cooling plates made out of copper. In order to ensure a minimal distance between the two components we place 9 stripes of Kapton tape (width ~ 5 mm) on the cooling plate in a radial direction. The minimal distance guarantees protection of the oxidized insulation layer during the bonding process. A slit in each cooling plate prohibits large eddy current during fast switching of coil currents. The gradient coils are usually connected in series in an anti-Helmholtz configuration (see

⁹Arctic Silver, Inc.

figure 3.4(c)), but can, in principle, be swapped into a Helmholtz configuration to explore Feshbach resonances [54]. Both cooling plates are directly interconnected in series to reduce the number of water connections to the outside of the magnetic shielding. We use a linear power supply SM 70-90¹⁰ controlled by the lab computer to power the coils as well as a current diverting device [95] used to reduce the current in the lower coil for magneto optical trapping, see section 3.3. Driving the coils by a single power supply results in an improved current noise characteristic compared to the use of two independent power supplies, where current noise is differential instead of common mode. To protect the coils from overheating I developed an interlock circuit that continuously monitors the temperatures of the coils, as well as the cooling plates, and deactivates any electrical current in case of higher temperatures, see appendix B.3.

I calculated the magnetic field for our gradient coils numerically in Matlab¹¹ based on a simple loop calculator presented in [96]. The resulting field gradient along the vertical direction is 9.31 G/(cm A) with a variation smaller than 10^{-4} along a region of $\pm 50 \mu\text{m} \times 50 \mu\text{m}$ in the horizontal plane. Thus, a current of 32 A is necessary to create the desired magnetic field gradient of 300 G/cm. A small misalignment (1 mm) of the geometrical center of the gradient coils relative to the position of the atoms only results in a 0.5 % change in the magnitude of the field gradient and can, therefore, be neglected for all practical purposes. The experimentally determined inductance and resistance of each gradient coil amounts to $L_{\text{grad}} = 6.2(1) \text{ mH}$ and $R_{\text{grad}} = 0.62(1) \Omega$, respectively [95].

Power Considerations The equilibrium temperature distribution within a gradient coil and its corresponding cooling plate are shown in figure 3.4(e-f) for the maximum current of 32 A using the coil setup presented in figure 3.4(b). In total, 650 W of dissipated power lead to a maximum temperature of about 60 °C at the inner top side of the coil while the outer lower side is heated up to 40 °C. In contrast, the cooling plate temperature does not rise above 25 °C for an inlet water temperature of 17.9 °C, which leaves the cooling plate with a temperature of 20.1 °C at the water outlet.

In more realistic conditions, the coil temperature remains below 27 °C, for instance during continuous operation at 10 A for loading of the magneto optical trap or during pulsed driving mode for plane selection at 32 A with a duty cycle less than 10 %.

¹⁰Delta Electronica B.V.

¹¹Mathworks, Inc.

3.3. Magneto-Optical Trapping of Cesium Atoms

Since its invention in the 1980s, the magneto-optical trap (MOT) [80, 81, 97] has become the essential tool to provide cold atoms with an ensemble temperature in the microkelvin range. This source of cold atoms is of great importance for optical lattice experiments [18, 19, 29, 38] since the trap depth in such systems is limited to only a few millikelvins. Such a low trap depth prevents direct loading from a background gas due to the vanishing fraction of atoms in the low temperature tail of the Boltzmann distribution.

A MOT combines Doppler cooling and a restoring force to cool and trap atoms. In a simple picture, three-dimensional laser cooling, also called “optical molasses”, is based on three orthogonal pairs of two counter-propagating near resonant laser beams, which are red-detuned¹² from the atomic transition. Atoms moving along a laser beam direction preferably absorb photons from the counter-propagating laser beam due to the Doppler effect, while the spontaneous emission is isotropic. Thus, on average an atom is decelerated by the recoil caused by the momentum transfer during the absorption of a photon, which leads to cooling and to a viscous friction force in all directions. The continuous absorption and emission correspond to a random walk in momentum-space that limits the minimal achievable temperature to the Doppler temperature $T_D = \hbar \Gamma / k_B = 125 \mu\text{K}$ for near-resonant light at the D2-transition of cesium. Here, \hbar denotes Boltzmann’s constant and $\Gamma = 2\pi \times 5.2 \text{ MHz}$ constitutes the natural line width of the transition [98]. However, various sub-doppler cooling methods, e.g. Sisyphus (polarization gradient) cooling [80, 81], can yield even lower temperatures [27, 38, 99], typically a few tens of microkelvins.

A position dependent restoring force is realized by overlapping a magnetic quadrupole field to the optical molasses beams such that the degeneracy of the Zeeman states is lifted proportionally to the magnetic field. Following a $\sigma^+ \sigma^-$ -configuration, the polarizations of horizontal laser beams obey a right-handed helicity whereas vertical beams show a left-handed helicity, as shown in figure 3.5(a). Thus, the lower (higher) Zeeman substate is closer to resonance in regions of positive (negative) magnetic fields leading to a preferred absorption of σ^- (σ^+) photons and hence an effective recoil towards the center of the magnetic field.

3.3.1. Laser Sources

For cesium, the D2-line at a wavelength of $\lambda_{D_2} = 852 \text{ nm}$ is used as the near-resonant cooling light as shown in figure 3.5(b). We employ laser beams with a frequency that is red-detuned by $2\pi \times 10.2 \text{ MHz} \approx 2\Gamma$ from the $|F = 4\rangle \rightarrow |F'' = 5\rangle$ transition for cooling since this allows us to drive the population of atoms in a closed loop. Here, the double primed (non-primed) quantum numbers for the angular momentum F'' (F) refer to the $6^2P_{3/2}$ ($6^2S_{1/2}$) electronic state of cesium while primed number F' refer to the electronic states $6^2P_{1/2}$. Eventually, off-resonant scattering events of the type $|F = 4\rangle \rightarrow |F'' = 4\rangle$ lead to a population in the dark state $|F = 3\rangle$. Thus, an additional laser beam on the $|F = 3\rangle \rightarrow |F'' = 4\rangle$ transition acts as a repumper and transfers the population back into the cooling cycle.

¹²Red-detuned – as opposed to blue-detuned – refers to the case where the frequency of the laser beam is lower than the atomic transition frequency.

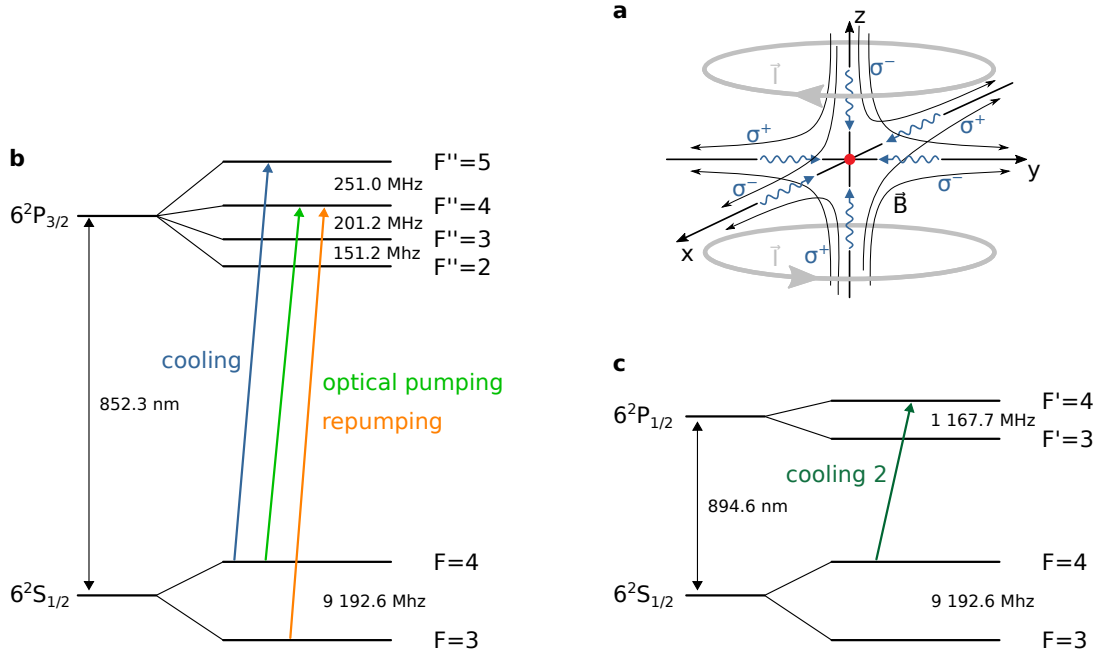


Figure 3.5.: Simplified schematic of the MOT adapted from [99] where a quadrupole magnetic field and six near-resonant circular polarized laser beams (blue) allow for cooling and trapping of atoms (red) in the geometric center. The simplified level scheme for the D2-line (b) and D1-line (c) of cesium shows relevant laser transitions for magneto-optical trapping and molasses cooling. Level separations are not drawn to scale. The level separations are taken from [98].

The power necessary for the repumper laser is typically lower than the one required for the cooling laser since only every thousandth scattered photon needs to be a repumper photon [94, 99]. However, the setup for fluorescence imaging (see chapter 4) prohibits the use of all MOT beams for molasses cooling since the vertical beams would shine into the sensitive camera. Therefore, we use the $|F = 4\rangle \rightarrow |F' = 4\rangle$ transition at the D1-line to cool the atoms in the vertical direction during fluorescence imaging in the optical lattice. As a result, all atoms are actively transferred to the former dark state $|F = 3\rangle$ demanding a relatively strong power of the repumper similar power than the cooling laser.

Optical pumping using the $|F = 4\rangle \rightarrow |F' = 4\rangle$ is eventually used to initialize all atoms in the Zeeman state $|F = 4, m_F = 4\rangle$, which is necessary for plane selection (section 4.3.3) and quantum walks (chapter 6).

External Cavity Diode Lasers Both – the cooling and repumping laser – are home-built interference filter lasers based on an original design by Peter Rosenbusch’s group [100]. Light emitted by a laser diode is collimated by a first lens, transmitted through a narrow-bandwidth interference filter ($\Delta\lambda < 1$ nm), and focused onto a partially reflective mirror. The position of the mirror – and thus the length of the cavity (~ 120 mm) – can be changed by a piezoelectric actuator for precise tuning of the wavelength. Due to the cat’s

eye configuration, interference filter lasers are less sensitive to tilts and vibrations [101] than lasers in a Littrow configuration [102], where a single grating is responsible for feedback and wavelength selection. We achieve a linewidth smaller than 10 kHz if we use an additional low-pass filter board (see section B.8) to reduce technical noise originating from our laser drivers ITC102¹³. A comprehensive characterization of this laser design can be found in René Reimann’s PhD thesis [103].

Both lasers are equipped with a 60 dB Faraday isolator I-80-U-4-852¹⁴ to prevent back reflected light from entering the laser cavity. Furthermore, the laser frequency is actively controlled using a polarization spectroscopy setup [104, 105] in a retro-reflected configuration [99]. The **cooling** laser is stabilized to the crossover signal in between the frequencies of the transitions $|F = 4\rangle \rightarrow |F'' = 3\rangle$ and $|F = 4\rangle \rightarrow |F'' = 5\rangle$, which is red-detuned by about 226 MHz from the desired cooling transition. The intensity and frequency of this beam are further controlled by an 110 MHz acousto-optic modulator (AOM) in a double-pass configuration that can shift the frequency into resonance. The non-shifted light is used for **optical pumping** since the frequency of this light is close to the $|F = 4\rangle \rightarrow |F'' = 4\rangle$ transition and the residual detuning is further compensated by light shifts of the optical lattice. The **repumper** laser is directly locked to the $|F = 3\rangle \rightarrow |F'' = 4\rangle$ transition and overlapped with the horizontal cooling beams.

In addition, we employ a distributed feedback (DFB) laser diode EYP-DFB-0894-00050-1500-TOC03-0005¹⁵ with an output power of 50 mW at the wavelength of $\lambda_{D_1} = 894.6$ nm for molasses cooling in the vertical direction during fluorescence imaging. The DFB laser light is split into two paths: one is shifted by 80 MHz via a AOM of the type 3080-122¹⁶ in order to lock the transmitted light to the $|F = 4\rangle \rightarrow |F'' = 4\rangle$ while the intensity and frequency of the other path are controlled by the experiment control using a separate AOM of the same type. The DFB laser diode is protected against back reflections by means of a Faraday rotator I-80-U-4-FR¹⁷ mounted in between two Glan-Laser polarizers¹⁸ yielding a suppression of 33(1) dB for our desired wavelength.

Furthermore, all laser beams can be blocked by optical shutters based on a design using bending piezos as reported in Arthur Widera’s group [106].

3.3.2. Beam Shaping

In our experiment, the magneto-optical trap is located about 1 mm in front of our high numerical aperture ($NA = 0.92$) objective that is oriented along the vertical direction. The full collecting angle of this objective amounts to 137° . As a consequence, laser beams for molasses cooling oriented under an angle to the horizontal plane cannot be used due to clipping at the objective lens. Thus, we need to specifically shape the beam profile of the four horizontal cooling beams and to compensate for the focusing effect of the objective for the vertical cooling beam.

¹³Thorlabs, Inc.

¹⁴Döhler Elektrooptik GmbH

¹⁵eagleyard Photonics GmbH

¹⁶Gooche & Housego PLC

¹⁷Döhler Elektrooptik GmbH

¹⁸Union Optics, Ltd.

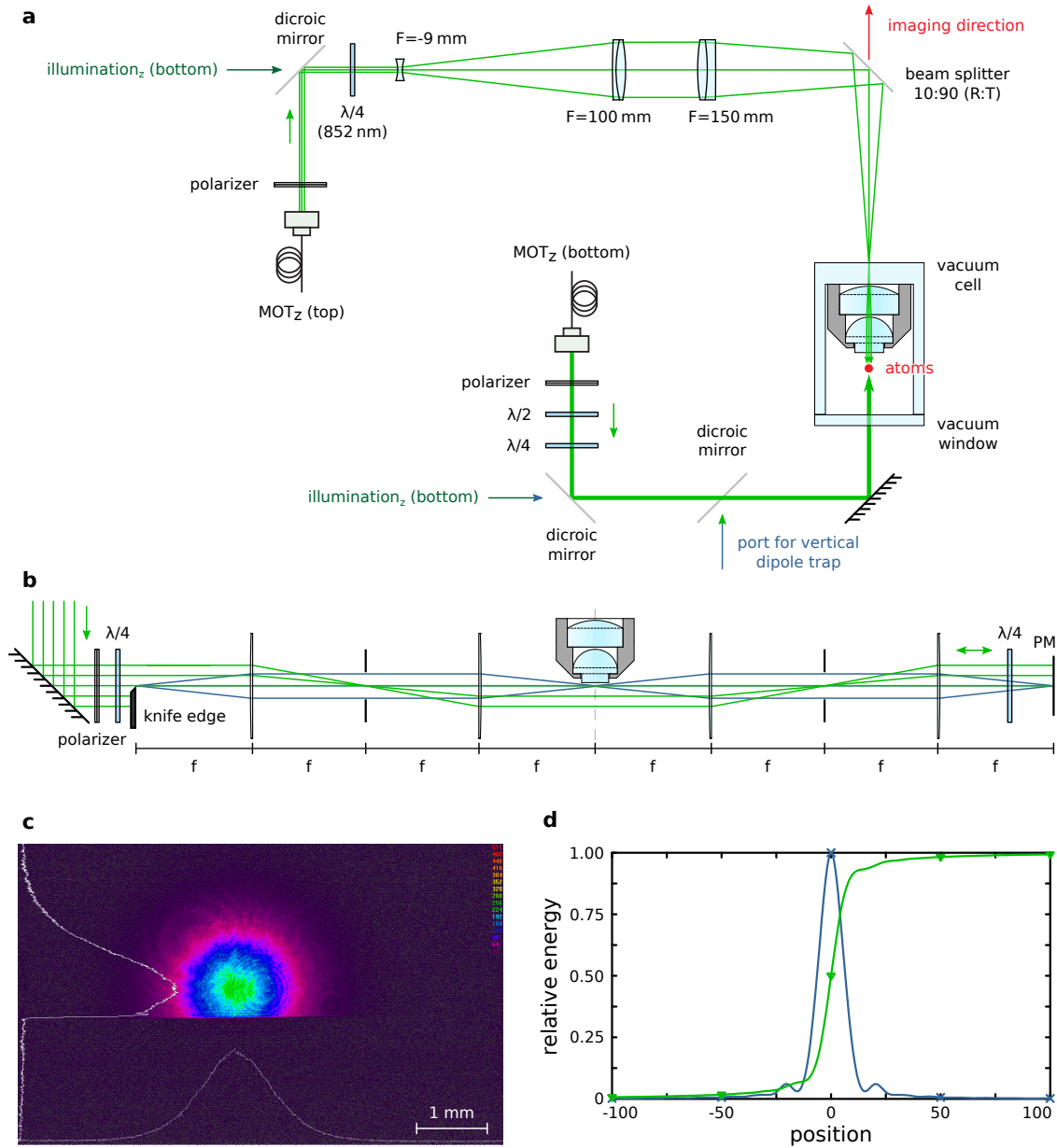


Figure 3.6.: (a) Setup for the vertical directions of the magneto-optical trap and illumination beams that are collimated in front of the high numerical aperture objective. (b) Horizontal setup to image a truncated Gaussian beam profile to the center of the objective. The beam setup is used for the two horizontal directions of whom the last mirror (PM) is mounted on a piezoelectric actuator. (c) Measured beam profile at the position of the objective, which is imaged on a beam profile camera at the position of the PM in (b). The integrated signals along the horizontal and vertical direction are shown as white lines. (d) Calculated line spread function (blue) and corresponding integrated knife-edge distribution (green).

To circumvent this issue, other groups magneto-optically cool and trap atoms at a farther distance and illuminate atoms in the optical lattice by total reflection at the objective [29], or by blocking the sixth beam that would otherwise shine directly into the objective during imaging [19]. The disadvantage of these approaches are residual reflections at optical elements, e.g. the objective or the glass cell, along the imaging direction that eventually reach the sensitive camera.

To compensate in the vertical direction, three 1" lenses are used to collimate the top MOT beam in front of the high numerical aperture objective lens. The first two form a telescope to increase the beam diameter to allow for a tight focus at the entrance of the objective using the third lens, see figure 3.6(a). The use of two achromatic doublets results in a diffraction limited performance of the optical system (Strehl ratio larger than 0.99) for the important wavelength range between 852 nm and 895 nm according to a simulation in the ray tracing software OSLO¹⁹. The resulting collimated beam diameter – defined as two times the Gaussian waist – amounts to 1.6 mm, and hence smaller than the beam diameter of the counter-propagating beam directed from the bottom (diameter 2.1 mm). A larger beam diameter would require larger optics, as well as a larger size of the telescope in order to minimize optical aberrations since mechanical constraints prohibit the use of a lens with a smaller focal length. We overlap the top vertical beam with the optical axis of the objective by means of a custom-made 2" beam splitter²⁰. The transmitted light is absorbed in a beam block LB1²¹ to avoid reflections in the direction of the optical axis of the objective, and hence in the imaging direction. The dichroic mirrors²² close to the fiber couplers combine the beams used for magneto-optical trapping with the beams used for molasses cooling during imaging in the optical lattice.

In the horizontal plane, we use four identical lenses with a focal length f in a $4f$ -configuration to image the beam profile clipped at a knife-edge onto the center of the objective, see figure 3.6(b). This setup is often employed in Fourier optics [107] and obeys the useful features that a Gaussian beam at the origin is exactly mapped to the identity at the output whereas a point source is imaged to the same point. As a result, we measure a beam profile, as shown in figure 3.6(c), which possess a steepness of the edge – defined as the distance between a 10 % and 90 % intensity of the beam – of approximately 18(4) μm for an aperture diameter of 3 mm. This is in good agreement with the ray tracing simulation yielding a point spread function and the point spread function also known as the knife-edge distribution, as shown in figure 3.6d. The knife-edge is positioned at a distance of 400(20) μm from the center of the Gaussian beam which itself is located about 500 μm away from the surface of the objective. The retro-reflecting mirrors are mounted onto electric actuators that are dithering at incommensurable frequencies of a few hundred hertz to avoid trap inhomogeneities due to standing wave patterns.

¹⁹Optics Software for Layout and Optimization from Lambda Research Corporation.

²⁰The reflectivity on the first surface amounts to 90(2) % for s- and p-polarized light, and to less than 1 % on the second surface.

²¹Thorlabs, Inc.

²²The specified reflectivity for 852 nm light is larger than 90 % while the transmittivity for light in the wavelength range between 866 nm and 895 nm is larger than 90 %. The reflectivity and the transmission are specified for s- and p-polarized light.

3.3.3. Discussion: Two-Color Magneto-Optical Trapping

On the one hand, the beam splitter after the objective lens provides the possibility to overlap the cooling beams with the imaging direction. On the other hand, the same beam splitter leads to a undesirable loss of 10 % of the fluorescence photons that reach the camera chip. In principle, a dichroic mirror could be used to separate these beams if magneto-optical trapping as well as molasses cooling were done at a different transition along this direction.

In references [108, 109], magneto-optical trapping of sodium using the D1-line has been reported. However, the drawback of this approach is the lower oscillator strength of the D1 line and the absence of a closed transition which requires higher powers required for the cooling and in particular the repumping laser beams. As a consequence, a relatively low number of atoms are cooled and trapped in this configuration compared to a MOT at the D2 line.

An alternative is the use of at least two wavelengths for cooling (“two-color MOT”). Such a configuration utilize the D2 transition in the horizontal plane and employ a different wavelength along the vertical direction. In references [110, 111] a two-color MOT for cesium has been reported using an additional transition to a higher energy level ($6P \rightarrow 8S$ transition) at a wavelength of 790 nm. However, this wavelength lies outside the range of our versatile optical coatings of the objective lens which needs to be optimized for the D2 transition to achieve high collection efficiency at large angles.

Thus, we tested a combination of the D2 and D1 lines for magneto-optical trapping — without success. We were not able to realize magneto-optical trapping in this configuration which indicates that it is either impossible, or that the number of trapped atoms is too low, or that it is very sensitive to parameters.

3.3.4. Cooling and Trapping of Atoms

In the experiment we use a power of 200 μW in all five beams of the cooling laser except the top beams which is set to a 40 % smaller power to match the beam intensities. The repumper light is overlapped along the horizontal beams and has a power of around 40 μW in each beam.

We observe trapped atoms at an exposure time of 35 ms by two cameras²³: camera 1 (DMK 72AU02) and camera 2 (DMK 23UP1300) as shown in figure 3.7. The two cameras allow us to align the MOT to the center of the objective and to the vertical position of the optical lattice which is positioned 150 μm below the surface of the objective. For magneto-optical trapping we typically use a magnetic gradient field of circa $75 \times 10^{-4} \text{ T/cm}$ since we want to have a good overlap with the dipole trap. In addition, we apply a vertical magnetic offset field – generated by the vertical compensation coil or an asymmetric current in the gradient coils – in the range between $8 \times 10^{-4} \text{ T}$ and $12 \times 10^{-4} \text{ T}$ to shift the zero field in front of the objective.

The $1/e$ -width of the cloud of atoms is 51.0(2) μm using a Gaussian model for a non-linear fit which actually states an average since the MOT is performing a random walk around its position with a standard deviation of 25 μm . A possible explanation of the continuous

²³The Imaging Source GmbH

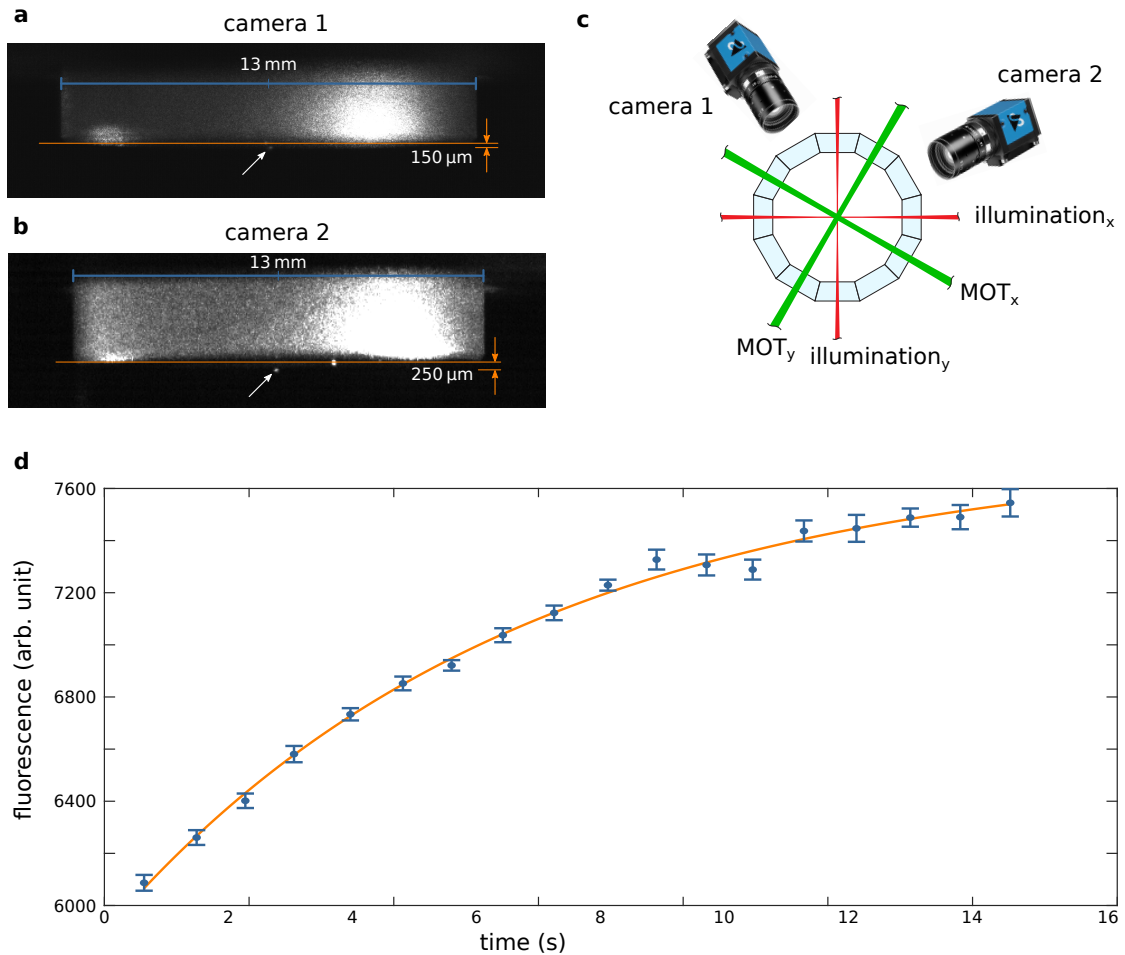


Figure 3.7.: (a) Image of a magneto-optical close to the surface of an objective and at a larger distance from a different angle (b). The white arrows mark the position of the MOT and the orange arrows indicate its distance from the surface of the objective. The setup of the cameras and the relevant beams is shown in (c). (d) Loading of the magneto optical trap by evaluating the integrated fluorescence of camera picture in a $13 \text{ px} \times 30 \text{ px}$ area in the picture.

movement of the MOT is given by local power imbalances in the horizontal beams due to residual diffraction lines in the clipped beam profile and small mechanical vibrations of the setup.

Integrating the total fluorescence of the atomic cloud in units of pixel brightness over a region of interest around the position of the magneto-optical trap yields the loading curve in figure 3.7(d). Under the assumption of low density, the loading process is described by a simple differential equation [82] for the number of trapped atoms N

$$\frac{dN}{dt} = R_L - \tau N, \quad (3.3)$$

where R_L is the loading rate and $1/\tau$ the decay constant due to collisions with background gases. A solution to the differential equation is given by $N(t) = N_s [1 - \exp(-t/\tau)]$, where N_s is to the number of atoms in the steady state. A non-linear regression of the exponential model to the data yields the decay constant $\tau = 5.7(4)$ s. Here, we implicitly assume that the detected fluorescence is proportional to the number of trapped atoms. The decay constant can be used to determine the background pressure if the dominant species of the background atoms as well as its scattering cross section is known [112]. Due to the high permeability of the vacuum glass cell towards water molecules we suppose that cesium atoms and water molecules provide the largest contribution of the background gas. This translates into a background pressure of $26(2) \times 10^{-10}$ mbar assuming a similar cross section of $\text{H}_2\text{O-Cs}$ and Cs-Cs [112]. The discrepancy towards the vacuum pressure of 3×10^{-10} mbar as measured by our ion pump can be partially explained by a differing scattering cross section with water molecules.

Reducing the driving current of the vertical compensation coils changes the position of the zero field, and thus the position of trapped atoms towards the objective as shown from different angles in figure 3.7(a) and 3.7(b). Furthermore, we observe a decrease in the total fluorescence emitted from the atomic cloud as it gets closer to the surface of the objective. The reason for the atom losses may arise from lower laser intensities, and from a lower collection efficiency of the cameras due to the blocking presence of the high numerical aperture objective and atom losses. Thus, in a typical loading sequence we start with loading the MOT at a distance of $500 \mu\text{m}$ in front of the surface of the objective for approximately two seconds and subsequently shift the trapped atoms to the position of the optical lattice ($150 \mu\text{m}$ to the objective).

4. Fluorescence Imaging of Atoms in a 3D Optical Lattice

Over the last decades far off-resonance optical lattices have become a standard tool in quantum optics to trap and transport neutral atoms in a deterministic and controlled way [113, 114] without altering its internal state. Recent advances in fluorescence detection of single atoms have been enabled by high numerical aperture (NA) objective lenses in the range of $0.60 < \text{NA} < 0.87$ [19, 29–33]. According to the Abbe criterion, the resolution of an objective at a wavelength λ_{D2} is given by $r_a = \lambda_{\text{D2}}/2\text{NA}$. However, in the context of optical lattices the ratio $R = r_a/L$ between the optical resolution r_a and the lattice spacing L is more meaningful to quantify the spatial resolution.

Optically resolving singles sites of an optical lattice is achievable for ratios $R \leq 1$. Larger ratios of R or short exposure times require special image processing techniques to reconstruct the position of point-like atoms [35] taking the point-spread function of the optical system as well as properties of the background noise into account. The resolution limit of these super resolution techniques [34] is given by [115]

$$(\Delta x)^2 = \frac{\text{rms}_{\text{PSF}}^2 + \Delta_{\text{px}}^2/12}{N_{\text{ph}}} + \frac{8\pi \text{rms}_{\text{PSF}}^4 \sigma_{\text{b}}^2}{\Delta_{\text{px}}^2 N_{\text{ph}}^2}, \quad (4.1)$$

where rms_{PSF} is the rms width of a Gaussian point spread function, Δ_{px} corresponds to the size of a camera pixel in the object plane, N_{ph} is the average number of detected photons per emitter, and σ_{b} is the rms background noise. While Eq. 4.1 states that single sites can still be detected with larger ratios of R when the signal-to-noise ratio is high, manipulating a single lattice sites with projected light beams will influence neighboring sites. Thus, smaller ratios render it impossible to achieve high state-preparation efficiency in optical lattice experiments. This contradicts the purpose of this experiment since we plan to project light patterns onto the atoms to achieve locally varying quantum walk coins, see chapter 6.

Obvious methods for decreasing R are to employ larger lattice geometries, e.g. microtraps [116, 117], smaller imaging wavelength or higher NA objective lenses [19, 29].

A further advantage of using a high NA objective lens is the ability to collect a high number of photons, i.e. photons within the solid angle [35]

$$\frac{\Omega}{4\pi} = \frac{1 - \sqrt{1 - \text{NA}^2}}{2} \quad (4.2)$$

which is required for fast (state-)detection [94].

In this chapter, the production of a new high NA objective lens consisting of two lenses with a combined $\text{NA}_{\text{design}} = 0.92$ is presented. The objective lens is further used to image

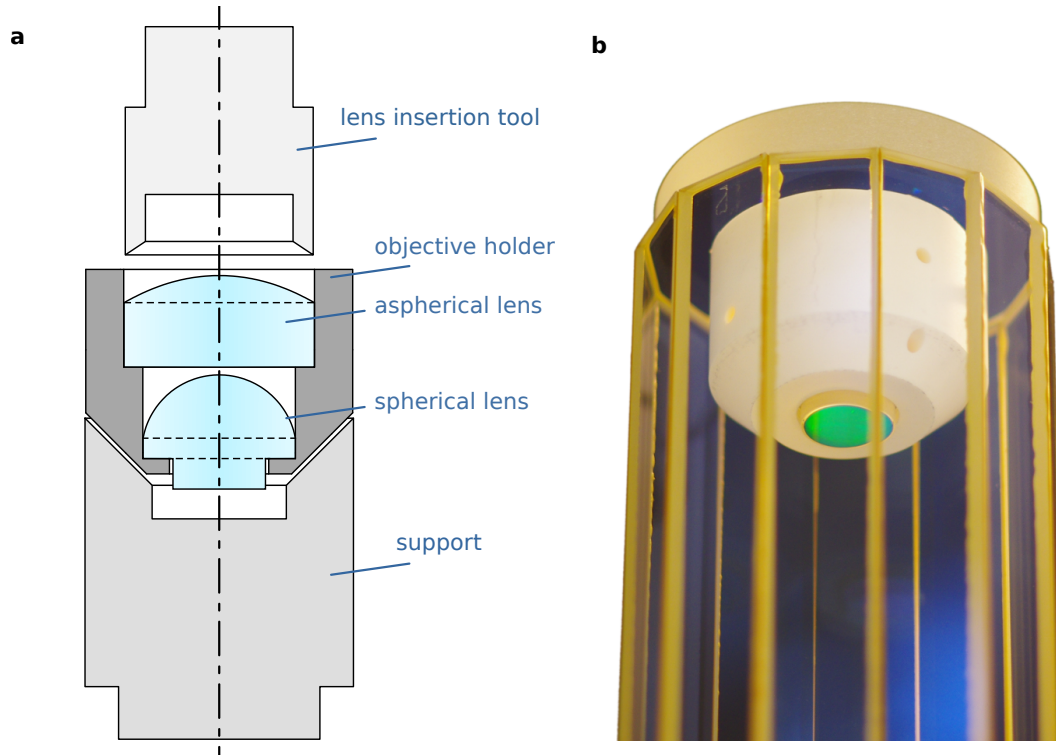


Figure 4.1.: Section drawing assembly tools (a) and mounted objective inside ultra-low birefringence glass cell (b).

single atoms in a three-dimensional optical lattice. These images are used to calculate lattice properties and to characterize the objective lens.

4.1. Development of a High Numerical Aperture Objective Lens

The existence of our high-NA objective lens is joint work of Carsten Robens (design, see [27]), Felix Kleissler (characterization, see [118]) as well as myself (assembly and characterization). The objective lens features a diffraction limited resolution at a designed numerical aperture of 0.92 and consists of two optical elements that are precisely aligned to each other by means of an aluminum oxide holder as shown in figure 4.1. The objective lens has to fulfill two main requirements: compatibility with ultra-high vacuum and high resolution at the imaging wavelength of the D₂-Line of Cs ($\lambda_{D_2} = 852 \text{ nm}$).

4.1.1. Optical Design

A detailed description of the optical properties and the design consideration of the objective lens can be found in [27]. Here, I want to briefly summarize the most important details. The two lens system comprises of a spherical (Weierstrass sphere) and an aspherical lens both made of N-SF10 glass [65]. A Weierstrass sphere, also known as aplanatic

solid immersion lens, is frequently used in microscopy to enhance the resolution of an optical system. In contrast to a hemispheric shape of a solid immersion lens, a Weierstrass sphere is elongated by r/n , i.e. the ratio of the radius r and the refractive index n of the material. As a result, the numerical aperture of the objective is increased by n^2 instead of n ($n_{\text{N-SF10}} = 1.709$). Both types of immersion lenses exhibit the feature that they do not cause spherical aberrations on the axis.

One surface of the second lens is planar while the other surface is polished to an aspheric shape in order to collimate the output beam of the objective. The numerical aperture of the second lens amounts to 0.35 showing the strong improvement in the numerical aperture due to the Weierstrass sphere. Almost all remaining aberrations are compensated by the aspherical surface to result in a diffraction limited operation at a wavelength of $\lambda_{\text{D2}} = 852 \text{ nm}$ at a working distance of $150 \mu\text{m}$. We regard a system as “diffraction limited” if it exhibits an on-axis Strehl ratio that is larger than 0.8. The Strehl ratio is defined as the quotient of the on-axis intensity of the lens system under test and the corresponding intensity of a point spread function of an ideal lens system for a given numerical aperture. The chromatic bandwidth determines the wavelength range where the on-axis Strehl ratio exceed 0.8 and amounts to $\pm 17 \text{ nm}$ for our objective lens. A working distance of at least $150 \mu\text{m}$ is necessary to trap atoms farther away from the first surface of the objective that might otherwise lead to clipping of lattice beams.

All surfaces are anti-reflection coated for the wavelength range $840 \text{ nm} - 900 \text{ nm}$ which is highly demanding for the front surface of the Weierstrass lens due to the large collection angle of $134^\circ/2$ corresponding to 30% of the solid angle. In addition, the plane surface of the Weierstrass lens is reflection coated for 1064 nm in order to retro-reflect a high power laser beam that forms an optical lattice along the optical axis of the objective lens. A further confinement of the position of atoms is necessary for high quality imaging since the depth of focus of the objective is given by $d = \pm \lambda_{\text{D2}}/2 \text{ NA}^2 \approx \pm 0.5 \mu\text{m}$. An atom trapped in this vertical lattice will therefore always stay within the depth of focus. The combined numerical aperture of the objective system is 0.92 yielding a theoretical resolution of $r_{\text{a}} = 460 \text{ nm}$. The ratio of the effective focal length of the objective (11.96 mm) and the tube lens will later define the magnification of the imaging system. The collimated beam diameter amounts to 22 mm which is still compatible with standard 1” optics. The field of view is characterized by the region where the system is operating diffraction limited and yields $b = \pm 35 \mu\text{m}$ which is in the order of 110 lattice sites of the horizontal lattice, see section 4.2.

In contrast to the objective lens presented here, high-NA objective lenses are typically made of many refractive surfaces to reduce aberration effects. Yet, our design is compact and achieves diffraction limited operation for monochromatic light and can easily be adapted to other wavelengths.

4.1.2. Mechanical Design

The design of the presented objective lens is robust against deterioration of optical properties if the mechanical manufacturing tolerances for a decentering or the distance of the two lenses are smaller than $1 \mu\text{m}$. The Weierstrass sphere is modified in diameter at the front surface to ensure a limit stop for alignment and to reduce clipping for lattice beams.

The alignment of the two lenses¹ is guaranteed by a precisely machined aluminum oxide holder² to meet the mechanical tolerances. The lenses are held in position by the vacuum compatible adhesive [119] that is also used in the production of the glass cell. The small working distance of 150 μm requires that the objective is placed inside an ultra-high vacuum, which is typically not possible with commercially available high-NA objective lenses. Small holes in the ceramic holder as well as three small “feet” at the collimated end of the objective enable evacuation of the inner volume of the objective lens. The ceramic material is chosen due to its thermal expansion coefficient of 8.1 /K [120] in the range [20 °C, 300 °C] that is matched with the glass cell and N-SF10 (10.8 /K). A thorough matching of the thermal expansion coefficients is mandatory to achieve an ultra-high vacuum due to the employed vacuum bake-out up to 150 °C [65].

4.1.3. Clean Room Assembly

Maintaining cleanliness is of utmost importance during assembly of high-NA objectives for use in ultra-high vacuum systems. For this reason, the hole assembly has been conducted in a class 100 clean room located in the Center of Advanced European Studies and Research in Bonn.

The procedure is as follows: After cleaning the ceramic holder thoroughly in an ultrasonic bath, the holder is held in place by an aluminum support with a conic shape, see figure 4.1(a). If necessary, the inner diameter of the ceramic holder can be enlarged by careful polishing with sandpaper of 1 μm grid³. However, care must be taken in order to maintain mechanical tolerances. Wrapped polishing sheets around a foam of cylindrical shape that fits into the holder allows us to homogeneously polish the inner surface without introducing further decentering of the two lenses. At first the spherical and subsequently the aspherical lens are pushed in place using a dedicated lens insertion tool made of Nylon which is limiting the direct contact with the lens surfaces to the outermost parts of the coated glass surfaces. A small droplet of the vacuum compatible adhesive is applied to the unpolished outer surface of each lens through small holes in the ceramic mount in order to fix the lens positions after a curing process similar to the one applied for the glass cell. In total two objective lenses were successfully assembled following the presented procedure. Unfortunately, the aspherical lens of one objective lens cracked during the curing procedure which is probably caused by the small distance between lens and its holder and the non-vanishing thermal expansion coefficient.

The optical performance of the objectives was roughly verified in the clean room by means of measuring the distortions of the wavefront of a laser beam – that is focused through the objective and subsequently retro-reflected by a silver mirror [118] – with a shearing interferometer⁴. Finally, the best objective is glued to the bottom surface of the top cell window using three tiny droplets of vacuum-compatible adhesive by imposing the glass cell on the supported objective and curing it in an oven. An image of the full assembled objective mounted in the ultra-high vacuum glass cell is depicted in figure 4.1(b).

¹custom made by Asphericon GmbH

²custom made by BeaTec GmbH

³Thorlabs, Inc

⁴SI254P from Thorlabs, Inc.

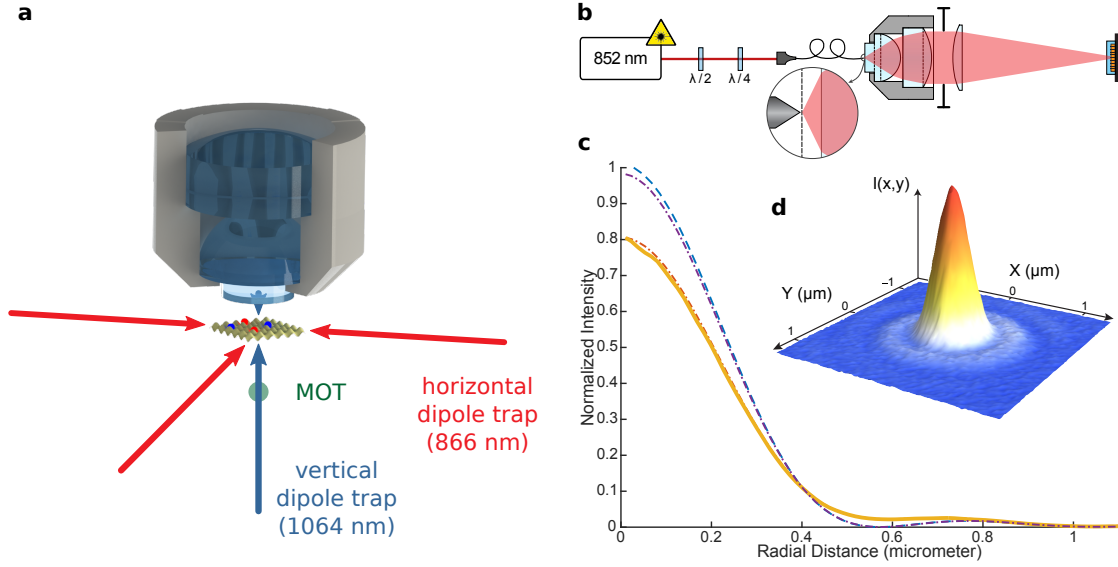


Figure 4.2.: (a) Rendering picture of the objective, a part of the holder and cesium atoms (blue and red dots) in a lattice (yellow). The green circles indicated the initial position of the magneto-optical trap as a source of cold atoms. The distances are not up to scale. (b) Setup to determine the point spread function (PSF) by imaging the tip of a SNOM fiber. In (c) the radially integrated PSF for measured (red), aberration fit (orange), ideal airy disk (blue) and fitted PSF without defocus (purple) are shown. (d) Image of the point spread function. Figures b-d are taken from [121].

4.1.4. Optical Characterization

Characterizing a high-NA objective lens is a demanding task by itself. Typical methods rely on the wavefront of the collimated beam or imaging an ideal point source [122].

Wavefront Analysis As mention in the previous section, both objective lenses have been characterized in the clean room by means of measuring the emerging wavefront with a shearing interferometer.

The limitation of a shearing interferometer consists in its capability to only detect local variations of the wavefront. Even though shearing plates with larger thickness cause farther separated parts of the wavefront to interfere, the spatial resolution is highly reduced such that a direct global analysis of the wavefront can only be done by integrating the resulting signal. Another method to determine the absolute wavefront over a detector size $5\text{ mm} \times 5\text{ mm}$ is utilizing a Shack-Hartmann wavefront sensor WFS150⁵ yielding an on-axis variation of $\lambda_{D2}/10$. Stitching of many wavefront measurements from different regions is in principle possible, but technically demanding for the required wavefront precision. Despite global wavefront detection the main limitation of this approach is given by the initial wavefront quality, polarization effects in high-NA objectives and the precise alignment of the mirror distance.

⁵Thorlabs, Inc.

Imaging a Point Source Instead of measuring the wavefront directly we image an ideal point source and infer the wavefront aberrations by analyzing its shape. The setup is depicted in figure 4.2: The light wave of a point source is collimated using the objective under test and imaged with a tube lens (focus length 750 mm) onto a beam profile camera Spiricon LW230⁶. The numerical aperture of the system is set with an automated iris IBM 65⁷. We tested different point-like sources as discussed in [118]:

- *Pinholes* A glass surface with gold layer of 200 nm thickness with holes $\varnothing = 100 \text{ nm} \dots 320 \text{ nm}$ has been thankfully produced by Johannes Overbuschmann at Caesar⁸. Unfortunately, the suppression of laser light by gold coating is extremely low (1:3000) probably due to surface roughness of gold layer due to sputtering process. A second sample featuring a 10 nm chromium layer between the glass and the gold layer in combination with an annealing stage at a temperature of 500 °C yields an improved suppression of 1:370 000. However, handling caused additional holes in delicate surface, and therefore, cannot be used for further analysis.
- *Nano-particles* placed at the surface of a prism that are illuminated by a laser beam at an angle of total reflection. The evanescent field is radiated at the position of the particles made of PMMA ($\varnothing = 400 \text{ nm}$) and TiO₂ ($\varnothing = 15 \text{ nm}$). The main limitations are caused by weak brightness and a strong dependence on the input polarization.
- *SNOM fiber tip* The tip ($\varnothing = 200 \text{ nm}$) of a aluminum coated fiber for a scanning near-field optical microscope E50-MONO780-AL-200⁹ withstands relatively high powers of up to 100 μW and exhibits a approximately Gaussian shaped angular radiation pattern [123]. The fiber is mounted on a three axis translation stage MAX302/M¹⁰ for precise alignment since the depth of focus is small and touching of surface must be prevented.

An image of the SNOM fiber tip is shown in figure 4.2(d) and translates into the radially integrated point spread function (orange) figure in 4.2(c). It only slightly differs from an ideal airy disk mainly due to the radiation characteristics of the fiber tip and the apodization function of the objective. Mathematically, the point spread function can be expressed as

$$\text{PSF} = \left| \mathcal{F} \left[P(x, y) E(x, y) e^{-2\pi i r(x, y)} \right] \right|^2, \quad (4.3)$$

where \mathcal{F} is the two-dimensional Fourier transformation, $P(x, y)$ the pupil function given by the aperture, $E(x, y)$ the electric field amplitude, and $r(x, y)$ the wavefront of the collimated beam. Apodization is an effect that results in a higher intensity of the collimated beam of the objective lens close to the aperture limit due to the spherical shape of the “principal plane”. The spherical plane originates from the Abbe sine condition [124] that is fulfilled for our objective [27]. The emission profile of a fiber tip can be modeled by a

⁶Ophir Optronics Solutions Ltd.

⁷Owis GmbH

⁸Center of Advanced European Studies and Research

⁹LovaLite SAS

¹⁰Thorlabs, Inc.

Gaussian angle distribution that might lead to a slightly lower estimation of the numerical aperture. Polarization effects play a crucial role in high-NA systems since a dipole radiation characteristic of a point source results in a reduced intensity at the collimated beam along the dipole orientation and an increased higher intensity perpendicular to this direction. However, by choosing circular polarized light we average over all linear polarizations leading to a tiny enlargement of the width of the PSF. We analyze aberrations by fitting the image to the calculated PSF of a lower-order Zernike (up to 3rd order) polynomial wavefront according equation 4.3 taking into account the distribution of the electric field $E(x, y)$.

The result is reported in [27] yielding a defocus of around 200 nm as the dominant remaining aberration. The corresponding point spread function as well as the calculated PSF without defocus is shown in figure 4.2(c). The resulting numerical aperture amounts to 0.936 and thus to larger value as originally intended by design. The discrepancy can be explained by a slightly larger aperture opening 22.3 mm instead of 22 mm of the automated iris. We conclude that the presented imaging system is exhibiting a Strehl ratio of 0.8 on-axis and can thus regarded as diffraction limited. According to the Zernike regression the Strehl ratio of our objective should even amount to 0.98 after a compensation of the small defocus.

4.2. Optical Setup to Image Individual Atoms

The setup to image single neutral atoms in a three-dimensional optical lattice is sketched in figure 4.2(a) and shown in more detail in figure 4.3. The lattice geometry is created by a combination of a one-dimensional state-independent dipole trap along the vertical direction and three interfering laser beams in the horizontal plane at a different wavelength forming two-dimensional the state-dependent lattice.

An experimental sequence starts with loading atoms in a magneto-optical trap for about 2 s at a position further away from the objective as explained in chapter 3. The center of the atomic cloud is moved towards the position of the optical lattice to transfer atoms into the lattice by altering the asymmetry of coil current for the gradient coils while the atoms are exposed to molasses and illumination beams. Finally, a fluorescence image of atoms in the three-dimensional lattice is recorded.

4.2.1. Optical Lattice Setup

Horizontal Lattice The three vertically-polarized laser beams in the horizontal plane form a square lattice geometry at the working distance of the objective lens. In the future, their polarization will be synthesized to realize state-dependent transport in two dimensions as reported in chapter 5. The laser beams have an elliptical shape in order to prevent clipping at the objective and to allow for a rather uniform intensity distribution within the horizontal plane. A good compromise for deep and homogeneous trapping potential over the field of view is given by a waist of 26 μm for the main axes of the ellipse in the vertical direction and 77 μm in the horizontal direction. In this case, a minimum distance of two times the beam radius between the center of the lattice beam and the first surface of the objective lens is maintained to limit stray light to an absolute minimum.

The laser light of the state-dependent lattice possess a wavelength of 866 nm as well as a power of 3 W and is generated by an Ti:Sapphire MBR 110¹¹ laser pumped by a Millennia eV 20¹² laser with 20 W output power at a wavelength of 532 nm. Back-reflections into the laser are suppressed by a 30 dB Faraday isolator FI-850-5SV¹³. The output beam is split into three beams that are transmitted via optical fibers to the vacuum apparatus, see figure 4.3 and individually controlled in intensity via separate acousto-optic modulators (AOM) 3080-122¹⁴ connected to Signadyne H3336F module. At the main table, see figure 4.3, some part of the three beams is split and guided onto photodiodes (PD_{1H}, PD₂, PD_{3H}) for intensity stabilization of the lattice beams with individual PID controllers¹⁵ (not shown). The other photo diodes are currently not in use but are mandatory for state-dependent transport scheme explained in chapter 5. Beam shaping is done by cylindrical lattice telescope that expand the beam out of the plane and focus it with a lens (focal length $F = 250$ mm) onto the atoms to form the desired elliptical shape with a power of up to 200 mW per beam. The corresponding trap depth amounts to $U_{\text{HDT}} = k_{\text{B}} \times 1.280 \mu\text{K}/\text{mW} \times P$, where P denotes the total sum over all horizontal beams and polarizations. It translates into the oscillation frequencies of single atoms inside the trap as discussed in section 5.2.1.

Vertical Lattice The vertical lattice needs to satisfy the two contrary requirements of strong confinement of atoms along the optical axis of the objective lens and a uniform radial intensity profile over the field of view. While the first requirement results from the short working distance of the objective, the second guarantees a homogeneous trap depth and light shift in a horizontal plane. Theoretically, a flat-top profile could perfectly fulfill the requirements. However, such profiles require beam shaping optics, e.g. Powell lens or cylindrical lens array, that introduce power losses or exhibit limitations on the uniformity [125]. A more practical alternative is the use of a Gaussian intensity beam profile with a relative large beam size of 77 μm which only exhibits a smooth, monotonous, radial decline of intensity. The resulting intensity change over a circle of 36 lattice sites in diameter amounts to 10 % and 35 % change over a circle of 110 lattice sites diameter (field of view), respectively. The vertical trapping beam is generated by a Mephisto MOPA¹⁶ laser system including a noise eater option and 25 W continuous-wave output power at a wavelength of 1064 nm that is protected against back reflections by a high-power single-stage optical isolator from Gsänger. The linearly polarized output power of the laser beam can be modulated by a AOM 3080-194¹⁷ connected to the Adwin Pro II¹⁸ system before it is transmitted into the fiber shown in figure 4.3. The transmitted light (up to 5 W) is overlapped with the bottom illumination beams by means of a short pass dichroic beam splitter DMSP1000¹⁹ and retro-reflected at the first surface of the

¹¹Coherent, Inc

¹²Spectra-Physics

¹³Qioptiq Photonics GmbH & Co. KG

¹⁴Gooche & Housego PLC

¹⁵proportional-integral-derivative controller

¹⁶Innolight GmbH, now Coherent, Inc.

¹⁷Gooch & Housego PLC

¹⁸Jäger Messtechnik GmbH

¹⁹ThorlabsInc.

4.2. Optical Setup to Image Individual Atoms

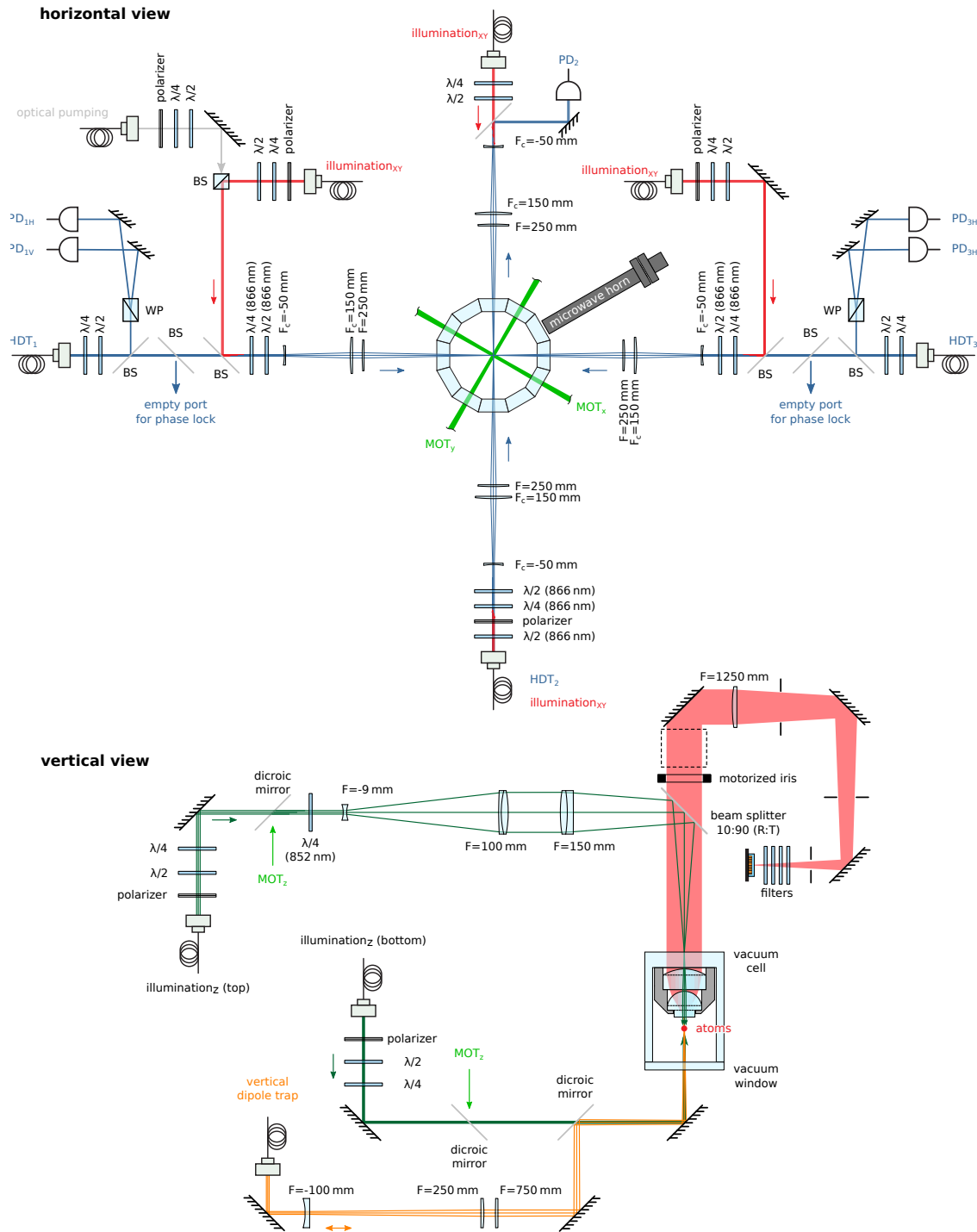


Figure 4.3.: Schematic drawing of the horizontal and vertical setup for taking fluorescence images of atoms in a three-dimensional optical lattice. The lattice is formed horizontally by three interfering laser beams (blue, 866 nm) and a retro-reflected laser beam (orange, 866 nm). Atoms are pre-cooled in a magneto-optical trap configuration (light green, 852 nm). Horizontally atoms in the lattice are cooled via illumination_{xy} beams (red, 852 nm) and vertically via illumination_z beams (dark green, 894 nm) The optical pumping beam (gray, 852 nm) is used for state preparation. See text for further details.

objective lens to form a standing wave trapping potential. The absolute value of the trap depth is predicted to be $330\ \mu\text{K}$ in front of the objective lens corresponding to an axial oscillation frequency of $190\ \text{kHz}$.

4.2.2. Illumination Setup

High-NA objective lenses suffer from optical access to cool atoms in optical lattices along the direction of the optical axis of the objective lens. Typical approaches for cooling are using a single molasses beam along this axis that is slightly tilted to [19] or shining beams through the objective lens [29]. We prefer to use illumination beams with a wavelength of $852\ \text{nm}$ in the horizontal plane and illumination beams with a wavelength of $894\ \text{nm}$ along the vertical direction which can easily be removed by narrow-band optical filters. The power in each horizontal cooling beam amounts to $500\ \text{nW}$ while the repumping and vertical beam intensities are the same as for the magneto-optical trapping.

The four horizontal illumination beams are overlapped with the direction of dipole trap beams by custom made pick up plates²⁰ (reflectivity of 6 % for s- and p-polarized light) for the circular polarized light. The vertical illumination beams are overlapped with the MOT beams by means of a long-pass custom-made dichroic mirror²¹, see section 3.3. The 10 % losses at the beam splitter cannot be avoided by the use of a polarizing beamsplitter cube since the fluorescence light of the atoms is effectively unpolarized and magneto-optical trapping at the D2 transition excludes the use of a dichroic mirror. The motorized iris behind the objective lens determines the effective numerical aperture of the objective lens, and thus, the depth of focus of the imaging system. Two bandpass filter for $852\ \text{nm}$ light (MaxLine laser²²) in combination with two notch filter for $1064\ \text{nm}$ light (NF1064-44²³) are placed in front of the electron-multiplying CCD²⁴ camera iXon Ultra 897²⁵. The optical filters guarantee a sufficient suppression of stray light caused in particular by the vertical dipole trap beam with a wavelength of $1064\ \text{nm}$ and the vertical illumination beams with a wavelength of $895\ \text{nm}$, respectively.

We use a tube lens exhibiting a focal length of $f_{\text{tl}} = 1250\ \text{mm}$ which results in a magnification of the imaging system of

$$M_{\text{th}} = f_{\text{tl}}/f_{\text{obj}} = 104. \quad (4.4)$$

4.3. Fluorescence Imaging of Atoms

The previously described setup is used to record raw images of atoms in a deep optical lattice with an exposure time of $300\ \text{ms}$, see figure 4.4(a). This exposure time is a good compromise between a high signal-to-noise ratio and a relatively short repetition time of the experimental sequence. Furthermore, the mechanical shutter of the camera required for protection against MOT beams needs about $20\ \text{ms}$ to fully open causing

²⁰Altechna

²¹Altechna

²²Semrock, Inc.

²³Thorlabs, Inc.

²⁴Charge Coupled Device

²⁵Andor

higher intensities in the center of the image. Shorter exposure times than 50 ms require an opening of the mechanical camera shutter prior to molasses illumination. It is reported in the literature that an etaloning effect of the back-illuminated electron-multiplying CCD camera leads to a spatial modulation of the intensity for homogeneous illumination with an amplitude of about 30 % [35]. Therefore, the first step of our image processing is to compensate the etaloning effect by multiplying each pixel of the image with the corresponding value in the sensitivity matrix shown in figure 4.4(b). The sensitivity matrix is determined as the inverse of the average over circa 1000 images using a low amount of scattered light of the MOT lasers at the outer coarse side of the first objective which is assumed to cause a homogeneous illumination at the camera position. We confirmed that the pattern is neither modified by exchanging any optical element in the imaging path nor by reducing the iris diameter but rather by a change in the temperature of the camera chip ($\Delta T = 50^\circ\text{C}$) as expected from the etaloning effect. However, additional mechanical vignetting in the region close to the left corners is caused by the small aperture of an optical filter positioned in front of the camera chip which will be exchanged in the future. A single atom in an optical lattice represents an ideal point source that can also be used to characterize the optical system since the typical extend of the atomic wavefunction in a deep optical potential amounts to a few tens of nano meter [126]. A shape of the recorded image of an atom is determined by the convolution of the extend of the wavefunction with the point spread function of the optical system, the discreteness of the sensor matrix plus additional optical and electronic noise contributions of the imaging system. In the cases where the optical system cannot resolve two adjacent lattice sites, advanced super resolution techniques must be applied in order to precisely reconstruct the lattice position [35]. These techniques attempt to inverse the convolution problem with precise knowledge of the point spread function and noise sources of the imaging system. Even high-NA systems with $R \approx 1$ profit from the knowledge of these parameters to reach high detection fidelities at low camera exposure times. Other experiments use simple Gaussians [31, 32, 127–129] or two superimposed Gaussians [30] as point spread functions for position determination.

4.3.1. Determining the Position of Single Atoms

This precise determination of the position of atoms is a mandatory prerequisite for the analysis of the point spread function for inferring lattice properties. Thus, to avoid stray light contributions from neighboring atoms, we focus on the detection of isolated atoms by a simple algorithm:

As a first step, candidates for regions of interests (ROI) are localized by selecting possible atom positions using a fast 2D peak search algorithm with a threshold of 1800 counts [130] and selecting a $32\text{ px} \times 32\text{ px}$ region around it. The fast 2D peak search algorithm determines local maxima based on observing intensity differences in a local $3\text{ px} \times 3\text{ px}$ region after median or Gaussian filtering.

Second, Fourier filtering is applied to each ROI in order to remove electrical noise contributions that exhibit significantly ($1.2\times$) higher spatial frequencies than the Abbe cutoff ($r_a^{-1} = 0.32\text{ px}^{-1}$). Following the procedure in [35], the images are subsequently up-sampled for higher spatial resolution ($16\times$) using the Whittaker–Shannon interpolation

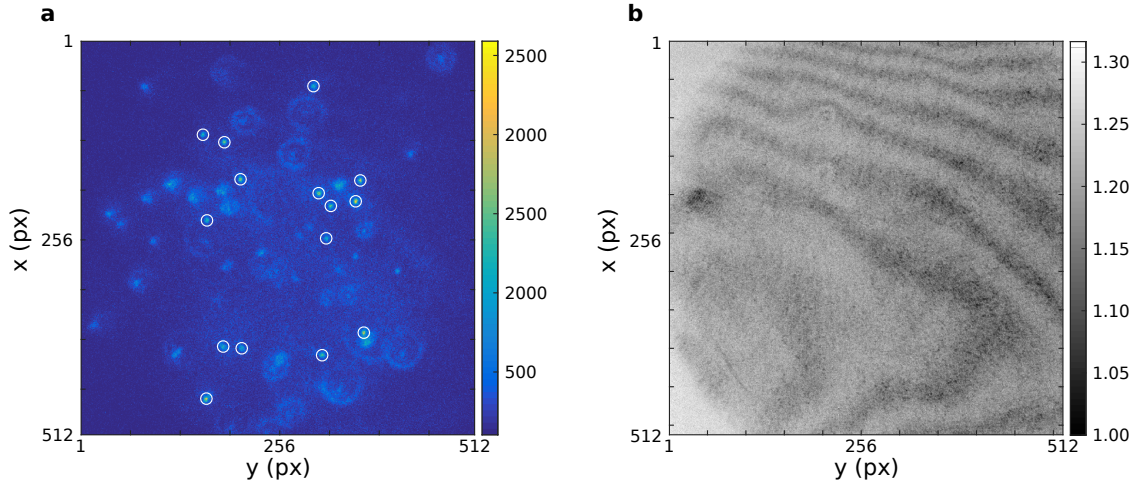


Figure 4.4.: (a) Typical image of single atoms in the three-dimensional optical lattice in arbitrary units. White circles indicate detected atoms. Background fluorescence is mainly caused by atoms that are out of focus of the imaging system as indicated by the strong defocus aberration, i.e. the rings. The darkening of the left corners within the image is caused by mechanical vignetting due to small optical filters. All camera images are corrected for the etaloning effect by the multiplication with the sensitivity matrix pixel by pixel. (b) Sensitivity matrix recorded as the inverse of the normalized average over many image of the etalon fringe pattern which is visible due to homogeneous illuminated of the camera chip with laser light.

formula. Both methods rely on the bandwidth limit (Abbe criterion) of the optical transfer function, i.e. the Fourier transform of the PSF.

In the last step, an elliptical 2D Gaussian function of the form

$$A \exp(-c_0(x-x_0)^2 + 2c_1(x-x_0)(y-y_0) - c_3(y-y_0)^2) + b \quad \text{with} \quad (4.5)$$

$$c_0 = \frac{\cos^2(\theta)}{2w_x^2} + \frac{\sin^2(\theta)}{2w_y^2}, \quad c_1 = -\frac{\sin(2\theta)}{4w_x^2} + \frac{\sin(2\theta)}{4w_y^2}, \quad c_2 = \frac{\sin^2(\theta)}{2w_x^2} + \frac{\cos^2(\theta)}{2w_y^2} \quad (4.6)$$

is fitted to each region of interest yielding the amplitude (A), the position in x - as well as y - direction (x_0, y_0), the width (along minor w_x and major axis w_y), the tilt angle of the major axis (θ), and a background intensity (b). An atom is regarded as detected if the regression yields values of the widths in the range of $0.5 \text{ px} < w_{x,y} < 4 \text{ px}$ and a RMS²⁶ error of the residual of the regression smaller than 0.2. In addition, the image of each accepted region of interest is shifted such that the center of the fitted Gaussian coincides with the center of the upsampled image.

Note that a Wiener deconvolution in combination with a threshold criterion could also be used for finding the regions of interest if the PSF is already known. However, this procedure results in a two times larger execution time while it does not improve the

²⁶Root Mean Squared

localization precision since it is mainly determined by the final regression. Single detected atoms are indicated by white circles in the exemplary image shown in figure 4.4(a).

Limitations Atoms located in a lattice plane outside the depth of focus of the objective lens suffer from enhanced aberrations resulting in blurred peaks or intensity rings. These atoms create a significant intensity background across the field of view, and hence degrade the detection efficiency of the presented algorithm. In principle, background atoms might even be used to improve on the characterization of the optical aberrations if their exact position is known via e.g. plane selection, see section 4.3.3.

In total 2250 atoms which are shown in figure 4.5(a-c) have been identified by the algorithm. Even though each image is multiplied pixel by pixel with the sensitivity matrix, i.e. the inverse of the fringe pattern, the position coordinates of all atoms clearly reveal the interference pattern of the camera chip. However, the absence of detected atoms in the “bright” areas of the sensitivity matrix may arise from an incomplete compensation of the etaloning effect of the camera chip and the lower signal to noise ratio in these regions.

Furthermore, the regression of the elliptical Gaussian function to the images of single atoms favors an ellipticity as a consequence of the patterned background intensity caused by out-of-focus atoms.

4.3.2. Analyzing the Point Spread Function with Pictures of Single Atoms

Using the up-sampled images of isolated single atoms allows us to determine the point spread function. For this purpose, we need to select atoms that are positioned in the working distance of the objective lens by their fitted Gaussian regression model. Our criteria for in-focus atoms are:

- The amplitude of the Gaussian is in the range between 3200 and 4000 counts since smaller amplitudes correspond to out-of-focus atoms and higher intensities to possible noise events caused by cosmic particles.
- The corresponding widths for the major and minor axis amounts to values smaller than 1.8 px to sort out spatially bunched occurrences of atoms.
- The fit quality in terms of the RMS error of the residual is smaller than 0.03 counts.
- Shape of the atom image is approximately radially symmetric, in order to remove contributions from neighboring atoms.

Only 13 atoms out of the whole data set fulfill these criteria. These atoms are highlighted by the orange color in contrast to all other atoms (blue) as shown in figure 4.5(a-c). Our first guess that in-focus atoms are positioned close to the optical axis of the objective lens, i.e. in the center of the images, is not exhaustive since three of these atoms are located farther out of this region in the lower right corner (c). The average of the up-sampled images of the selected atoms is plotted in figure 4.5(d) along with an image (e) of a wavefront regression using low order Zernike polynomials similar to the one applied in section 4.1.4. In this case we do not use the assumption apodization and the dipole

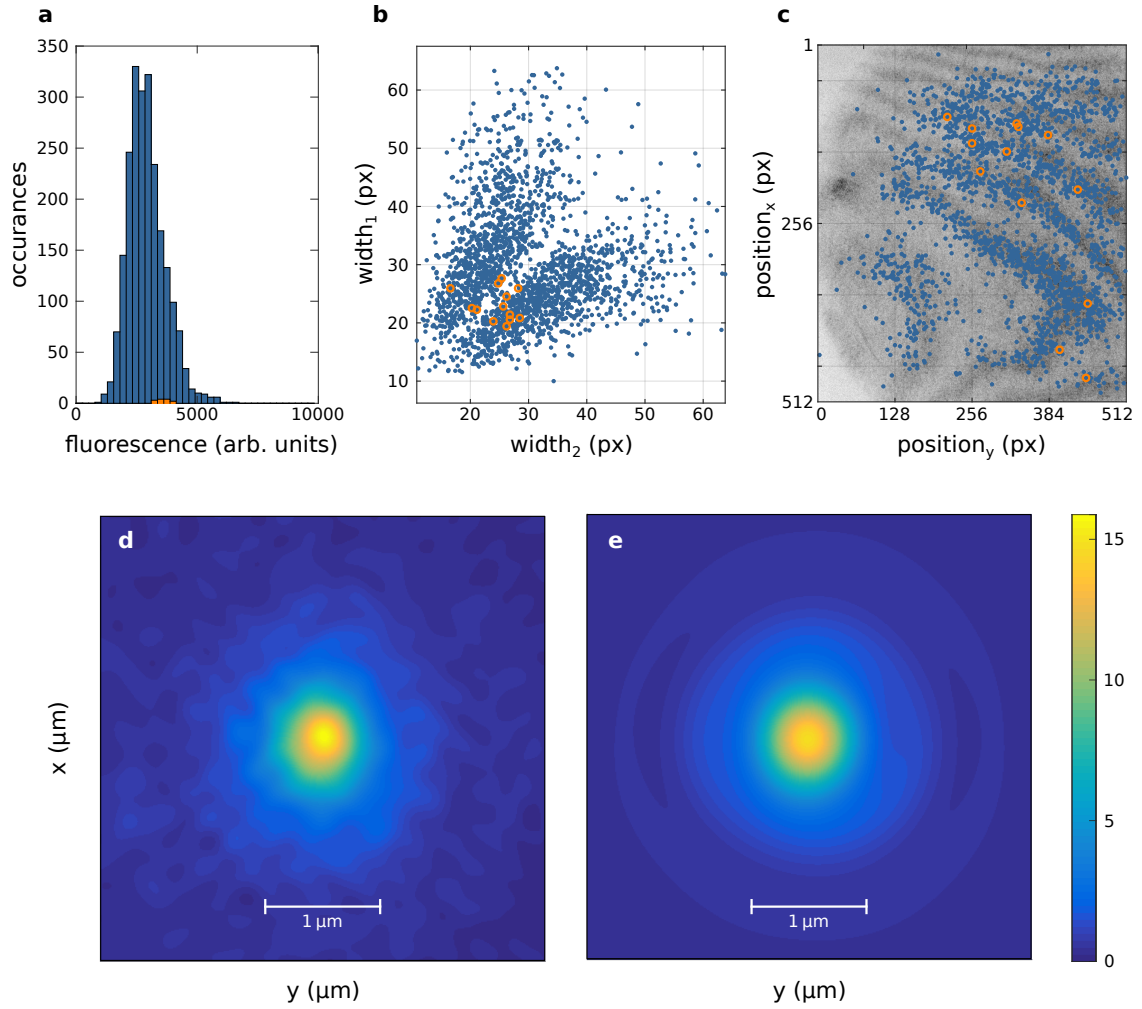


Figure 4.5.: Visualization of all detected atoms: (a) Histogram of fitted atom amplitudes. (b) Fitted atom width correlation of the up-sampled ($16\times$) images. (c) Position correlation of the fitted atom positions overlapped with the sensitivity matrix. The orange color indicate selected atoms which are used to reconstruct the up-sampled PSF (d). (e) The resulting PSF of a global optimization (see main text) of the aberrations in lower order Zernike polynomials similar to 4.1.4 yielding a Strehl ratio of 0.51.

radiation characteristics of single atoms since they do not contribute significantly to the wavefront distortion. However, we integrated an additional convolution with the pixel size of the camera ($16\ \mu\text{m} \times 16\ \mu\text{m}$) due to the relatively small spatial sampling frequency (four pixels per Abbe radius) that had to be chosen to image the whole field of view onto the camera chip.

Most of the resulting coefficients of the Zernike polynomials, see table 4.1, are relatively small except for the strong components of defocus and the components of spherical aberration. Their combination leads to a unsatisfactory Strehl ratio of about 0.51 and a fitted numerical aperture of 0.69 which is much lower than the measured numerical aperture during imaging the light emitted by a SNOM-fiber tip, see section 4.1.4. Where do these differences originate from? A lower numerical aperture may arise from clipping of the output beam at filter frames or apertures used for stray light reduction along the imaging path despite the careful alignment of these elements. This is in accordance to a another experiment in our group where a similar relative difference between the desired and the measured numerical aperture with single atoms is observed [35]. We attribute the strong defocus and the resulting low value of the Strehl ratio partially to the averaging of the point spread function over the selected atoms that might contain atoms that are out of focus. Furthermore, a reduction of the Strehl ratio is caused by an incomplete alignment of the position of the objective and the tube lens. So far, the distance of the atoms to the objective lens is only known up to an accuracy on the order of the width of the horizontal lattice beams ($26\ \mu\text{m}$) and a few centimeters for the distance between the tube lens and the camera, respectively. While small deviation from the designed working distance of the objective lens can be compensated, a deviation of about $7\ \mu\text{m}$ causes a decline of the Strehl ratio of the combined optical system by a factor of two. A more precise alignment procedure could be realized by deterministic preparation of atoms in a single plane. In this case the absence of background atoms would lead to clearer images and a better signal to noise ratio. Optimal lens positions are achieved by inferring the point spread function for various distances between the atoms and the objective lens as well as between the tube lens and the imaging camera, see chapter 6. However, a real-time implementation of the global optimization routine using Zernike polynomials seems to be unfeasible due to the required computing time of the global optimization fit routine.

As an alternative, the width of the point spread function which is determined by fitting a simple 2D Gaussian regression model is sufficient to optimize the imaging system. Applying a Gaussian profile to our data yields a width of $\sigma = 1.806(2)$ px in the original picture which corresponds to $278(3)$ nm in the object plane. This width translates into the numerical aperture of an airy disk under the assumption of $\text{NA}' = 0.22\ \lambda_{\text{D2}}/\sigma = 0.671(2)$ from [131] which is in good agreement with the numerical aperture determined by the method base on Zernike polynomials.

Brightness Considerations The total number of fluorescence photons per atom reaching the camera chip is given by

$$N_{\text{ph}} = \Gamma/2 \cdot s \cdot \text{CE} \cdot \eta_{\text{eff}} \cdot \Delta t, \quad (4.7)$$

where s is the saturation parameter, $\text{CE} = 4\pi [1 - \cos(\arcsin(\text{NA}))]/2$ the collection efficiency of the objective lens, $\eta_{\text{eff}} = 76\%$ the transmittance of the optical path (losses

Table 4.1.: Table of Zernike aberrations calculated from global optimization routine for the measured point spread function. All values are given in units of λ_{D2} .

position X	position Y	NA	defocus	astigmatism V	astigmatism H	coma V
-0.0110	-0.0168	0.6897	+0.1243	-0.0135	-0.0001	-0.0017
coma H	trefoil V	trefoil H	spherical	astigmatism 2nd order V	astigmatism 2nd order H	Strehl ratio
-0.0042	+0.0025	+0.0026	+0.0219	-0.0052	+0.0024	0.507

due to beam splitter and optical surfaces), and $\Delta t = 0.3$ s exposure time of the camera. Converting the number of photons into ADC counts of the camera yields

$$N_{\text{ADC}} = N_{\text{ph}} \cdot \eta_{\text{CCD}} \cdot g \cdot \alpha^{-1} \quad (4.8)$$

where $g = 1000$ denotes the combined gain of the electron multiplying stage and conventional gain stage, $\eta_{\text{CCD}} = 0.6 e^-$ is the quantum efficiency of the camera sensor, and $\alpha = 52.3 e^-/\text{counts}$ represents the conversion factor between electrons and ADC counts according to the data sheet of the camera. In total, under the assumption of $s = 1$, we expect an integrated atom brightness of approximately 1.6×10^8 counts for the full numerical aperture of 0.92 and 7.4×10^7 counts for the measured value 0.69, respectively. Instead, we infer the value 7.2×10^4 counts by integrated over the 2D Gaussian regression model of the point spread function corresponding to a saturation parameter of 1/2300 in the case of $NA = 0.92$ and 1/1030 for the lower numerical aperture. Reported values for s in the literature are in the range of $1/10 < s < 1/30$ [35, 99] for a pure D2-line illumination, and thus, strongly deviate from our values for an illumination with a combination of the D1- and D2-line. The use of the D1 line is expected to reduce the total scattering of photons at the D2 line by 1/3 due to a relative oscillator strength of 1:2 (D1:D2) [98]. However, the remaining discrepancy of about an order of magnitude is not understood. Possible explanations include losses due to clipping along the optical path, a degradation of the EMCCD amplifier stage, and suboptimal settings of intensity and detuning parameters for the two-color molasses cooling used for fluorescence imaging.

Resolution Limit Following equation 4.1, we obtain a super resolution limit of $\Delta x_{0.7} = 18$ nm for the current status of the characterized imaging system. Here, we have assumed that the camera detects $N_{\text{ph}} = 6240$ photons per atom and that the width of the Gaussian PSF amounts to $\text{rms}_{\text{PSF}} = 1.8 \text{ px} = 277$ nm as calculated from atom pictures. Furthermore, we have used the that the standard deviation of the background noise is given by an equivalent of $\sigma_b = 6$ photons and that the size of each camera pixel corresponds to $\Delta_{\text{px}} = 16 \mu\text{m}/103.5 = 154$ nm in the object lane. In principle, we expect to reach a super resolution of $\Delta x_{0.92} = 0.1$ nm for the correctly aligned imaging system featuring our objective lens.

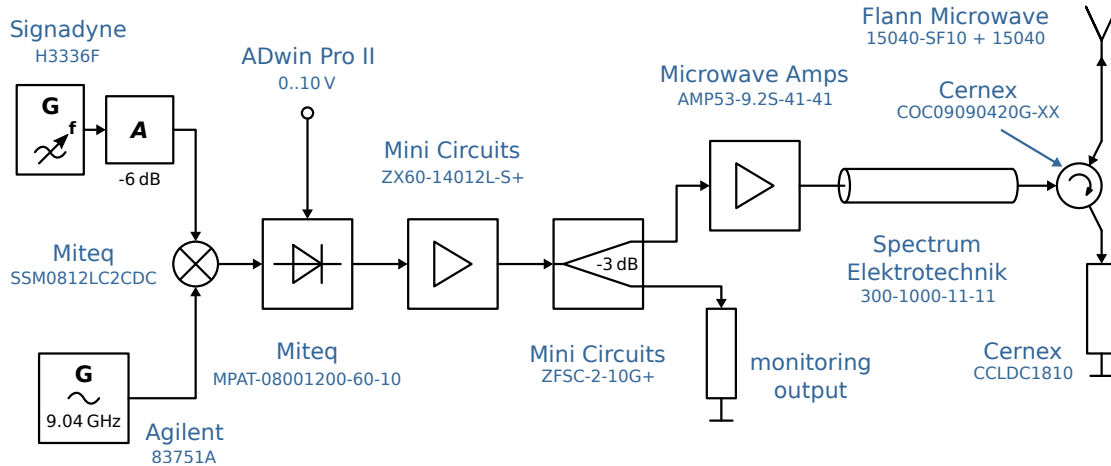


Figure 4.6.: Microwave setup: A phase and frequency synthesized signal generated in a Signadyne H3666F module is mixed in a single sideband upconverter with a fixed frequency reference at 9.04 GHz. Pulse shapes are generated by applying a voltage to a PIN (Positive Intrinsic Negative) diode to attenuate the combined microwave signal. This resulting signal passes a preamplifier, a power splitter for monitoring purposes and a high power amplifier to yield powers up to 41 dBm at the open end of a microwave waveguide that is placed a few millimeters away from the glass cell. Back reflections are guided to a terminator by means of a circulator. They can arise from an improper coupling of the microwave signal into the low loss cable or the waveguide as well as from reflections at metal parts of the apparatus, for instance the metal shielding.

4.3.3. Outlook: Selecting a Single Plane of Atoms

A precise aligning the imaging system to reach the design characteristics is only achievable if the position of imaged atoms is known e.g. by selectively removing undesired atoms from the three-dimensional lattice. As a positive side effect a single plane of atoms improves the imaging by avoiding stray light influences caused by out-of-focus atoms, like in [128]. Preparing a single plane of atoms is similar to addressing a single lattice site which has been achieved by superimposing a lattice of different wavelength [132–134], light shifts originating from focused laser beams [78, 135–138], or magnetic field gradients to induce spatial varying transition frequencies that are resolved by nuclear magnetic resonance (NMR) techniques [31, 76–78]. Superimposing an additional lattice demands for a stable relative phase between both lattices. Furthermore, a constructive (red-detuned) or destructive (blue-detuned) interference at the working distance of the objective within a tolerance of about $\pm 1 \mu\text{m}$ needs to be guaranteed. To comply with this small tolerance requirements is a demanding task for an experimental implementation. Projecting light sheets as a dimple trap depends on strong focusing of a laser beam from the horizontal side parallel to the objective surface, and thus cannot be directly applied [139] in our setup using the objective lens.

Thus, we are currently preparing a setup using the NMR technique in a position dependent magnetic field to select a plane: Initially, all atoms are prepared in the state

$|\uparrow\rangle = |F = 4, m_F = 4\rangle$ of the cesium hyperfine ground state $6^2S_{1/2}$ by means of optical pumping with a σ^+ polarized laser beam at the $|F = 4\rangle \rightarrow |F'' = 4\rangle$ cycling transition in the horizontal direction, see section 3.3. During initialization, the quantization axis is defined by a weak magnetic field (2×10^{-4} T) which is aligned to the direction of the two counter-propagating lattice beams in the horizontal direction. It is subsequently rotated into the vertical direction by adiabatically driving the current from the x-compensation coils to z-compensation coils within a few milliseconds (compare figures 4.3 and 3.1). In addition, a quadrupole magnetic field generated by the gradient coils (see section 3) results in a gradient field along the radial (r) and vertical (z) direction

$$B(r, z) = \begin{pmatrix} 0 \\ -B_0 \end{pmatrix} + \nabla B \begin{pmatrix} r/2 \\ -z \end{pmatrix}. \quad (4.9)$$

Here, B_0 denotes the strength of the offset field defining the quantization axis and ∇B indicates the resulting magnetic gradient of up to $\nabla B = 300$ G/cm = 0.016 G/ $(\lambda_{\text{VDT}}/2)$ for the reported coils. Pulsed microwave radiation couples the state $|\uparrow\rangle$ to the state $|\downarrow\rangle = |F = 3, m_F = 3\rangle$ at a position-dependent transition frequency up to second order in spatial directions (r, z) [76]

$$\omega(r, z) = \omega_0 + \gamma |B(r, z)| \quad (4.10)$$

$$\approx \omega_0 + \gamma \left(B_0 + \nabla B z + \left(\frac{\nabla B}{\sqrt{8B_0}} r \right)^2 \right) \quad (4.11)$$

$$= \omega_0 + \delta_0 + \Delta\omega z + \frac{(\Delta\omega)^2}{8\delta_0} r^2. \quad (4.12)$$

In this equation, ω_0 corresponds to the splitting between $|\uparrow\rangle$ and $|\downarrow\rangle$, the gyromagnetic ratio is denoted as $\gamma \approx 2\pi \times 2.5$ MHz/G and the guiding field shift $\delta_0 \equiv \gamma B_0$ and a position-dependent shift $\Delta\omega \equiv \gamma \nabla B$ are introduced. We expect to achieve differences in the transition frequencies of circa $\Delta\omega = 2\pi \times 40$ kHz per lattice site which is larger than what is required to select a single lattice site (13 kHz) [76] or a lattice plane (14 kHz) [78]. The quadratic dependence on the radial direction r limits the selection radius of a plane. However, this effect can be reduced via increasing δ_0 by either stepping up the guiding field or equivalently by driving the gradient coils with an unequal current which offers larger maximum field shifts. Due to a misalignment of the lattice relatively to the coils of about a millimeter, we expect to have an equivalent guiding field of around 30 G without further compensation. In first order approximation, selecting the desired microwave frequency using the assembled setup shown in figure 4.6 allows us to transfer the internal state of atoms in a plane from $|\uparrow\rangle$ to $|\downarrow\rangle$. A short pulse of a so-called ‘‘push-out’’ [36] – realized by the σ^+ polarized top MOT beam – resonantly heats all remaining atoms in $|\uparrow\rangle$ out off the optical lattice with reduced potential depth. The push-out pulse length needs to be short enough to avoid off-resonant excitations that lead to a population of the $|\downarrow\rangle$ state. As a first step towards plane selection, we were able to record the population relaxation time (T_1) [36], see section 6.1.

Another idea to infer information of the distance between the atoms and the objective is making use of a position-dependent point spread function, for instance a helical structure where the rotation angle determines its position along the optical axis [140, 141].

4.4. Characterization of the Optical Lattice

The three interfering beams in the horizontal plane ideally form a square lattice (figure 4.2) whose symmetry axes are eventually rotated relative to the pixel grid of the camera chip. Deviations of the rectangular angle between lattice beams lead to separate lattice spacings and tilts for translation symmetry axes, as discussed in more detail in section 5.2). Revealing the geometry of the optical lattices can, in principle, be done by free space imaging of a Bose-Einstein condensate that maps the crystal momentum into momentum distribution of atoms [28, 142], which is similar to x-ray diffraction at solid state crystals. Different methods for high-NA objectives depend on their capabilities to resolve single sites of an optical lattice by e.g. maximizing the intensity at each lattice site for an assumed lattice configuration [32]. Alternatively, the width of peaks in histograms of detected atom positions along an axis in a rotated is minimized for a certain angle that corresponds to the lattice tilt, while the distance of the peaks transfer into the lattice spacings [19, 129].

Alternatively, the center and the minimum width of peaks in histograms of detected atom positions along the axes of a rotated frame at a certain angle [19, 129] lead to a determination of lattice spacings and tilts. Here, I present more precise methods to infer the lattice constants and tilts from atom positions.

As a first step the $N = m \cdot n(n - 1)/2 = 1\,085\,182$ relative atom distances $\delta l_i(\alpha)$ along the coordinates are calculated for n detected atom positions, within each picture, of all m pictures. The relative atom distances are calculated in a frame that is tilted by an angle α to the pixel grid of the camera.

4.4.1. Detection Precision

A large fraction of the relative difference $\delta_i(\alpha)$ is shown in the two-dimensional histogram, see figure 4.7(a). The result of the next subsection is used to calibrate the axis in units of lattice sites and rotate the relative distances for the lattice tilt. The figure is limited to a square of 60 lattice sites since the number of atoms at a larger distance is significantly reduced due to the finite size of the optical lattice plane. However, relative distances up to 90 lattice sites are still arranged in clear lattice geometry. The clear periodic structure within the histogram proves the absence of significant distortions in the imaging optics that otherwise could deteriorate the detection of atom positions for large distances.

By performing a modulo operation with the lattice spacing, all relative distances are folded into a histogram of unit cell which is shown in figure 4.7(b). We attribute the global background to erroneous detection of atom positions that might occur due to fluorescence light originating from out-of focus atoms, as discussed in the previous section. An uncorrelated uncertainty in the detection algorithm to infer the position of atoms (see section 4.3.1) can lead to a radially symmetric distribution. However, the measured distribution exhibits this circular shape only in its center while it adapts the rectangular elsewhere due to additional position correlations that increase the number of detected atoms along the diagonal. These correlations are spatially overlapped with the directions of the three laser beams that are generating the optical lattice. Thus, we attribute this correlations to fast lattices drifts along two independent directions caused by fluc-

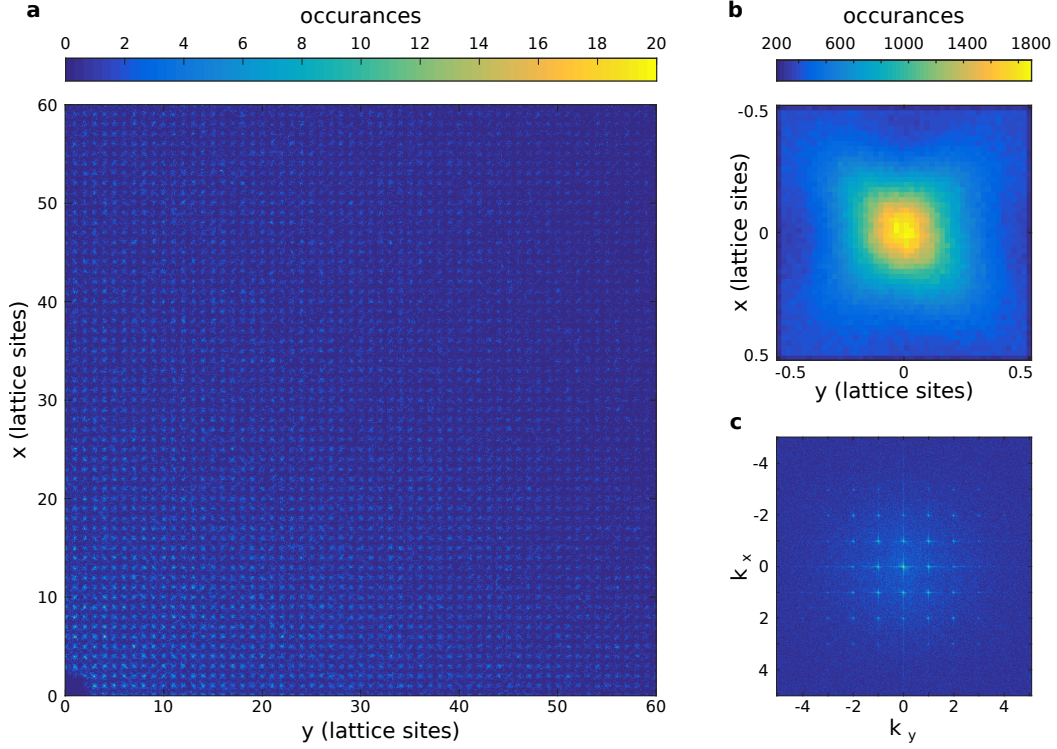


Figure 4.7.: (a) Histogram of circa 1 085 000 relative atoms distances for an rotation angle $\alpha = -3.3901(3)^\circ$ between the camera and the optical lattice. The lower left corner is left blank due to an intentional restriction in atom detection procedure where only well isolated atoms should be detected. (b) Histogram of all relative distances folded into the unit cell for a lattice spacings of 3.946 20(5) px along the x-direction and 3.981 67(2) px along the y-direction, respectively. (c) Fourier transform of the 2D histogram corresponding to the reciprocal plane.

tuation in the optical path length during the recording of images. The RMS-width of this distribution specifies the detection precision and amounts to 0.157(2) lattice sites in the x-direction and 0.159(2) lattice sites in the y-direction, respectively. The discrepancy between this width and the super resolution limit of 18 nm (0.03 lattice sites) for the current status of the imaging system remains topic of further investigation when the plane selection method to improve the detection accuracy.

4.4.2. Tilt and Spacings

The first method (method 1) to determine the lattice properties, i.e. the lattice spacing and lattice tilt, relies on the Fourier transform of the histograms (bin width 1/10 px) of atom positions along one tilted direction at angle α as shown in figure 4.8(a). The spectra reveal a periodicity of the histogram - and thus, the lattice spacing - at a spatial frequency of circa $L_x^{-1} = 0.25 \text{ px}^{-1}$ indicated by the strong Fourier component whose amplitude varies with α . Fitting a Gaussian shape to the Fourier component yields the

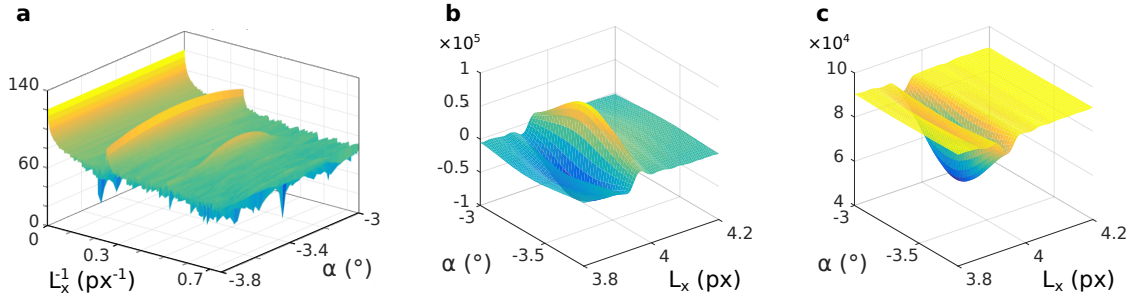


Figure 4.8.: Determination of lattice properties in x-direction: (a) Fourier spectrum of the histogram of binned atom positions (bin-width of $1/10$ px) for different lattice tilts α . (b,c) Evaluation of the function $f_1(L, \alpha)$ and $f_2(L, \alpha)$ (see main text) using the same position data.

lattice spacing by the inverse of the corresponding frequency and the lattice tilt by the angle α at which the Fourier component reaches its maximum amplitude. The second method (method 2) does not depend on a binning procedure but on finding the zero crossing of the function

$$f_1(L, \alpha) = \sum_i \frac{(\delta l_i(\alpha) \bmod L) - L/2}{\delta l_i(\alpha)}, \quad (4.13)$$

where “ $a \bmod b$ ” denotes the modulo operation that vanishes if the relative distances are a multiple of the assumed lattice spacing. The denominator is required for normalization. The dispersive shape of $f_1(L, \alpha)$ is shown in figure 4.8(b) where the same data as in method 1 has been used. The position of the zero-crossing determines the lattice spacing while the lattice tilt is given by the position of maximum contrast of the dispersive shape. The reported values are extracted from $f_1(L, \alpha)$ by regression with a model function that is the product of a Gaussian distribution along the tilt coordinate and a first derivative of a Gaussian distribution along the spacing coordinate. While this model is capable of describing the dispersive shape of the data sufficiently it systematically differs from the data at regions of highest and lowest amplitude.

The third method (method 3) is a slightly modified version of method 2 and requires minimization of the function

$$f_2(L, \alpha) = \sum_i \left(\frac{([\delta l_i(\alpha) + L/2] \bmod L) - L/2}{\delta l_i(\alpha)} \right)^2 \quad (4.14)$$

since its value is positive everywhere and is expected to vanish at the real lattice spacing. As shown in figure 4.8(c), the evaluated function can be well approximated by a simple 2D Gaussian regression model yielding the two lattice spacings and tilts.

The inferred values of the lattice spacing and tilt for both lattice directions using methods 1-3 are listed in table 4.2. We deduce that all presented methods allow for a precise determination of the lattice spacings and tilts with a factor of ten improvement in the accuracy relative to the binning method used in reference [19]. The values in table 4.2

Table 4.2.: Overview of lattice properties estimated with the presented methods. Confidence intervals (0.68) are derived from the regression.

	method 1	method 2	method 3
$\alpha_x(^{\circ})$	-3.407(3)	-3.402(2)	-3.4035(7)
$\alpha_y(^{\circ})$	-3.373(2)	-3.377(1)	-3.3767(2)
$L_x(\text{px})$	3.9334(9)	3.9456(1)	3.946 20(5)
$L_y(\text{px})$	3.9684(8)	3.9816(1)	3.981 67(2)
$L_x(\text{nm})$	607.6(1)	609.52(2)	609.614(8)
$L_y(\text{nm})$	613.0(1)	615.08(1)	615.094(3)

justify the assumption that our lattice can be described as a rotated rectangular lattice with two slightly different lattice spacings. The average lattice tilt $-3.3901(3)^{\circ}$ relative to the camera chip can be further decomposed into a rotation angle that is caused by a misalignment of the lattice beams as well as a tilt of the camera chip (see section 5.2). The angle caused by misalignment is calculated by the ratio of both lattice spacings according to equation 5.11 and amounts to a very small rotation angle of $-0.2563(3)^{\circ}$ which is proving that all beams are well aligned. Older atom images yield a lattice tilt of $-0.1230(5)^{\circ}$ indicating that the lattice characterization needs to be performed after every realignment of the optical lattice beams.

The results of an analysis of subsequent data sets which have been recorded during a the time period of a day is shown in figure 4.9(a-d) providing no evidence for systematic drifts or changes in the lattice spacings and tilt. Note that, while the reported errorbars are inferred from 0.68 confidence intervals of the regression, the widths of the fitted distribution are about a factor of 10 larger than the statistical errors of all methods. Thus, we conclude that the physical alignment is reasonably stable during this time period to reprehensibly exhibit the same lattice properties.

In addition, all presented methods have been tested with simulated atom positions that obey a small position uncertainty of 0.2 lattice sites indicating that all methods enable a reconstruction of the lattice properties up to one parts per thousand. The advantage of method 2 and method 3 is their accuracy in the cases where only a small number of relative distances (around 20 000) is available. In the following sections, we use the lattice properties determined via method 3 since they are the most accurate ones.

Magnification The knowledge of the lattice spacing allows us to determine the magnification of our imaging system precisely by evaluating

$$M_{\text{exp}} = \sqrt{2} \Delta_{\text{px}} \bar{L} / \lambda_{\text{HDT}} = 103.5723(6), \quad (4.15)$$

using the mean inferred lattice spacing $\bar{L} = \sum_{i=x,y} L_i$, the camera pixel size ($\Delta_{\text{px}} = 16 \mu\text{m}$) and the knowledge of the standing wave spacing $\lambda_{\text{HDT}}/\sqrt{2}$ due to the lattice wavelength $\lambda_{\text{HDT}} = 866 \text{ nm}$. It well agrees well with the magnification resulting from the ratio of the focal length of the objective lens and the tube lens ($104\times$) if we assume that the pixel size might have a systematic production tolerance of about 100 nm.

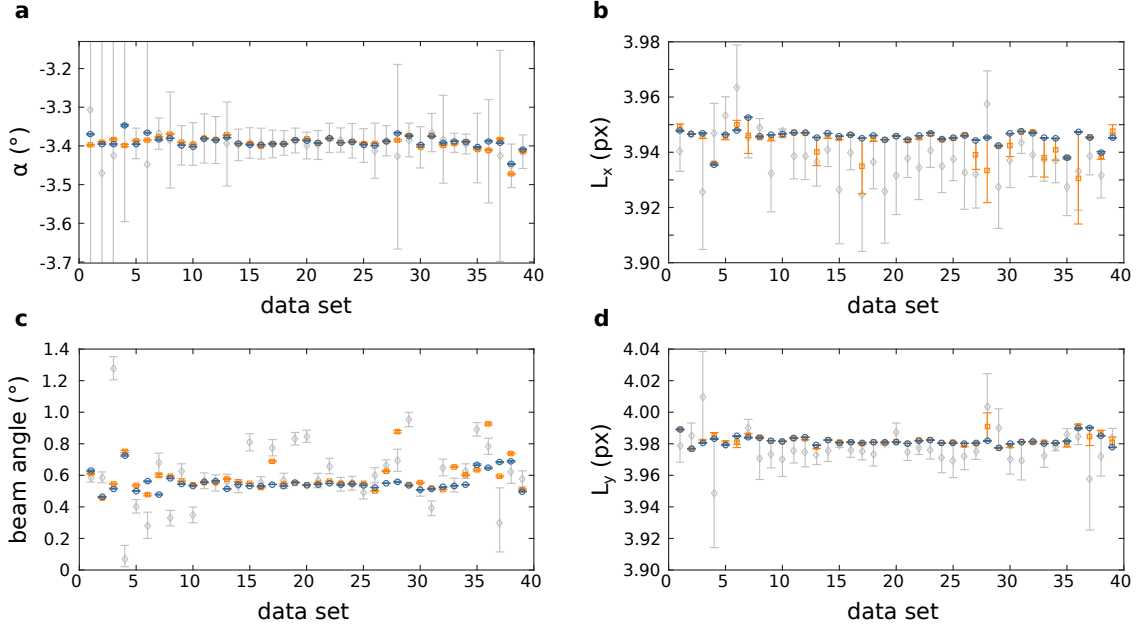


Figure 4.9.: Stability of the lattice properties: (a) Lattice tilt α , (b,d) lattice spacings $L_{x,y}$ in x- as well as y-direction, and (c) beam angle of the orthogonal beam for several successive data sets recorded over an entire day (~ 20 h). In total, 55 340 fluorescence images have been analyzed with method 1 (gray), method 2 (orange), and method 3 (blue). Due to technical reasons, the average number of images per data set is around 1800 with a standard deviation of 200 resulting in differing confidence intervals.

4.5. Detecting the Occupation of Lattice Sites

Knowing the lattice properties allows us to reconstruct the occupation of lattice sites with single atoms. Here, we first detect single atoms using the procedure explained in section 4.3.1 and subsequently optimize the position of the overlapped lattice by minimizing the quadratic distances between lattice sites and atom positions. An exemplary image with the initial detected positions and overlapped lattice sites is shown in figure 4.10(a). The mean fluorescence (in units of ADC counts) in the $3 \text{ px} \times 3 \text{ px} = 460 \text{ nm} \times 460 \text{ nm}$ vicinity of each lattice site gives rise to the histogram shown in figure 4.10(d). A lattice site is assumed to be occupied when the mean fluorescence is larger than the threshold of 1000 counts. This threshold value is slightly lower than the typical fluorescence of an isolated bright atom in a region with a small amount of background fluorescence.

We simulated pictures of atoms featuring a Gaussian PSF (amplitude of 1800 counts with 5% amplitude variation, width 1.8 px) with additional Poissonian noise as well as white background noise (mean 100 counts, standard deviation 20 counts) contributions. The parameters resemble the conditions of our imaging system except for the background atoms. The resulting accuracy of the filling detection is larger than 99% in the case of low filling of the lattice (1%). In case of simulated pictures, a histogram of the integrated fluorescence around in the region of lattice sites show a separated double peak

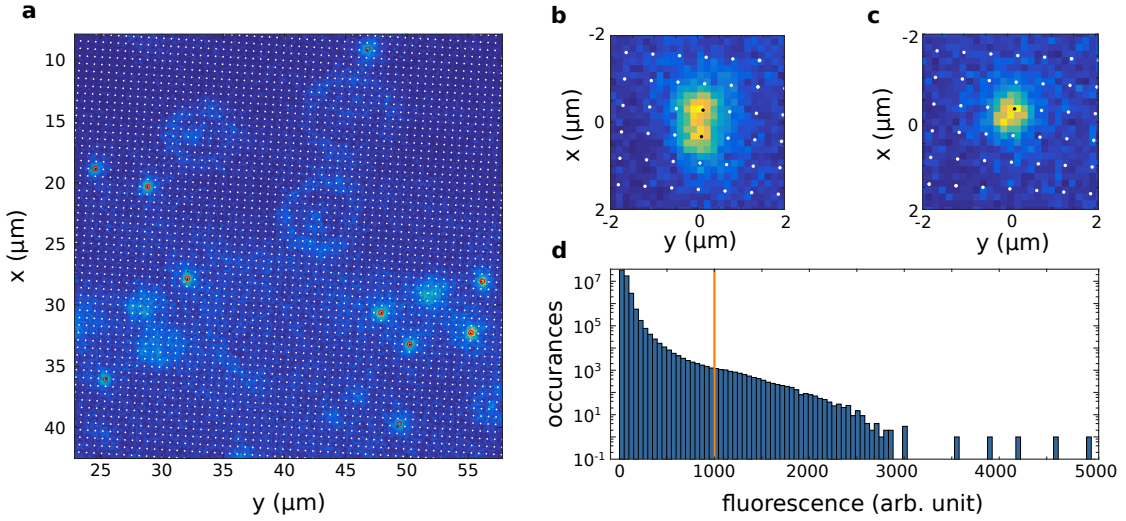


Figure 4.10.: Detection of lattice filling: (a) The red circles mark the fitted position of detected single atoms. The white dots indicate empty lattice sites whereas the black dots refer to an occupied site. The filling is determined by means of a threshold in order to select only brightest atoms. (b) Zoomed image of two nearest neighbor atoms in the optical lattice. (c) Image of the same region as in (b) at a later time where one atoms is lost from the lattice. (d) Histogram of mean photon number in the $3\text{ px} \times 3\text{ px}$ vicinity around possible lattice sites for many images with threshold condition (orange line). The missing separation between empty and occupied lattice sites arise from fluorescence contributions from out-of-focus atoms since we image atoms in a 3D lattice instead of a single plane.

structure that enables precise determination by means of a threshold, due to the absence of background atoms. Even for a dense filling of about 50% – limited by parity light-assisted collisions between pairs of atoms [143] – the accuracy of the filling detection only deteriorates slightly to 86% which mainly caused by the absence of reasonable separated atoms for detecting the initial lattice offsets. In this case the phase of the Fourier transformed image can be used to determine the lattice offsets [139] which is not important for our application where only a few atoms occupy the relevant plane. More advanced techniques like Bayesian methods [94] or likelihood estimators [127] can also be employed to improve on the detection precision in the case of dense filling or short exposure times. However, the current limitation is the distribution of atoms in a three-dimensional lattice that is expected to improve when plane selection techniques are applied.

However, the presented imaging system in its current condition enables a resolution of $r_a = 610\text{ nm}$ yielding $R = r_a/L = 0.99$ compared to state-of-the-art experiments reported in *R. Yamamoto et al.* (^{174}Yb , $R_{\text{TIT}} = 1.0$ [30]), *E. Haller et al.* (^{40}K , $R_{\text{GLG}} = 1.1$ [31]), *S. Bakr et al.* (^{87}Rb , $R_{\text{HUR}} = 0.8$ [29]), *C. Weitenberg et al.* (^{87}Rb , $R_{\text{MPQ}} = 1.1$ [19]). We believe that our design goal of $R = 0.75$ using the numerical aperture of 0.92 will be achieved in the near future and will define a new benchmark in the field of quantum

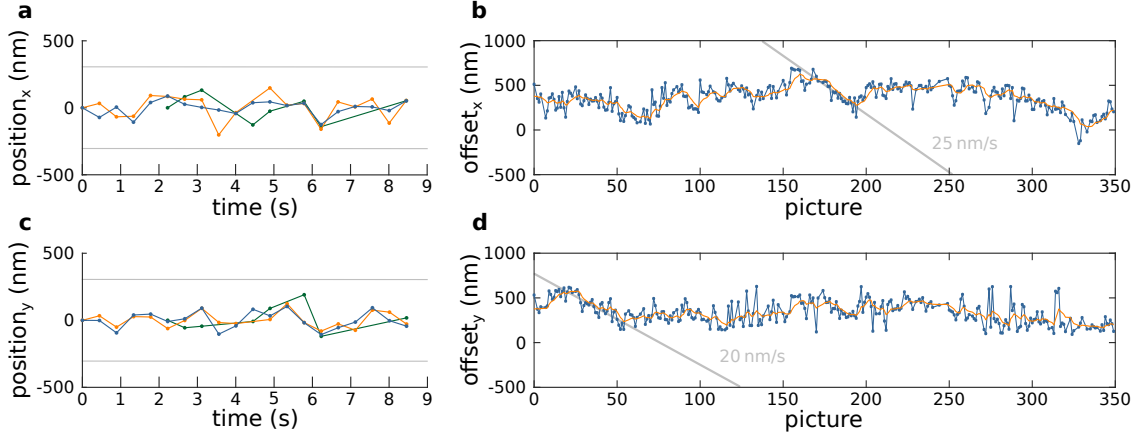


Figure 4.11.: (a,c) Short time jitter of the optical lattice determined by the fitted positions of up to three single atoms for a series of 20 successive images in both image directions. (b,d) Long term lattice offsets for subsequently recorded images. The orange line corresponds to low-pass filtered data using a Fourier filter with the cut-off frequency $1/6 \text{ picture}^{-1}$. The grey line indicates regions of highest drift velocity. The mean time in between two successive images is 0.5 s.

optics. Even now, we can clearly optically resolve adjacent atoms in the optical lattice by visual inspection, see figure 4.10(b,c). Note, by employing the deterministic transport scheme in combination with the ability to address single sites of the optical lattice, we will be able to realize arbitrary low R if the spacing between atoms and each transport step are an integer multiple of the lattice spacing.

4.5.1. Horizontal Drifts of the Optical Lattice

The optical path length of each laser beam forming an optical lattice is subjected to changes in the order of the wavelength due to e.g. thermal drifts and schlieren in air [76]. Estimating the drift behavior of a lattice is of high importance since fast drifts on the timescale of the exposure time lead to systematic blurring of the image. In figure 4.11(a,c), continuously observing the position of single atoms in 20 successive images is done by means of k-means clustering [144] where the number of clustered is known from atom detection. A standard deviation of the detected position amounts to 75 nm (65 nm) in x-direction (y-direction) which coincides with the detection precision of isolated atoms as discussed previously. After analyzing 30 of these traces we conclude that position changes are smaller than one lattice site in successive images and that no significant drift ($< 3 \text{ nm}$) of the lattice during the observation time of 8.5 s occurs.

Due to movements of the lattice of less than one lattice site during the time in between pictures, we can track the lattice movement for longer times using the lattice offsets, i.e. the coordinates of the upper left lattice site in each picture. By applying a phase unwrapping technique, the periodic lattice offsets are translated into absolute positions shown in figure 4.11(b,d). Several conclusions emerge from this figure: First, the absolute lattice offset is subjected to shot-to-shot fluctuations on the order of a quarter lattice site

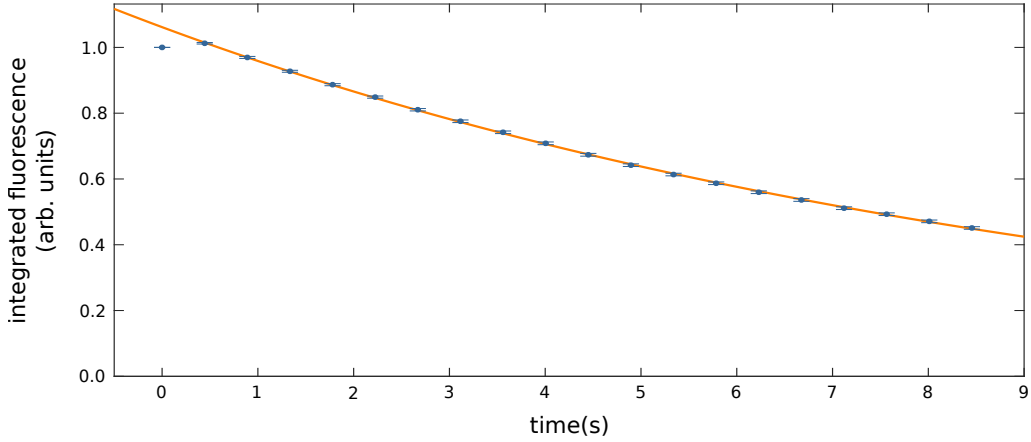


Figure 4.12.: Survival of atoms in the three-dimensional optical lattice during constant illumination calculated by integrated fluorescence over a picture after background subtraction and normalization to the first picture. The orange line is an exponential regression average of the normalized integrated fluorescence of 1700 images yielding a time constant of $9.82(3)$ s.

which arise from the precision limit of the atom detection and the varying number of detected atoms in successive images. We infer maximum drift velocities of $20(2)$ nm/s in y-direction and $25(2)$ nm/s in x-direction from a linear regression after low-pass filtering the data in Fourier space with a cut-off frequency of $1/3$ s⁻¹. These values are comparable to the 10 nm/s drift velocity in the axial direction of a one-dimensional lattice reported by *Karski et al.* [76]. However, the maximum position change during an exposure time amounts to approximately 10 nm in both experiments. Such a drift is smaller than the RMS extend of the atomic wavefunction in a deep optical lattice which is given by $x_0 = \sqrt{\hbar/(m_{\text{Cs}} \omega_{\text{vib}})} \approx 30$ nm, where \hbar is the Planck constant, m_{Cs} the mass of a cesium atom, and $\omega_{\text{vib}} \sim 2\pi \times 100$ kHz the calculated oscillation frequency in the optical lattice [145]. A more detailed discussion on oscillation frequencies for our trap geometry can be found in chapter 5. To conclude, the observed lattice drift does not limit our imaging resolution. Yet, tracking and correcting its movement over the long term is important when spatial light maps are projected onto the lattice as required for simulations, see chapter 6.

In the vertical direction, the high-numerical objective lens causes the retro-reflection of the far-detuned vertical lattice. Thus, a relative drift between the imaging system and the lattice cannot occur.

4.6. Storage Time of Atoms in a 3D Optical Lattice

To determine the storage time of neutral atoms in our optical lattice, we load atoms into the dipole trap and record a series of pictures with 300 ms exposure time while the atoms are continuously molasses cooled. At the end of a sequence, all atoms are pushed out of the trap by applying a resonant laser beam to record a picture of the background fluorescence. The integrated fluorescence of each image is corrected for the

background fluorescence and normalized to the first picture as shown in figure 4.12. The systematic lower fluorescence of the first picture has not been fully understood yet. A possible explanation might be timings issues of the mechanical shutter of the camera. Nevertheless, we are able to infer a storage time by an exponential regression to the data yielding a decay constant of $9.82(3)$ s for our predicted trap depth of $k_B \times 610 \mu\text{K}$ (160 mW per beam) created by the horizontal lattice and $k_B \times 450 \mu\text{K}$ (4 W per beam) in the vertical lattice, respectively.

We primarily attribute the relatively short lifetime to elastic collisions with background gas – in particular cesium atoms and water molecules [146] – at a pressure of 3×10^{-10} mbar in the vacuum chamber. Our finding is also compatible with the lifetime of $25(3)$ s reported in a one-dimensional far-detuned optical lattice (wavelength 1064 nm, similar trap depth) at a vacuum pressure of about 1×10^{-10} mbar [99].

However, an experimental determination of the trap frequencies, and thus, the trap depth is planned in the future using microwave spectroscopy in a magnetic gradient [27] allowing us to quantitatively compare the lifetimes which exhibit a weak dependence on the trap depth.

5. State-Dependent Transport in Two Dimensions

With the atoms trapped at the planes of a static three-dimensional optical lattice, attention is now drawn to the robustness and the state-dependent transport scheme of our implementation of a state-dependent optical lattice.

Over the last decades far-detuned optical lattices, also known as optical dipole traps, have become a standard tool in quantum optics to provide a conservative potential for atoms with an array of lattice sites [113]. Transport of neutral atoms in such a standing wave potential is realized in a deterministic and controlled way by changing the phase or frequency of one of the generating laser beams [114]. However, these transport schemes do not distinguish between different internal states of the employed atoms.

The basic idea behind the realization of state-dependent transport, often referred to as spin-dependent transport, is the correct wavelength in combination with a precise control of the lattice polarization. It has first been suggested by *Jaksch et al.* [25] and experimentally realized in one dimension for rubidium [147] and cesium [18] where the transport is realized by rotating the polarization of one of the beams using an electro-optic modulator. Recently, this scheme has been further improved in our group by implementing an arbitrary polarization synthesizer based on an acousto-optic modulator setup. The polarization synthesizer allows for fully independent transport of both spin states over arbitrary distances [75]. This is in contrast to the former implementation where only a relative movement of over one lattice site could be achieved. Note that an additional implementation of state-dependent transport is based on fixed polarizations in combination with a precise control of the quantization axis defined by a weak magnetic field in a hexagonal lattice configuration [28, 148]. However, this solution does not provide the versatility of the fully independent transport.

5.1. State-Dependent Transport Revisited

5.1.1. Optical Dipole Potentials

In a classical interpretation, an optical lattice is a conservative potential created by interfering laser beams based on the interaction of the light field with an induced dipole moment of the atoms. In a simplified semi-classical description, the potential originates from the AC-stark shift in a two-level quantum system (atom) caused by the interaction with a classical light field. In the case of a linearly polarized, far off-resonant light field, the interaction results in an attractive force directed towards intensity maxima for frequencies smaller than the atomic resonance (red-detuned) and in a repulsive force for a larger frequency (blue-detuned). The fine-structure found in alkali atoms, e.g. cesium,

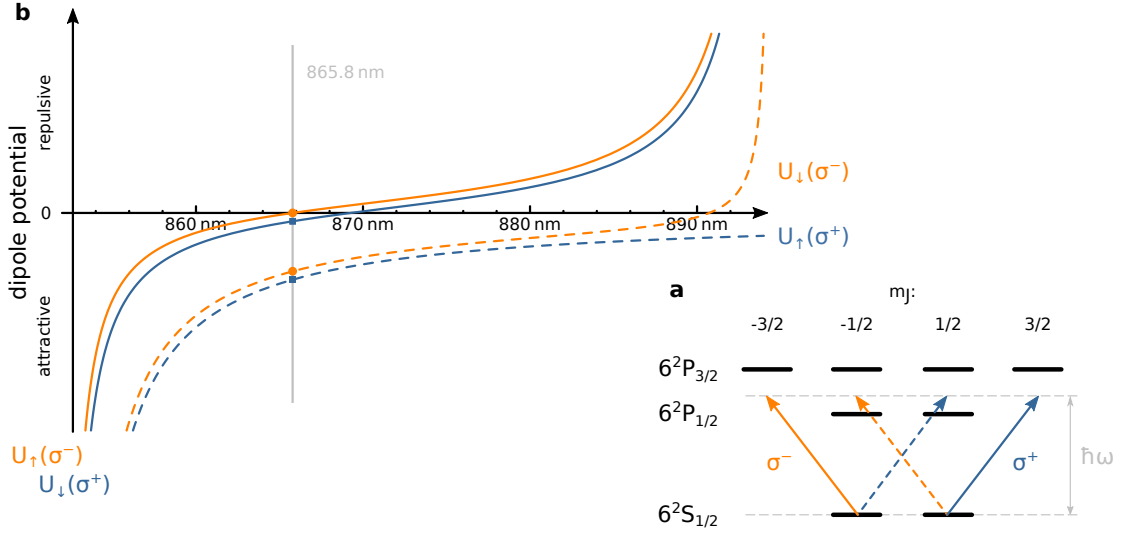


Figure 5.1.: (a) Zeeman sublevels of the fine-structure splitting in the ground and excited states of cesium. The two colors indicate possible transitions of circular polarized light at the frequency $\hbar\omega$. (b) Dipole potentials for state $|\uparrow\rangle$ and $|\downarrow\rangle$ for both circular polarization states (σ^+ , σ^-) as a function of the wavelength in the range between the D2-line at 852 nm and the the D1-line at 894 nm of cesium. The corresponding potentials for π -polarized light are fully identical for both states and are hence not shown.

allows for a state-dependent optical potential given that the lattice wavelength is set in between the two D-lines such that the repulsive and attractive contributions cancel each other for the transitions to $m_J = \pm 1/2$, see figure 5.1(a). As a result, each ground state is only affected by a single circular polarization component of the light. In the real world, the nuclear spin $I = 7/2$ of a ^{137}Cs atom causes an additional hyperfine splitting. We choose the two outermost hyperfine states $|\uparrow\rangle = |F = 4, m_F = 4\rangle$ and $|\downarrow\rangle = |F = 3, m_F = 3\rangle$ as a two-level system since they can easily be prepared by optical pumping. Their light shifts, i.e. their dipole potentials, are calculated in a similar method using second order perturbation theory of an electric dipole interaction of a multilevel atom with a classical light field. In this case, only contributions of the D1 and D2 line to the ground states need to be taken into account due to their relatively small detuning compared to other resonances. The full derivation invokes a reduction of the dipole matrix elements of the total angular momentum via the Wigner-Eckart Theorem [149], with the use of Wigner 3j as well as 6j-symbols¹ in combination with the oscillator strengths of both D-lines [98, 151, 152]. The resulting dipole potentials $U_s(q)$ of each state $s = \uparrow, \downarrow$ depend explicitly on the polarization ($q = \pi, \sigma^+, \sigma^-$) and implicitly on the wavelength of the laser light as shown in figure 5.1(b). Using a lattice wavelength of $\lambda_{\text{HDT}} = 865.8$ nm results in a vanishing potential $U_{\uparrow}(\sigma^+)$. The total dipole potentials $U_s = \sum_q U_s(q)$ for

¹Fun Fact: The 6j-symbols exhibit a symmetry of exchanging neighboring elements in the same column as well as permutations of columns, see appendix “Racah Coefficients and ‘6j’ Symbols” in reference [150].

this wavelength depend on the different polarization intensities I_{σ^+} , I_{σ^-} , I_{π} according to

$$\begin{pmatrix} U_{\uparrow} \\ U_{\downarrow} \end{pmatrix} = c_0 \cdot \begin{pmatrix} 1 & 0 & 1/2 \\ 1/8 & 7/8 & 1/2 \end{pmatrix} \cdot \begin{pmatrix} I_{\sigma^+} \\ I_{\sigma^-} \\ I_{\pi} \end{pmatrix} \quad \text{with} \quad c_0 = -k_B \times 2.717 \text{ pK}/(\text{W}/\text{m}^2), \quad (5.1)$$

where k_B denotes Boltzmann's constant. Thus, both potentials are merely sensitive to a single circular polarization component of the lattice light.

The wavelength dependence is in close analogy to the choice of a characteristic (“magic”) wavelength that fulfills certain criteria, for example state-insensitive trapping of atoms, e.g. in alkali [153, 154] or Rydberg atoms [155]. State-insensitive trapping is of special interest for extending coherences in quantum information processing or in optical metrology like optical lattice clocks where a flat zero crossing of the potentials for the used states is mandatory [85].

As we will see later, the non-vanishing component $1/8$ results in an undesirable modulation of the lattice depth during transport. Note that by selecting a trap wavelength of 869.3 nm, the potential of the states the $|\uparrow'\rangle = |F=4, m_F=3\rangle$ and $|\downarrow'\rangle = |F=3, m_F=3\rangle$ are solely generated by a single circular component of the optical lattice. In this case the two potentials are given by $U_{\uparrow'} = c'_0 \cdot (I_{\sigma^-} + I_{\pi})$ and $U_{\downarrow'} = c'_0 \cdot (I_{\sigma^+} + I_{\pi})$ with $c'_0 = -k_B \times 1.867 \text{ pK}/(\text{W}/\text{m}^2)$. As a result, the specific choice of states prohibits the use of experimentally robust optical pumping and requires more advanced techniques like STIRAP [156] to prepare single atoms in the state $|\uparrow'\rangle$. This technique causes an increase of the complexity of the experimental apparatus to achieve the same state preparation fidelities and is thus discarded for the experiment described in this thesis. However, all findings for the geometry lattice and for the transport properties, which will be presented in the following, are valid for both choices of states.

5.1.2. State-Dependent Transport in One Dimension

In one dimension, a lattice is formed by two counter-propagating laser beams at the wavelength λ_{HDT} that interfere to give rise to a standing wave pattern. The intensity can be decomposed into exactly two circular polarization components when the quantization axis is oriented along the propagation direction of the beams (x_3 -direction) as employed in figure 5.2. For both beams, the electric field oscillating with an amplitude E_0 at a frequency ω is given in $(\sigma^+, \sigma^-, \pi)$ -polarization coordinates by

$$\vec{E}_1(\vec{x}, t) = \frac{1}{\sqrt{2}} \begin{pmatrix} e^{-i\phi_1} \\ e^{-i\phi_2} \\ 0 \end{pmatrix} E_0 \mathcal{E}(\vec{x}, \vec{k}_1) e^{i\vec{k}_1 \vec{x} - i\omega t}, \quad \vec{k}_1 = 2\pi/\lambda_{\text{HDT}} \begin{pmatrix} 0 \\ 0 \\ 1 \end{pmatrix} \quad \text{and} \quad (5.2)$$

$$\vec{E}_2(\vec{x}, t) = \frac{1}{\sqrt{2}} \begin{pmatrix} 1 \\ 1 \\ 0 \end{pmatrix} E_0 \mathcal{E}(\vec{x}, \vec{k}_2) e^{i\vec{k}_2 \vec{x} - i\omega t}, \quad \vec{k}_2 = 2\pi/\lambda_{\text{HDT}} \begin{pmatrix} 0 \\ 0 \\ -1 \end{pmatrix}. \quad (5.3)$$

Here, $\mathcal{E}(\vec{x}, \vec{k})$ describes an additional spatial ($\vec{x} = (x_1, x_2, x_3)^T$) variation of the amplitude and phase to account for a Gaussian beam profile. It explicitly amounts to

$$\mathcal{E}(\vec{x}, \vec{k}) = \frac{w_0}{w(x_3)} e^{-\frac{x_1^2 + x_2^2}{(w(x_3))^2}} e^{i|\vec{k}| \frac{x_1^2 + x_2^2}{2R(x_3)} - i\Psi(x_3)}, \quad (5.4)$$

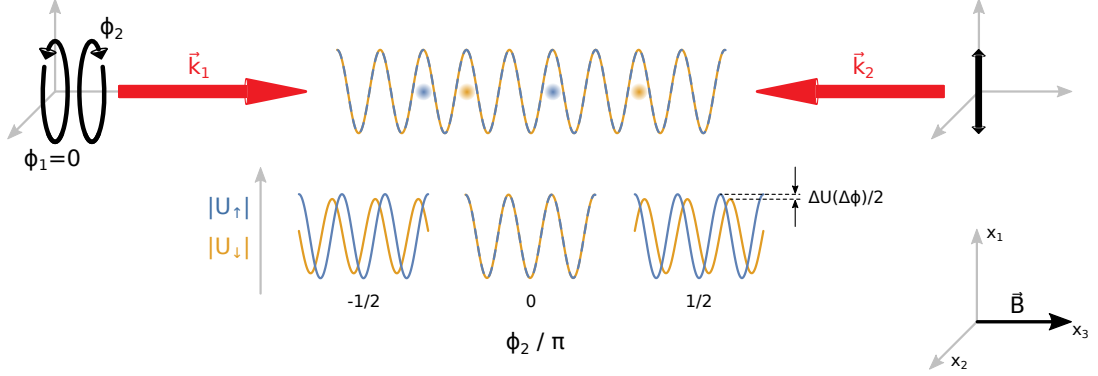


Figure 5.2.: One-dimensional transport along the quantization axis: A polarization synthesized laser beam (phases of circular polarization $\phi_{1,2}$, red arrow k_1) interferes with a counter-propagating laser beam of fixed linear polarization (red arrow, k_2). The resulting standing wave intensity is a superposition of two circular polarization components, which can be independently shifted in space by altering the phases $\phi_{1,2}$. The corresponding values of the dipole potential depth U_\uparrow (blue) and U_\downarrow (yellow) are shifted accordingly. In contrast to shifting U_\uparrow , the dipole potential depth U_\downarrow is slightly modulated by ΔU during a transport step.

where the beam waist w_0 and the Rayleigh range $x_R = \pi w_0^2 / \lambda_{\text{HDT}}$ are used to determine the beam width $w(x_3) = w_0 \sqrt{1 + (x_3/x_R)^2}$, the wavefronts's radius of curvature $R(x_3) = x_3 [1 + (x_R/x_3)^2]$, and the Gouy phase $\Psi(x_3) = \arctan(x_3/x_R)$ [107]. The imaginary part of equation 5.4 can be neglected for all practical purposes since all atoms are only trapped in the region $|\vec{x}| \ll z_R$ ($35 \mu\text{m} \ll 4.4 \text{mm}$). Due to the same argument, we further neglect the variation of the field amplitude due to the Gaussian beam profile such that $\mathcal{E}(x, y, z) = 1$, i.e. we apply a plane wave approximation.

The corresponding light intensity for the total electric field $\vec{E}(\vec{x}, t) = \sum_i \vec{E}_i(\vec{x}, t)$ yields

$$\vec{I}(\vec{x}) \equiv \begin{pmatrix} I_{\sigma^+} \\ I_{\sigma^-} \\ I_\pi \end{pmatrix} = \frac{c \varepsilon_0}{2} \vec{E}(\vec{x}, t)^\dagger \vec{E}(\vec{x}, t), \quad (5.5)$$

where the speed of light is denoted by c , ε_0 is the vacuum permittivity, and \dagger indicates the conjugate transpose. For further analysis, we choose a normalization condition for the integrated power of all beams. Thus, the real valued electric field amplitude for each beam is defined according to $I = c \varepsilon_0 / 2 \sum_1^N E_0^2 = 1$, where N denotes the total number of beams. For the configuration in equations (5.2) and (5.3), the polarization components of the intensity amount to

$$I_{\sigma^+} = \frac{1}{2} (1 + \cos(4\pi x_3 - \theta_1 - \phi_1)), \quad I_{\sigma^-} = \frac{1}{2} (1 + \cos(4\pi x_3 - \theta_2 - \phi_2)), \quad I_\pi = 0. \quad (5.6)$$

These intensities directly translate into dipole potential depths using the matrix multiplication in equation 5.1 exhibiting a maximum trap depth of $U_\uparrow = U_\downarrow = 1$ as shown in

figure 5.2. Altering the phases $\phi_{1,2}$ translates the dipole potential $U_{\uparrow,\downarrow}$ in real space by

$$\Delta x_{1,2} = \frac{\phi_{1,2}}{|\Delta \vec{k}|} = \frac{\phi_{1,2}}{|\vec{k}_1 - \vec{k}_2|} = \frac{\phi_{1,2}}{2\pi} \frac{\lambda_{\text{HDT}}}{2}. \quad (5.7)$$

A modification of the corresponding phase 2π , thereby, results in a transport of atoms in the corresponding potentials by one lattice site (periodicity $\lambda_{\text{HDT}}/2$).

A modulation $\Delta U(\Delta\phi) = |U_{\downarrow}(\Delta\phi) - U_{\downarrow}(0)|$ of the dipole potential depth $U_{\downarrow}(\Delta\phi)$ with an amplitude of $\max[\Delta U(\Delta\phi)] = 1/8 \times U_{\downarrow}(0)$ depending on the relative phase difference $\Delta\phi = \phi_1 - \phi_2$ can be observed during a state-dependent transport step of one lattice site [152]. In the following, a transport step will always refer to a state-dependent transport step since a global state-insensitive transport step does not induce changes in the potentials if the change caused by the acceleration is neglected. In contrast to U_{\uparrow} , the change in the potential U_{\downarrow} originates from the two contributions of the I_{σ^+} and I_{σ^-} intensity components, see equation. 5.1. In general, a change in the trapping potential during transport limits the maximum achievable transport speed ($20 \mu\text{s}$ per step [42]). Higher speeds result in significant heating of the atoms or even atom losses and raise the probability to excite higher vibrational energy levels, and hence, increase the decoherence [145]. Although the modulation of the trap depth states an intrinsic property of our choice of states, its impact on decoherence and transport speed can be overcome by means of optimal control [157].

5.2. State-Dependent Transport in Two Dimensions

Extending the concept of transport into two dimensions is more demanding since the quantization axis cannot be overlapped with both directions simultaneously. In the following, I present my new concept for two-dimensional state-dependent transport in an optical lattice in more detail and analyze its stability against experimental imperfections as compared to reference [15].

Starting from the one-dimensional setup, we rotate the orientation of the formerly counter-propagating beam \vec{k}_2 by 90° such that it is placed in the orthogonal direction within the horizontal plane. As a result, the periodicity, i.e. lattice spacing, is increased by $\sqrt{2}$. Adding another polarization synthesized beam that is counter-propagating to the first beam \vec{k}_1 causes additional interference along the second direction. This way, the synthesized beams are oriented along the quantization axis - enabling direct control of the circular intensity components - while the fixed polarization of the other beam is oriented perpendicular to the axis.

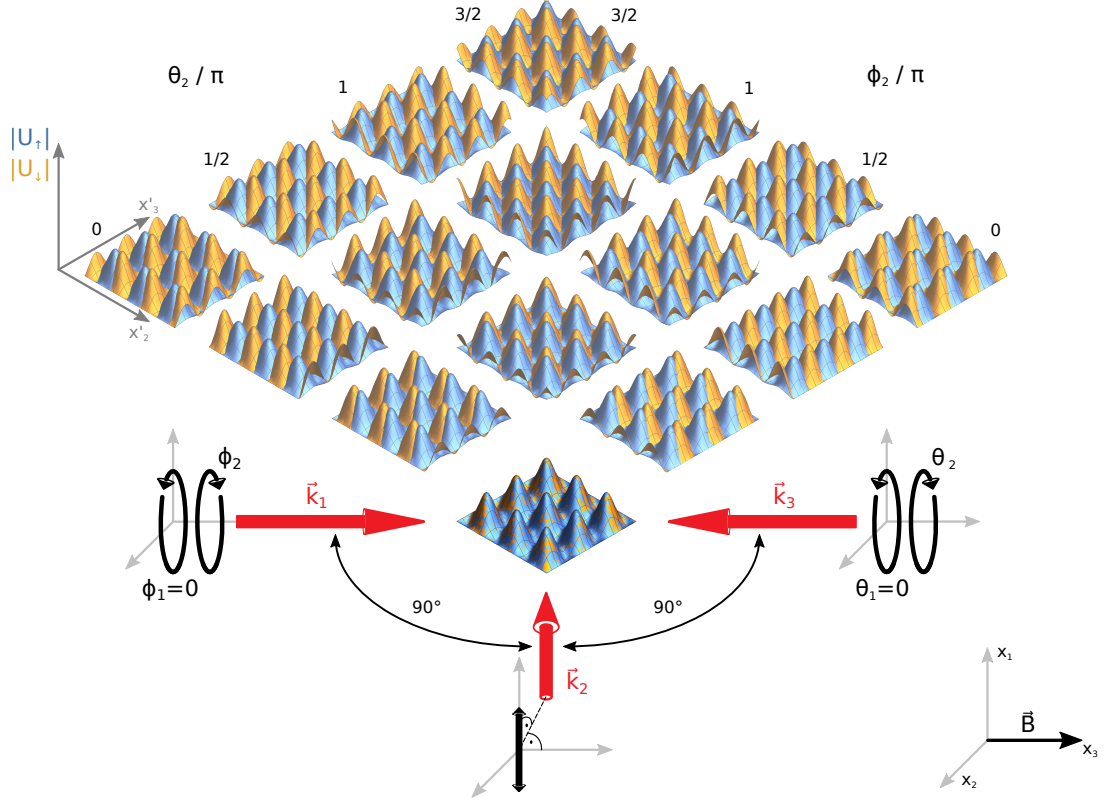


Figure 5.3.: Two-dimensional transport scheme: Three interfering laser beams (red arrows) create dipole potential depths for $|\uparrow\rangle$ (blue), $|\downarrow\rangle$ (yellow) where atoms are trapped at the peaks. A weak magnetic field \vec{B} defines the quantization axis for the atoms. Linear polarization is indicated by a black arrow whereas black circles visualize a phase for a circular polarization component of a laser beam forming the lattice.

Mathematically, the setup is described by

$$\begin{aligned}
 \vec{E}_1(\vec{x}, t) &= \frac{1}{\sqrt{2}} \begin{pmatrix} e^{-i\phi_1} \\ e^{-i\phi_2} \\ 0 \end{pmatrix} E_0 \mathcal{E}(\vec{x}) e^{i\vec{k}_1\vec{x} - i\omega t}, & \vec{k}_1 &= 2\pi/\lambda_{\text{HDT}} \begin{pmatrix} 0 \\ 0 \\ 1 \end{pmatrix}, \\
 \vec{E}_2(\vec{x}, t) &= \frac{1}{\sqrt{2}} \begin{pmatrix} 1 \\ 1 \\ 0 \end{pmatrix} E_0 \mathcal{E}(\vec{x}) e^{i\vec{k}_2\vec{x} - i\omega t}, & \vec{k}_2 &= 2\pi/\lambda_{\text{HDT}} \begin{pmatrix} 0 \\ -1 \\ 0 \end{pmatrix}, \\
 \vec{E}_3(\vec{x}, t) &= \frac{1}{\sqrt{2}} \begin{pmatrix} e^{-i\theta_1} \\ e^{-i\theta_2} \\ 0 \end{pmatrix} E_0 \mathcal{E}(\vec{x}) e^{i\vec{k}_3\vec{x} - i\omega t}, & \vec{k}_3 &= 2\pi/\lambda_{\text{HDT}} \begin{pmatrix} 0 \\ 0 \\ -1 \end{pmatrix},
 \end{aligned} \tag{5.8}$$

where the intensity and phase profiles of the astigmatic lattice beams can be neglected due to the relatively small region of interest. The total electric field translates into an

intensity distribution with two circular components

$$\vec{I}(\vec{x}) = \frac{1}{3} \begin{pmatrix} 3/2 + \cos(2\pi(x_2 + x_3) - \theta_1) + \cos(2\pi(x_2 - x_3) + \phi_1) + \cos(4\pi x_3 - \theta_1 - \phi_1) \\ 3/2 + \cos(2\pi(x_2 + x_3) - \theta_2) + \cos(2\pi(x_2 - x_3) + \phi_2) + \cos(4\pi x_3 - \theta_2 - \phi_2) \\ 0 \end{pmatrix}. \quad (5.9)$$

The resulting potential depths using equation 5.1 as well as the setup of the lattice beams are shown in figure 5.3. Several conclusions arise from this figure. First, the periodicity of the lattice, i.e. the lattice vectors, are oriented in a frame (x'_2, x'_3) that is rotated by -45° relative to the original setting around the normal vector pointing along the x_1 -axis. Second, altering the phase $\phi_{1,2}$ ($\theta_{1,2}$) translates the blue (yellow) sub-lattice along the diagonal x'_2 (x'_3) relative to the original frame according to

$$x_0 \rightarrow x_0, \quad x_2 \rightarrow x_2 + \frac{\theta_{1,2} - \phi_{1,2}}{2\pi} \times \frac{\lambda_{\text{HDT}}}{2}, \quad x_3 \rightarrow x_3 + \frac{\theta_{1,2} + \phi_{1,2}}{2\pi} \frac{\lambda_{\text{HDT}}}{2}. \quad (5.10)$$

The dipole potentials are shifted by an integer number of lattice sites if the relative phase differences $\Delta\phi = \phi_1 - \phi_2$ ($\Delta\theta = \theta_1 - \theta_2$) are changed by multiples of 2π .

The total translation can be understood in terms of the transport for each beam pair $(\vec{E}_i, \vec{E}_j) \forall i, j \in \{1, 2, 3\} : i \neq j$, and thus, by a combination of one-dimensional transport operations. Likewise, the shape of the potential depth is determined by the three individual terms of equation 5.9 due to the direction and spacing of the periodic modulation. They are caused by the pairwise interference along the direction of each $\Delta\vec{k}_{ij} = \vec{k}_i - \vec{k}_j \forall i, j \in \{1, 2, 3\}$, while its amplitude corresponds to the periodicity of the interference in this direction.

5.2.1. Potential Depth and Trap Frequencies

The maximum potential depth (according to equation 5.9) yields $U_{\text{max}} = 1.5 \times U_0$ and hence a 50% larger depth than in the one-dimensional system if the total power of all laser beams in each system is identical. In one dimension, the inter-site potential barrier U_{ISB} differs from this maximum potential depth only during transport steps. In the 2D configuration, the corresponding barrier amounts to a lower value of $U_{\text{ISB}} = 1.333 \times U_0$ even in the case of vanishing relative phases, i.e. overlapping potentials, see figure 5.4(a). There, the black arrows indicate the important transport directions for a split step quantum walk where a pure change in $\Delta\phi$ or $\Delta\theta$ is performed and grey lines mark the unit cell of the square lattice. The center of the potential can be described in a harmonic potential approximation with a minor and a major axis of the ellipse yielding trap frequencies. The corresponding trap frequencies for our cesium atoms (mass m_{Cs}) amount to $\omega_{\text{Minor}} = \omega_{\text{1D}} = \sqrt{(4\pi U_0)/(\lambda_{\text{HDT}} m_{\text{Cs}})}$ along the first principal axis (the direction of x_2), and $\omega_{\text{Major}} = \omega_{\text{minor}}/\sqrt{3}$ along x_3 , respectively.

Modulation During Transport The potential depth and hence the trap frequencies are constant for the state $|\uparrow\rangle$ during a state-dependent transport step. However, they vary for the state $|\downarrow\rangle$ due to relative shift of the σ^+ contribution as shown in figure 5.4(b) for

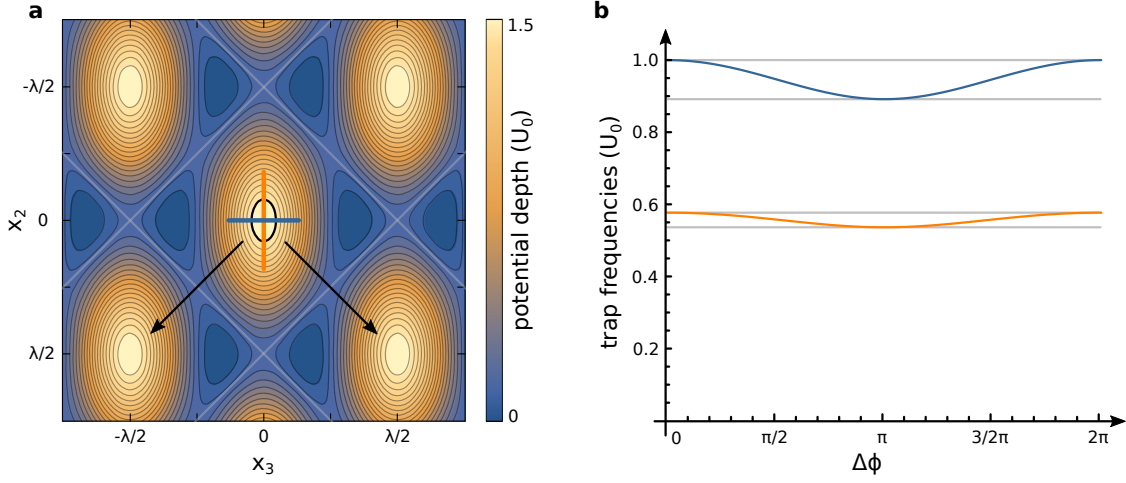


Figure 5.4.: (a) Zoomed picture of the rectangular lattice potential depth for $|\downarrow\rangle$ state when all polarization phases are zero. The black arrows indicate directions of transport, while a unit cell of the lattice potential is highlighted by the grey diagonal lines. The scale of the image ranges from 0 (dark blue) to a maximum normalized potential depth of $1.5 \times U_0$ (light yellow). The main (orange) and minor (blue) axis at the maximum of the potential depth determine the trap frequencies for $|\downarrow\rangle$, which are plotted in (b) as a function of the angle difference $\Delta\phi$, during a transport following the right arrow. The plotted trap frequencies are initially identical to those of $|\uparrow\rangle$, which are indicated by the two grey lines and do not change during transport.

the trap frequencies. The amplitude of the modulation of the potential depth amount to $|\Delta U| = 1/8 \times U_0$ which coincides with the one dimensional case. Besides the corresponding change in the depth of the potential, the ellipse of the trapping potential is slightly tilted during a transport step by a few degrees. In addition, a small displacement of the ellipse center position in the order of a few tens of nanometer can be observed for U_\downarrow when the potential U_\uparrow is translated. The displacement becomes maximum when the relative phase between two potentials equals to π but is still much smaller than the periodicity of the lattice.

5.2.2. Distortions of the Optical Lattice

So far, we have assumed that the lattice beams and the quantization axis are perfectly aligned and the intensities of all beams are identical. In a physical system, such conditions can only be realized within a certain precision. Hence, the robustness of the proposed configuration against such detrimental conditions is studied in the following section. Without loss of generality all circular phases $\phi_{1,2}$ and $\theta_{1,2}$ are set to zero for this analysis.

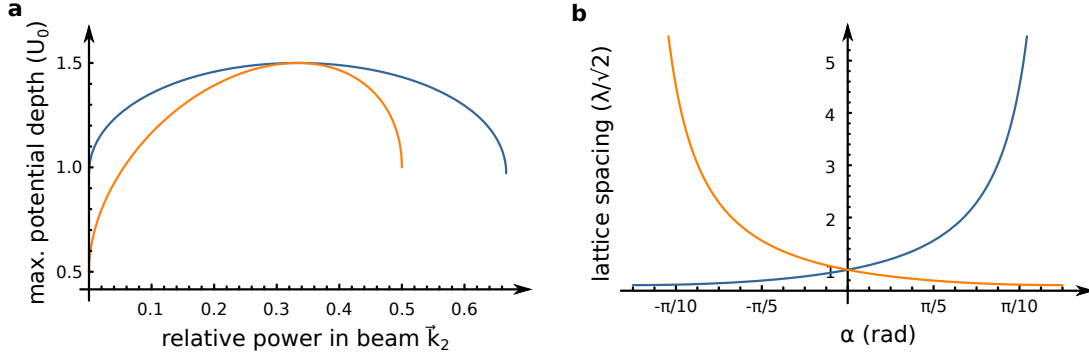


Figure 5.5.: (a) Maximum potential depth as a function of the power in beam \vec{k}_2 for the case of constant total power. The orange line corresponds to the case where the remaining power is distributed symmetrically to the two other beams \vec{k}_1 and \vec{k}_3 . The blue line resembles the case where beam \vec{k}_3 possesses 1/3 of the total power. (b) Variation of the lattice spacing in the two directions depending on the tilt of beam \vec{k}_2 .

Power Imbalance

It is well known that intensity and phase fluctuations of the lattice beams directly lead to heating and decoherence of the atoms [36, 37]. These fluctuations may arise from instabilities of the Ti:Sapphire laser system or by stimulated Brillouin scattering, i.e. the interaction of light with induced photons via electrostriction, in long optical fibers at high light intensities [158]. The influence of the phase instabilities of the laser system can be reduced by carefully matching the optical path length of all lattice beams. The impact of intensity noise on the potential depth is reduced in our system by feedback loops for each beam. However, systematic differences in the power of each beam might still occur leading to a linear change in potential depth for a global reduction or increase of the light intensity. While modification of the total beam power directly translates into a linear change of the potential depth, differential power differences in between lattice beams only lead to a change in the potential depth in second order, see figure 5.5(a). We distinguish two cases for power imbalances while the total power is kept constant: In the first case, the power of beam \vec{k}_3 is fixed and the power in beam \vec{k}_2 is varied yielding an asymmetric power distribution of the counter-propagating beam. In the other case, the power in beam \vec{k}_2 is varied while the remaining power is distributed symmetrically to the beams $\vec{k}_{1,3}$. Both cases maximize the potential depth when the total power is equally distributed over the three beams. Deviating from this conditions leads to a favorable smaller reduction of the potential depth. As an example, a 10% power modulation results in a change of the potential depth by 0.2% (blue case) and 0.5% (orange case) and thus lead to a modification of the trap frequencies which is smaller than 0.1% and 0.25%, respectively.

Misalignment of the Lattice Beams

The presented ideal three-beam configuration for the two-dimensional state-dependent transport leads to a square lattice with a lattice spacing $L = \lambda_{\text{HDT}}/\sqrt{2}$ and a tilt angle

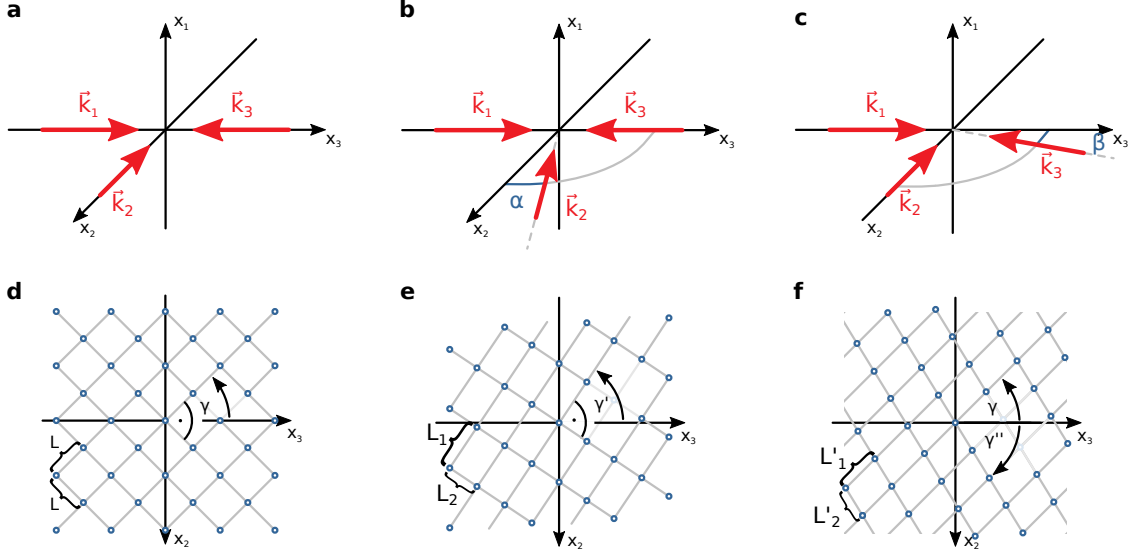


Figure 5.6.: Setup for the undistorted two-dimensional transport scheme (a) and for different cases of misalignment (b-c) resulting in a square lattice (d) and rectangular (e) as well as oblique (f) lattice configuration.

$\gamma = \pi/2$ rad, see figure 5.6(a,d).

By analyzing fluorescence images of single atoms, we have observed a clear lift of the degeneracy of lattice spacing in perpendicular directions of our optical lattice experiment, see section 4.4. This behavior can be reproduced by introducing a small tilt γ' of the beam with fixed polarization (\vec{k}_2) which causes a global rotation of the lattice structure and the emerging of two distinct lattice spacings $L_{1,2}$ according to

$$L_{1,2} = \sqrt{\frac{1}{2 \mp 2 \sin(\alpha)}} \approx \frac{1}{\sqrt{2}} \left(1 \pm \frac{\alpha}{2}\right), \quad \gamma' = \frac{\pi}{4} + \frac{\alpha}{2}. \quad (5.11)$$

Following the classification of Bravais for lattices in two dimensions [159], this configuration realizes a rotated rectangular lattice, see figure 5.6(b,e). The dependence of the lattice spacing on the tilt angle (shown in figure 5.5(b)) can be used to calculate the tilt angle of the lattice and to distinguish it from a pure rotation of the imaging camera.

Other properties like the potential depth and the trap frequencies remain constant or are not subjected to changes in first order approximation, respectively. The state-dependent transport is also not affected by this kind of misalignment since the π -polarization component of the tilted beam is still vanishing. Similarly, a rotation of \vec{k}_2 around the axis x_3 out of the original plane does not alter the polarization of the beam nor does it introduce a deviation from a square lattice of the undistorted configuration. However, one should guarantee that such an angle is relatively small since it can cause an undesirable beating with the vertical, far-detuned standing wave. The experimental alignment of \vec{k}_2 is rather difficult due to the absence of a reference unlike the alignment of the two beams \vec{k}_1 and \vec{k}_3 which are counter-propagating and can thus be aligned by coupling one beam into the optical fiber of the other output.

Despite the precise method of aligning the counter-propagating beams, we consider a non-vanishing angle β between \vec{k}_3 and the x_3 -axis, as shown in figure 5.6(c,f). This way, we create a homogeneous running wave contribution I_π in the center of the trap that does not induce an additional modulation of the potential but reduces the inter-side barrier due to the loss in beam power/intensity for the circular components. Additionally, the lattice structure is converted to an oblique type where one lattice direction is sheared relative to the other which alters the two lattice spacings to $L'_{1,2}$. In first order approximation, the new angles for the two lattice directions are given by

$$\gamma = \frac{\pi}{4} \text{ rad}, \quad \gamma'' \approx \frac{\pi}{4} \text{ rad} + \frac{\beta}{2} y. \quad (5.12)$$

For small angles β , the amount of power in the circular components of the misaligned beam is negligible resulting in the ability to transport atoms in a state-dependent manner. In our system this type of distortion is strongly suppressed since the angles of the two lattice directions are compatible with 90° within one standard deviation as mentioned earlier in section 4.4.

Note, that the other two remaining Bravais lattices types in two dimensions (hexagonal and centered rectangular) can also be realized in a three beam interference. As an example, the interference pattern of three beams positioned every 120° creates a hexagonal structure [28, 160].

Misalignment of the Quantization Axis

An angle between the quantization axis and the desired direction along the axis x_3 directly modifies the distribution of polarization components of the beam intensity in the coordinate system of the atoms. An arbitrary rotation of the quantization in the horizontal plane around the x_1 axis leads to a reduction of the magnitude of both circular polarization components I_{σ^+,σ^-} in favor of the linear polarization component I_π . A linear component results in an additional modulation of the dipole potential which enhances the existing modulation during transport steps leading to a further reduction of the acceptable transport speed.

In the experiment, a pair of compensation coils is mechanically aligned to the beam axis and create a weak magnetic field that defines the quantization axis. Due to the magnetic shield, static and varying external fields are highly suppressed that might otherwise cause pointing instabilities in the direction of the guiding field. In the future, microwave spectra of atoms [27] can be used to identify and to correct for a residual angle such that remaining contributions are negligible.

Reflections

Any optical component in the path of the lattice beam reflects some part of the laser light which may interfere with the original setting. Examples are the telescope lenses which exhibit a planar surface as well as the glass cell which is closest to the atoms and cannot be tilted easily.

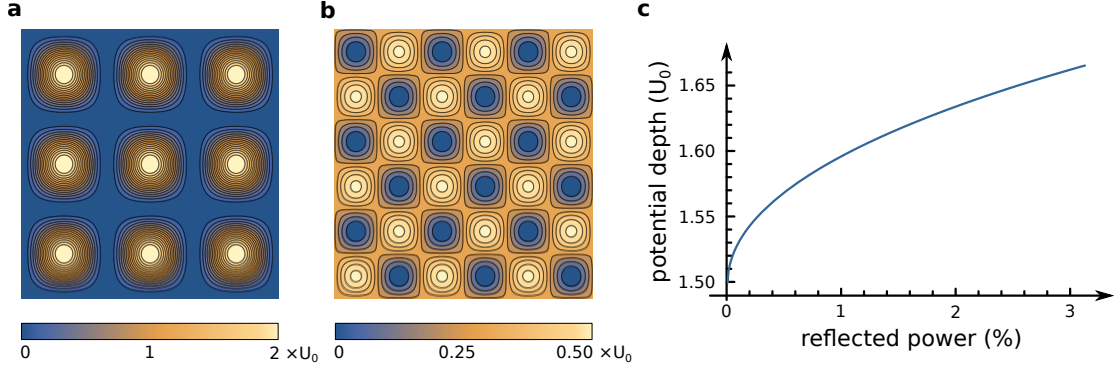


Figure 5.7.: (a,b) Potential depth in a crossed configuration of four interfering laser beams for two values of the global phase of the two counter-propagating beam pairs. The global phase determines the maximum potential depth $2 \times U_0$ (a) and $U_0/2$ (b) and the lattice spacing of $\lambda_{\text{HDT}}/\sqrt{2}$ (a) or $\lambda_{\text{HDT}}/2$ (b). The frame is rotated by $\pi/4$ rad for convenience. (c) Increase of the potential depth for reflected powers of laser beam \vec{k}_2 .

Let us first consider the case where a reflection of the beam \vec{k}_2 is propagating towards the center of the trap and exhibits the same amplitude as all other beams, i.e. by assuming

$$\vec{E}_4(\vec{x}, t) = \frac{1}{\sqrt{2}} \begin{pmatrix} 1 \\ 1 \\ 0 \end{pmatrix} E_0 \mathcal{E}(\vec{x}) e^{i\vec{k}_2 \vec{x} - i\omega t - i\delta}, \quad \vec{k}_4 = 2\pi/\lambda_{\text{HDT}} \begin{pmatrix} 0 \\ 1 \\ 0 \end{pmatrix}. \quad (5.13)$$

Depending on the global phase δ of this beam, any standing wave pattern in between the two limiting cases shown in figure 5.7(a,b) may occur. Note, that the two patterns are plotted in a rotated frame (by $\pi/4$ rad) such that the creating beams are aligned along the diagonals. The first lattice pattern exhibits the same spacing $L_a = \lambda_{\text{HDT}}/\sqrt{2}$ and an angle of the lattice vectors at $\pi/4$ rad relative to the directions of the laser beams which is identical to the three beam interference. In contrast, the maximum potential depth amounts $U_a = 2 \times U_0$. It is a common feature of all configurations presented in this thesis, that the interference of N laser beams of the same intensity I_0 obeys a maximum intensity of $N/2 \times I_0$, and thus, trap depth of $N/2 \times U_0$. The second pattern can be seen as a generalized version of the counter-propagating, one-dimensional setup. In this case, the lattice spacing is given by $L_b = \lambda_{\text{HDT}}/2$ and lattice directions are oriented along the propagation axis of the four beams corresponding to the diagonals in the figure. The maximum trap depth amounts at a low value of $0.5 \times U_0$. A feature that depends on the potentially drifting phase δ is highly undesirable since the phase of the retro-reflected beam is not controlled experimentally and may lead to a change of lattice geometry during an experimental sequence.

Independently of δ , this four-beam setup degrades the two-dimensional state-dependent transport to only one dimension along the direction of the polarization-synthesized beams $\vec{k}_{1,3}$. The positions of the maxima translate according to $p_{1,2} = [5 + 3 \cos(\theta_{1,2} - \phi_{1,2})] \times \lambda_{\text{HDT}}/4$ for states $|\uparrow\rangle, |\downarrow\rangle$ albeit the potential depth is strongly modulated due to the two possible lattice patterns as discussed before. Evidently, this configuration is unsuitable

for performing state-dependent transport experiments in two-dimensions. However, the degradation of two-dimensional transport only appears when the four beam interference is dominant over the three beam interference. One might ask the question what beam power of the reflected beam is acceptable to allow for an undistorted two-dimensional transport. We already know that the three beam interference pattern is rather insensitive towards imbalances of the power of the each beam. The same phenomenon also occurs in the case of a four beam interference. Consequently, a small reflection can result in a non-linear increase in the trap depth as exemplary shown in figure 5.7(c) if the phases δ of the back reflected light is chosen identical to figure 5.7(a). In the other limiting case a reduction of the trapping potential depth may occur. Thus, a typical reflectivity of optical coatings amounts of less than 0.5% leads to a change of up to 7% in the potential depth. In practise, all beams forming the optical lattice are divergent at the position of the glass cell yielding significantly less reflected intensities at the position of the atoms. All other optical components (lenses, waveplates, etc.) are placed at a larger distance where a tiny tilt is sufficient to guide the reflected beam out of the trapping region.

We conclude that reflections in the three beam interference need to be prevented by optical coating on all surfaces and by small tilt of optical components relative to the transmitted beam. Otherwise, the potential depth is subjected to a large modification whereby the sign of the change is determined by the global phase of the retro-reflected beam.

5.2.3. Alternative Scheme: Perpendicularly-Oriented Quantization Axis

In general, it can be proven that a 2D state-dependent transport can be achieved if the quantization axis is located within the horizontal plane spanned by all lattice beams and all polarizations can be modulated [161]. However, state-dependent transport in two dimensions can also be realized – albeit subjected to a slightly stronger modulation of the U_{\downarrow} lattice during transport – if the quantization axis is aligned perpendicular to the lattice plane [95]. In this case, we require the control over the polarization angle and the intensity of all lattice beams forming the lattice. This scheme has been proposed by A. Alberti and is based on two independent, one-dimensional lattices, each of which is created by two perpendicular beams. Both lattices share a common direction for one of their generating beams similar to the presented three-beam configuration for two-dimensional transport. The interference between both lattices is effectively canceled out due to a set frequency mismatch of 1 MHz caused by driving two pairs of AOMs for each lattice at slightly different RF frequencies.

The advantage of this setup results from the fact that the plane selection, as well as an early proposal for simulating artificial magnetic fields in quantum walks, require a orthogonal orientation of the quantization axis relative to the lattice plane. On the contrary, this scheme requires experimental control over no less than four independent polarization-synthesized lattice beams, and hence, eight individual intensity and phase control loops. Besides the tremendous increase in complexity and the consumption of space on an optical table, the scheme dramatically limits the achievable potential depth: One reason arises from the two independent, and thus, non-interfering, one-dimensional lattices of half the laser power to allow for transport in the directions. Furthermore,

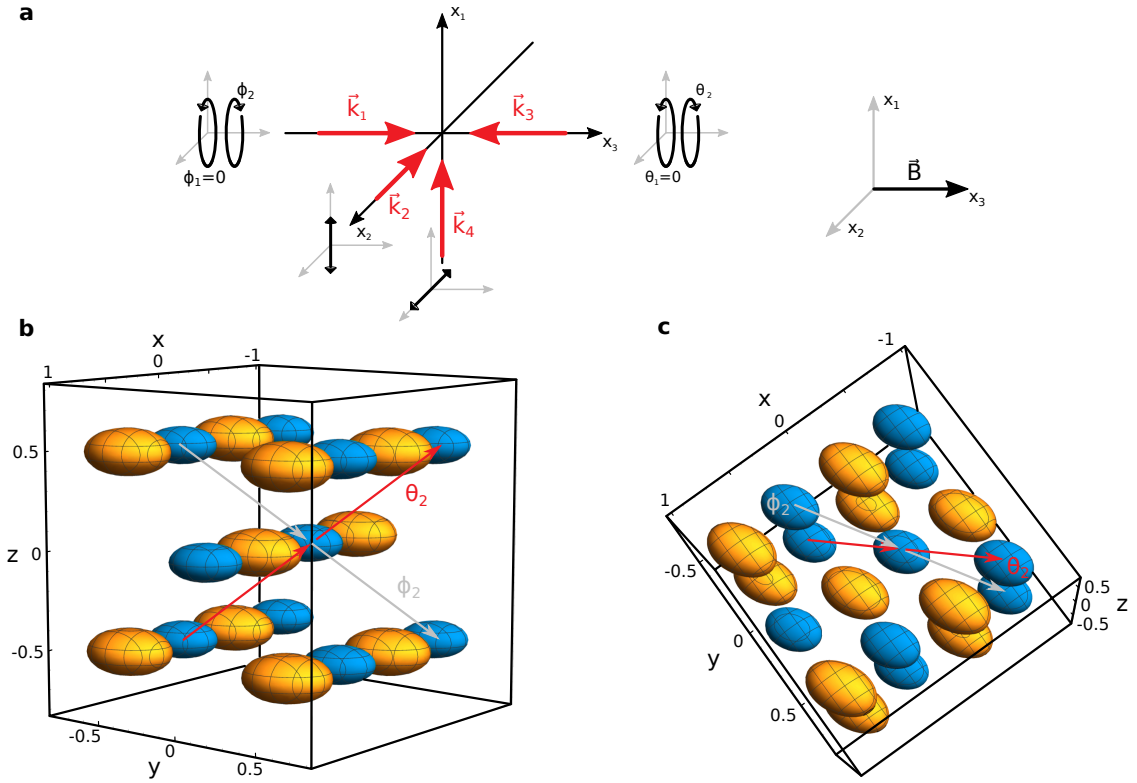


Figure 5.8.: (a) Setup of four interfering laser beams for three-dimensional state-dependent lattice. (b,c) The corresponding potentials U_\uparrow (blue) and U_\downarrow (yellow) are indicated by contour surfaces at 75% of the potential depth for different view angles. Spatial units are given in λ_{HDT} . The arrows indicate exemplary transport step in the U_\downarrow potential for a change of $\phi_2 = 0 \rightarrow 2\pi$ and $\theta_2 = 0 \rightarrow 2\pi$, respectively.

two polarization synthesized beams of almost identical frequency ($\Delta f \approx 1$ MHz) need to be overlapped, e.g. by a non-polarizing beam splitter causing a power loss of 50% for both beams. As a result, this scheme demands for a four times higher laser power compared to the previous solution in order to achieve the same potential barrier between neighboring lattice. We refrain from implementing this scheme since such a high power is only available by employing an additional Ti:Sapphire laser system and due to the large number of required control loops.

5.3. State-Dependent Transport in Three Dimensions

In this section, we address the question whether it is possible to further extend the two-dimensional transport scheme to three dimensions. A small relative displacement of the lattices for the two states would enable to cool atoms into the vibrational groundstate along all lattice directions using solely the robust method of microwave sideband cooling, see section 6.3. We assume that the two-dimensional setup in equation 5.8 is enlarged

by an additional laser beam that is oriented along the vertical direction (x_1) and linearly polarized along x_2 :

$$\vec{E}_4(\vec{x}, t) = \frac{1}{\sqrt{2}} \begin{pmatrix} 1 \\ 1 \\ 0 \end{pmatrix} E_0 \mathcal{E}(\vec{x}) e^{i\vec{k}_4\vec{x} - i\omega t}, \quad \vec{k}_4 = 2\pi/\lambda_{\text{HDT}} \begin{pmatrix} -1 \\ 0 \\ 0 \end{pmatrix}. \quad (5.14)$$

$$(5.15)$$

The corresponding setup is shown in figure 5.8(a) leading to the potential landscapes shown in figure 5.8(b-c) for different view angles. Following the classification by Bravais [159], the lattice obeys a body-centered cubic structure where potential maxima for the state $|\uparrow\rangle$ are located at basis vectors $b_1 = (0, 0, 0)^T$ and the maxima for state $|\downarrow\rangle$ at $b_1 = \lambda_{\text{HDT}} \times (1/2, 0, 0)^T$ if all polarization phases are equal to zero.

Why it could work. As indicated in the same figure by red (change in ϕ) and gray (change in θ) arrows, the dipole potential U_\downarrow is translated along the diagonal directions. Even though it is not shown in the picture, the same holds true for the other potential U_\uparrow . The transport directions can be understood from the one-dimensional transport where the components of the direction are given by the transport along each separate beam pair. Exchanging a fixed linear polarization by a polarization synthesis to increase the number of transport directions bears the drawback of creating a contribution of π -polarized light, and is thus not considered here. In principle, two transport directions are also sufficient for the main purpose of cooling as long as there is a non-vanishing relative shift between the two potentials along the vertical direction of the far-detuned optical lattice.

Why it does not. The intensity distribution of the two circular polarization components are identical in shape but translated in space such that the maxima never coincide for any combination of polarization angles $\phi_{1,2}, \theta_{1,2}$. As a immediate consequence, the diameter of the contour surface of the potential U_\downarrow is significantly larger than U_\uparrow due to the mixture of circular intensities for the potential U_\downarrow , see equation 5.1. More importantly, the maxima of the potentials are always separated and cannot be displaced from one another by about 20 nm as required for microwave sideband cooling [162].

Varying the amplitude of \vec{E}_4 while starting from a vanishing amplitude results in a smooth transition from a purely horizontal lattice to the three-dimensional lattice potential. This could potentially be used to create a small differential drag, and thus displacement of the lattice potentials, if the state-dependent lattice was superimposed with the strong periodic potential of the far-detuned lattice.

Alternative Configuration One might also employ the ideas for transport for a configuration where the quantization axis is perpendicular to the propagation direction of laser beams as presented in section 5.2.3. The two-dimensional transport in the horizontal plane is realized by the three-beam configuration explained in section 5.2, where the quantization axis is located inside the lattice plane along the direction of the counter-propagating beams. In addition, two synthesized laser beams forming a vertical supplementary standing wave allow for transport in this direction if their frequencies are

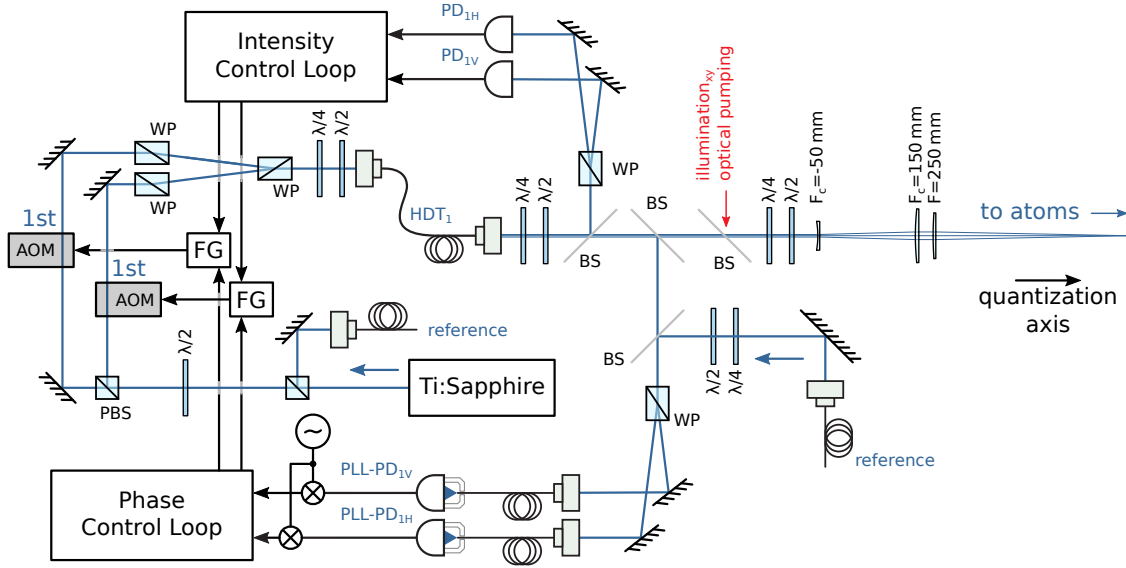


Figure 5.9.: Implementation of the setup for the polarization-synthesis of one lattice beam.

detuned to the horizontal lattice and their phase as well as intensities can be precisely controlled. However, the phase of any vertical standing wave always needs to be stabilized to the first surface of the objective in order to guarantee that atoms are kept in focus for high resolution imaging and addressing. Implementing such a control loop in an experiment constitutes a tremendous technical challenge.

5.4. Technical Implementation of the Polarization Synthesis

As a reminder, the presented transport scheme for two dimensions relies on the polarization synthesis of two counter-propagating laser beams and an additional orthogonal beam of fixed polarization. The required experimental setup is, in principle, identical to the one presented in figure 4.3 except for the polarization synthesis which is discussed in this section.

The polarization synthesis is based on the ability to deterministically control the relative phase of the two orthogonal circular polarization components of a light beam. An early implementation of polarization synthesis of a light beam is reported in reference [163]. It has first been employed in a one-dimensional lattice experiment to transport atoms state-(in)dependently and to allow for the preparation of arbitrary patterns of atoms [27, 75]. Here, we adapt this technique for the two counter-propagating beams in the two-dimensional transport scheme using three interfering laser beams.

For simplicity, I will focus solely on the polarization synthesis of one lattice beam since the setups for both beams are identical. The system is constructed as follows (see figure 5.9): The light of a Ti:Sapphire laser is split into three beams where one beam exhibiting low power is used as a reference beam for phase locking and the other two are modulated in

intensity and phase by 80 MHz AOMs in first order configuration. The laser beams passing the AOMs are of orthogonal linear polarization and can therefore be overlapped by a Wollaston prism (WP). To compensate of the slight ellipticity in the beam profile caused by the WP and to improve the degree of polarization in each beam, both beams pass through an additional WP before being overlapped at the prism. A precise static transverse overlap is assured by an optical, polarization-maintaining fiber which is required for a homogeneous polarization synthesis over the entire laser beam profile [27]. However, care must be taken to guarantee a precise compensation of polarization disturbing effects due to the optical fiber and the fiber coupler that tend to induce a small retardance in the polarization. Both effects are compensated by waveplates in front and after the fiber. Custom made beam splitters (BS, 6 % reflectivity for s- and p-polarization) guide a small fraction of the light to two photodiodes $PD_{1V,1H}$ that allow for a stabilization of the intensity of each polarization component. The relative phases of each polarization component are detected by overlapping them with a reference beam that is not shifted in frequency. The phase of each polarization component is imprinted on the phase of the beat signal at 80 MHz that is recorded by the two photodiodes $PLL - PD_{1V,1H}$. Both photodiodes are fiber coupled to ensure a precise mode matching of the lattice and reference beam that leads to a high signal to noise ratio of the beat signal. Further details of the fast photodiodes and their amplifier stages are described in the appendix B.7. Both beat signals are mixed with a local oscillator frequency to yield a lower the beat frequency to about 10 MHz. Alternatively, the frequency of the reference beam can be shifted by an supplementary AOM to yield a similar beat frequency.

The resulting beat and intensity signals are fed to a Signadyne H3336-F module that digitizes the signals in a analog-to-digital converter with 16 Bit resolution at a sampling rate of 100 MS/s. Each beat signal is compared to a user-defined waveform reference by a phase-frequency-detector which is internally integrated by the manufacturer. The calculated error signal of the phase is fed to an PID controller unit to set the new phase value of each output signal generated at the function generators (FG). The amplitude of each output signal is determined by an additional PID controller using the digitized signals from the photodiodes $PD_{1V,1H}$. All relevant parameters of the control loops can be set from the Matlab environment on the lab computer, see section B.1. The output signal is generated by means of a direct-digital synthesis at 80 MHz and amplified by a power amplifier ZHL-1-2W-S+² to drive the individual AOMs. For practical consideration, it is of high importance that the optical path length of all beams is matched such that common mode phase noise of the laser is not translated into lattice displacements.

We have already set up the optical components of the lattice successfully. Currently, work is underway to enable digital control of beam intensities and phases in contrast to the reported setup in reference [75] where all stabilization are done by analog controllers. The benefit of the digital setup is the possibility to use feed forward techniques to overcome restrictions on the lock bandwidth which is physically limited by the dead time of the AOM due to the traveling time of the sound wave [27].

²Mini-Circuits, Inc.

6. Conclusion and Outlook

In this thesis, I presented an experimental apparatus for the high-resolution ($\text{NA} = 0.92$) single-site detection of single cesium atoms stored in a three-dimensional lattice where the two horizontal lattice directions are state-dependent. The imaging setup as well as the lattice geometry have been characterized by fluorescence images of single atoms stored in the optical lattice. To reduce decoherence, I constructed an ultra-low birefringence glass cell compatible with ultra-high vacuum conditions to suppress polarization distortions of our lattice as well as a double layer magnetic shielding to reduce ambient magnetic field noise. Furthermore, a new scheme and its technical implementation for state-dependent transport in two dimensions were discussed.

Full control over the internal state and the position of atoms will allow the investigation of topology and artificial gauge fields with two-dimensional discrete quantum walks.

6.1. Atoms as Qubits

Single atoms stored in a state-dependent optical lattice in front of a high-resolution objective lens are ideal candidates for quantum walkers including the ability to drive local unitary operations. Any state $|\Psi\rangle$ of our qubit system can be expressed as a superposition of the two basis states $\{|\uparrow\rangle = |F = 4, m_F = 4\rangle, |\downarrow\rangle = |F = 3, m_F = 3\rangle\}$. The dynamical evolution of $|\Psi\rangle$ and interaction of this state with a microwave radiation field can be described in a semi-classical ansatz by the so-called “optical Bloch equations”. An extension of these equations introduces phenomenologically damping terms: the population relaxation time T_1 (also called “longitudinal relaxation time”) and the relaxation time of coherences T_2 (also referred to as “total transverse dephasing time”). These damping terms are necessary to account for decoherence and optical pumping caused by e.g. spontaneous Raman scattering, and dephasing due to, e.g. a variations of differential light shifts [37, 164].

6.1.1. Population Relaxation Time

We determine the population relaxation time in the optical lattice by preparing all atoms in either $|\uparrow\rangle$ or $|\downarrow\rangle$ and observing the temporal evolution of the population. The procedure is as follows [27, 164]: We take a first image of atoms in our deep three-dimensional lattice. Afterwards we prepare all atoms in state $|F = 3\rangle$ by illuminating them for 25 ms with cooling laser light (30 nW) or in $|F = 4\rangle$ using the repumper laser light (35 nW), respectively. Following the state preparation, we lower the horizontal lattice potential depth by a factor of 5.3 to $k_B \times 115 \mu\text{K}$ within 2 ms and wait for a given hold time. Subsequently, atoms in the state $|F = 4\rangle$ are resonantly heated out of the lattice by illumination with a resonant laser (top vertical MOT beam, 30 nW power). Afterwards,

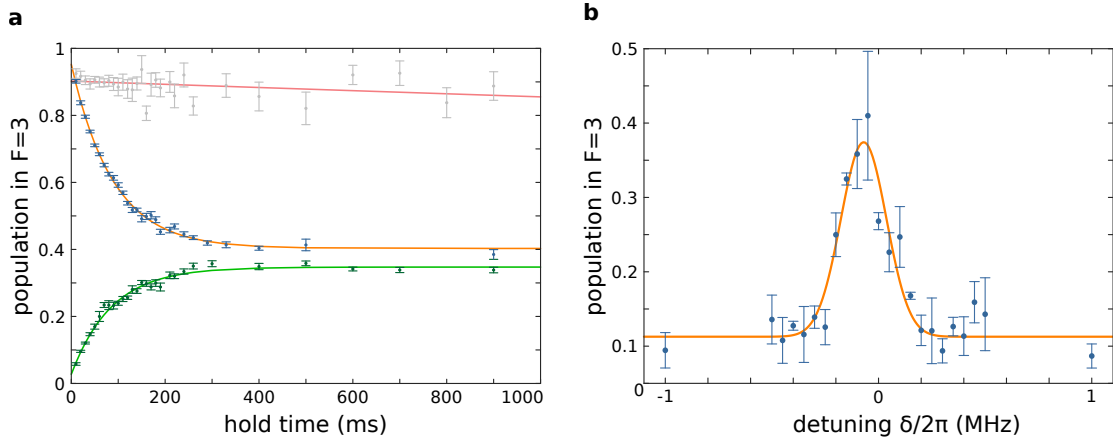


Figure 6.1.: (a) Measurement of the population relaxation time for atoms initially prepared in $|F = 4\rangle$ (green) and $|F = 3\rangle$ (blue). Solid lines correspond to exponential fits following the model from equations 6.1. The data is corrected for the slow exponential losses due to background gas collisions which is measured individually without push-out laser (gray). (b) Microwave spectrum without bias magnetic field. The solid line is a Gaussian fit to determine the width and the center position.

we record a second fluorescence image of the remaining atoms in $|F = 3\rangle$. To compensate for background light, we record an additional image where all atoms have been removed by lowering the lattice depth and using near resonant radiation (top vertical MOT beam). We infer the number of atoms from the integrated fluorescence counts over the entire picture to gain more statistics as compared to using only the clearly resolved atoms in focus of the objective lens.

The temporal evolution of the number of atoms in the state $|F = 3\rangle$ ($|F = 4\rangle$) follows the optical Bloch equation with damping and can be approximated by

$$P_{3,4}(t) = P_{3,4}^{ss} - (P_{3,4}^{ss} - P_{3,4}(0)) \exp\left(-\frac{t}{T_1}\right), \quad (6.1)$$

where $P_i^{ss} = \lim_{t \rightarrow \infty} P_i(t)$ is the steady state population, and T_1 the $1/e$ population decay time. The parameter $P_3(0)$ ($P_4(0)$) is introduced to account for imperfections in the initial state preparation. A non-linear regression of these function to the normalized fluorescence data (see figure 6.1(a)) yields decay constants of $89(2)$ s for atoms that are initially prepared in $|F = 4\rangle$ and $86(4)$ s for atom prepared in $|F = 3\rangle$, respectively. This relaxation time is in the same order of magnitude as for a slightly lower lattice depth in one dimension where it could be shown that the time is limited by the scattering rate with lattice photons at 866 nm [27].

6.1.2. Microwave Driven Transitions

Using the microwave setup described in section 4.3.3, we recorded first results for probing transitions between the qubit states by resonant microwave pulses. The experimental procedure is similar to the relaxation time measurement with the exception of additional

m_F -optical pumping in a weak magnetic bias field (2×10^{-4} T) to prepare the initial state $|\uparrow\rangle$ and a microwave pulse in the lower lattice to drive a transition to $|\downarrow\rangle$. For m_F -optical pumping, we use a beam of the the optical pumping laser (see section 3.3.1) with a power of 30 nW and a σ^+ polarization which is overlapped with beam HDT₁ (see figure 4.3). The microwave square pulse (6 W for 40 μ s) induces transitions to $|\downarrow\rangle$ depending on the detuning δ from the hyperfine transition. The background-corrected ratio of the integrated fluorescence of the first and second picture determines the population in the state $|\downarrow\rangle$.

We confirmed that we prepare the correct Zeeman substate $|\uparrow\rangle = |F = 4, m_F = 4\rangle$ state by measuring the shift of the transition frequency in an external magnetic bias field. A first exemplary spectrum is shown in figure 6.1(b) for the case of no bias field (and hence only preparation of the state $|F = 4\rangle$). The center of the peak is located at a detuning of $\delta_0 = -2 \times 60(8)$ kHz corresponding to a residual magnetic field of $B_{\text{res}} = 24(3)$ mG, which is about one order of magnitude lower than the Earth’s magnetic field in this direction. The width of the peak amounts to $\Delta\delta = 2\pi \times 108(10)$ kHz which is an indication for power broadening or this transition [164]. In the next steps, we will improve the population transfer efficiency of microwave pulses in order to select a plane of atoms in a magnetic field gradient (see 4.3.3).

6.2. Addressing Individual Atoms

Despite global state rotations, the manipulation of individual atoms in the optical lattice is a key ingredient for the preparation of arbitrary initial states such as arbitrary patterns [135] and low entropy states [116, 117, 165]. Typical methods for local addressing rely on driving microwave transitions in the presence of magnetic field gradients where the Zeeman effect causes spatial dependence [31, 76–78] or focused laser beams via light-shifts [135, 136]. While both techniques achieve high efficiencies for classical population transfer, precise local addressing without affecting the neighboring sites and maintaining the coherences has only been shown recently by the method using light shifts [134, 137, 138]. Our state of the art objective lens is ideally suited to project light patterns with a high spatial resolution onto the atoms with minimal cross-talk to neighboring sites which should enable us to further improve on the reported local gate fidelities. Controlling the light pattern is achieved by, e.g. acousto-optical deflectors or spatial light modulators that modify the phase (LCOS¹) or intensity of a light beam (DMD²). This method will allow us to prepare low entropy states in a bottom-up approach by using the state-dependent transport to shift selected atoms into a dense pattern in combination with further cooling methods to reach the internal ground state.

6.3. Vibrational Ground State Cooling

After fluorescence imaging, cesium atoms typically have a temperature of a few tens of microkelvins in a deep optical lattice [27, 99]. Reducing the temperature to the vibra-

¹Liquid Crystal On Silicon

²Digital Mirror Device

tional ground state greatly improves the dephasing time T_2 [36, 37], and is a pre-requisite for experiments with indistinguishable particles. In contrast to a Mott insulator state, which requires the generation of a Bose-Einstein condensate, resolved-sideband cooling in a deep optical lattice enables the transfer of atoms into the vibrational ground state after imaging. In the resolved-sideband regime, the separation between vibrational energy levels in the optical lattice are resolved by using two-photon Raman transitions or microwave transition in state-dependent potentials. While the first approach causes a change in the kinetic energy due to the momentum of a photon [166, 167], the second depends on a change in potential energy change due to the relative lattice displacements of the two lattices for the two states [145, 162, 168].

In our experiment, this displacement can be achieved with the state-dependent lattice in the horizontal directions to implement the robust microwave sideband cooling technique. In the vertical direction, additional Raman beams will be employed to achieve a high vibrational ground state population. Since we have strong confinement in all dimensions, efficient three-dimensional ground state should be possible [168].

6.4. Quantum Simulation Enabled by Quantum Walks in Two Dimensions

The technique of state-dependent transport and global as well as site-resolved addressing enable the realization of a variety of quantum walk protocols to simulate interesting quantum systems. The unitary discrete-time quantum walk operator consist of a coin and a shift operation. The operator is acting on the Hilbert space $H = H_q \otimes H_p$ which is created by the internal qubit state (H_q) and the discrete positions in the periodic array of lattice sites (H_p). In one dimension, a simple walk operator is the so-called “split-step walk” [15]

$$W_{1D} = S^\downarrow C(\theta_2) S^\uparrow C(\theta_1). \quad (6.2)$$

The coin operator $C(\theta_i)$ creates a superposition of qubit states and a shift operator S^\uparrow (S^\downarrow) translates the wavefunction of the state $|\uparrow\rangle$ ($|\downarrow\rangle$) by one lattice site along the positive (negative) direction. Uniform global coins are driven by pure microwave transitions while shift operations correspond to transport in the two-dimensional state-dependent lattice [18]. Spatially varying (local) coin operations will be realized by projecting light patterns created by a spatial light modulator (SLM) via the high numerical aperture objective lens onto the atoms [15]. The projected light either drives the transition directly via Raman transitions or causes light shifts which are resolved by microwave transitions.

6.4.1. Topologically Protected Edge States

In two dimensions, the emergence of topologically protected edge states in a driven Floquet topological insulator system can be studied with the walk operator

$$W_{\text{PES}} = S_y^\downarrow S_y^\uparrow C(\theta_2) S_x^\downarrow S_x^\uparrow C(\theta_1). \quad (6.3)$$

The lower index for the shift operator indicates which of the two directions is used for transport. If two bulk regions of differing coin angles get in contact, protected edge states

emerge at the boundaries that can transport (population) currents. The number of edge states are determined by the invariants according to the bulk-boundary correspondence principle. These states are robust against deformations as well as disorder and can still be observed when a small amount of decoherence is present in the system [15]. We plan to realize the phase boundaries by driving the coin operations with projecting Raman beams of spatially varying intensity and hence Rabi frequencies [15].

6.4.2. Artificial Magnetic Fields

In addition, the physics of a charged particle in a strong magnetic field can be simulated via the walk operator

$$W_{\text{AMF}}(\xi) = S_x^\downarrow S_x^\uparrow H F(\xi) S_y^\downarrow S_y^\uparrow H, \quad (6.4)$$

where H is the Hadamard coin that creates an equal superposition of basis states and $F(\xi)$ is a state-dependent phase shift operator that mimics the phase shift caused by a uniform magnetic field according to $\xi = \Phi(x) = Bx$ [169]. The acquired phase per plaquette in one step can reach values up to 2π , which would correspond to magnetic fields of a few kiloteslas in solid-state crystal lattices. This is way more than the 100 T that can be classically realized with a non-destructive magnet [170].

A. Error Propagation

In physics, Gaussian error propagation [171] is an often employed statistical tool, that assumes normal distributed parameters and depends on the first partial derivatives of a given function with respect to its parameters. The advantage of this procedure is an analytic expression for the propagated error. However, it is only valid up to first order terms, i.e. for (almost) linear functions. Even a non-linear function as simple as the ratio of two rational numbers is known to eventually result in asymmetric confidence intervals, which cannot be described in this framework [172]. Thus, a more general approach based on Monte-Carlo sampling [173] is used in this thesis to propagate errors for arbitrary functions and initial distributions. The basic idea consists in generating Monte-Carlo Samples for each function parameter, that obeys a certain given probability distribution, and evaluating the resulting distribution to determine the confidence interval and the function value.

The collaborative work with Carsten Robens [27] to implement this technique in Matlab is available online [174]. The code consists of three functions: to generate Monte-Carlo parameters, to propagate errors given a function in combination with Monte-Carlo Samples for its parameters, and a function to generate a probability density function from a *fittype*-object in Matlab, as shown in the following example.

```
%% generate probability density function from fittype object
t = 0:2:20;
y = 5*exp(-t/5) + (rand(size(t))-0.5);
f = fit(t', y', 'exp1'); % exponential fit

% results for particular data y:
% f =
%   General model Exp1:
%   f(x) = a*exp(b*x)
%   Coefficients (with 95% confidence bounds):
%     a =      5.924 (4.977, 6.871)
%     b =     -0.1322 (-0.1676, -0.09681)

pdf = generatePDF(f, 1);
```

The resulting discretized probability density array is plotted in figure A.1 a and is subsequently used to generate Monte-Carlo Samples:

```
%% generate MonteCarlo Samples
A = generateMCparameters('function', pdf); % distributed according to pdf

B = generateMCparameters('gaussian', [0.5, 0.2]); % normal distribution
```

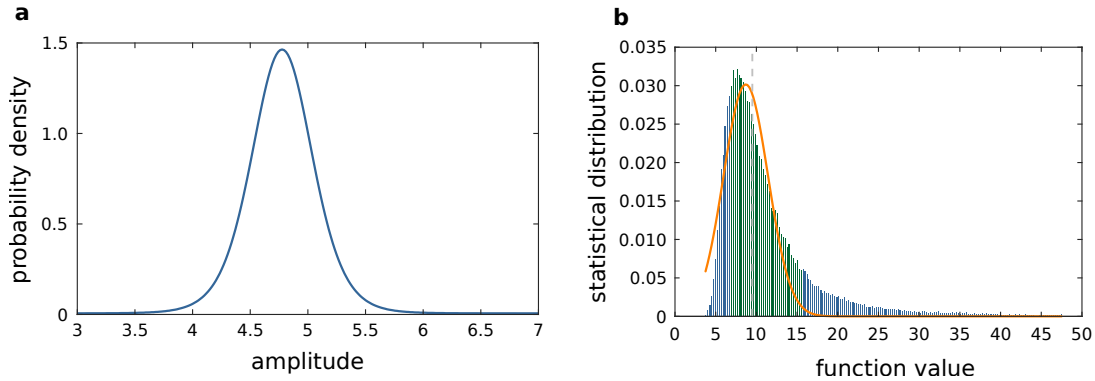


Figure A.1.: (a) Probability density function (PDF) calculated for parameter fits in Matlab. (b) Statistical distribution of 10^5 Monte-Carlo samples for the ratio of the given PDF and a normal distributed parameter with given mean (0.5) and standard-deviation (0.2). The orange curve is a Gaussian fit to the data to visualize the asymmetry of the statistical distribution. The dashed gray line represents the median value of the distribution while the green color indicates the 0.68 confidence interval.

In addition, binomial and bootstrapping methods, as well as option to set the number of samples (typically 10^5), are available for the function `generateMCparameters()`. The function value and its confidence interval are determined by `propagateErrorsWithMC()`, which is used to generate the distribution shown in figure A.1 b.

```

%% Propagate Errors
fun = @(x) x(1)/x(2); % functional to probe
[funValue, funCI, funSamples] = propagateErrorWithMC(fun, [A; B]);
%
% Monte Carlo: 11.79 [7.98 - 20.37]
% Gaussian Fit: 10.86 [7.23 - 14.48]

```

The standard approach for determination of the function value is the meridian of the sample distribution, which is the most robust one. Alternatives are the mean of the distribution or the most probable value.

B. Personal Additions to the Laboratory Infrastructure

In the following appendix I will provide more details on the lab infrastructure and the technical components, that are used to operate the presented experimental apparatus in an efficient manner. A focus of this work was the design of a system, that records important environmental and experimental data in order to facilitate a later correlation analysis of the data. Such an analysis might eventually lead to further improvement of the apparatus. An overview of the system is given in figure B.1.

The central control element of the experimental apparatus is the lab computer featuring a Microsoft Windows 10 operating system, that interacts with various external devices. Its functionality can be divided into two distinct parts: the acquisition and processing of environmental data (server and browser), and the ability to provide a unified interface to all measurement and control devices in a programmable environment.

B.1. Computer Control

Server The server part is based on a Debian Weezy [175] operating system, that is executed as a guest system in an Oracle VM VirtualBox environment. VirtualBox realizes virtualization by intercepting the access to the hardware from the guest system and subsequently executing the commands in a special environment (on the host system) such that the guest system is running independently from the host system [176]. Virtualization offers a higher degree of security by separating the externally accessible server processes of the guest system from the operating system of the host. The ability to take snapshots for backup purposes and migration to other system in the case of failures is a further advantage of virtualization [177].

Two distinct web servers (Tornado [178] and Apache [179]) are running on the guest system to enable access to and visualization of the data from a browser on the host system via IP¹ port forwarding provided by Virtualbox. On the one hand the Tornado web server is used for communication with the power meter device, which is described in more detail in B.2. The Apache web server on the other hand is used to regularly execute PHP scripts [180] for polling environmental data from the ion pump over a USB² connection, as well as from the air conditioning system over a TCP³ connection, and for saving the data into a MySQL [181] database running on the guest operating system. Furthermore, Apache provides a simple interface for external clients, that are connected

¹Internet Protocol

²Universal Serial Bus

³Transmission Control Protocol

over a local Ethernet cable, to store data into the MySQL database and to visualize the data in a web browser chart powered by the javascript chart library dygraphs [182].

Controller The controller consists of self-written scripts and objects within a Mathworks Matlab environment to create sequences for output devices and to acquire measurement data. Each external devices is represented by a Matlab object in order to provide a unified interface and to hide the low-level implementation details of each individual device driver from the user for better code readability. Most importantly, it creates three permanent objects in the Matlab workspace:

- 'ad': A general sequencer used for all analog and digital channels of the ADwin Pro II⁴ device.
- 'sd': A sequencer for vector generator outputs, that interfaces the H3336F modules⁵ for intensity and phase control of all lattice beams and the microwaves radiation.
- 'camera': An EMCCD camera interface to our Andor iXon camera for imaging atoms in the optical lattice.

In addition, I programmed scripts to generate and execute experimental sequences, as well as dedicated measurement classes for data analysis and storage in Matlab's proprietary file format '.mat' using version 7.3. If necessary, environmental data from the MySQL database can be imported directly into the Matlab workspace for further analysis. A in depth description of the functionality and the structure of the written Matlab code lies out of the scope of this work due to its size of a couple of thousand lines of the source code.

For the sake of completeness, it should be mentioned that there are more USB devices connected to the computer, see figure B.1. These devices are typically controlled by individual applications provided by the respective manufacturer. However, I will focus in the following sections on my own electronic developments: a power meter (B.2), a temperature interlock (B.3), a window comparator (B.4). Furthermore, circuits used for controlled vacuum baking (B.5), plasma cleaning of the vacuum cell (B.6), an amplifier box for the fast photodiode of the phase-locked loop (B.7), and a modulation board for our interference lasers (B.8) are presented.

⁴Jäger Messtechnik GmbH

⁵Signadyne Spain S.L.U., merged with Keysight Technologies, Inc. on 2016-07-04

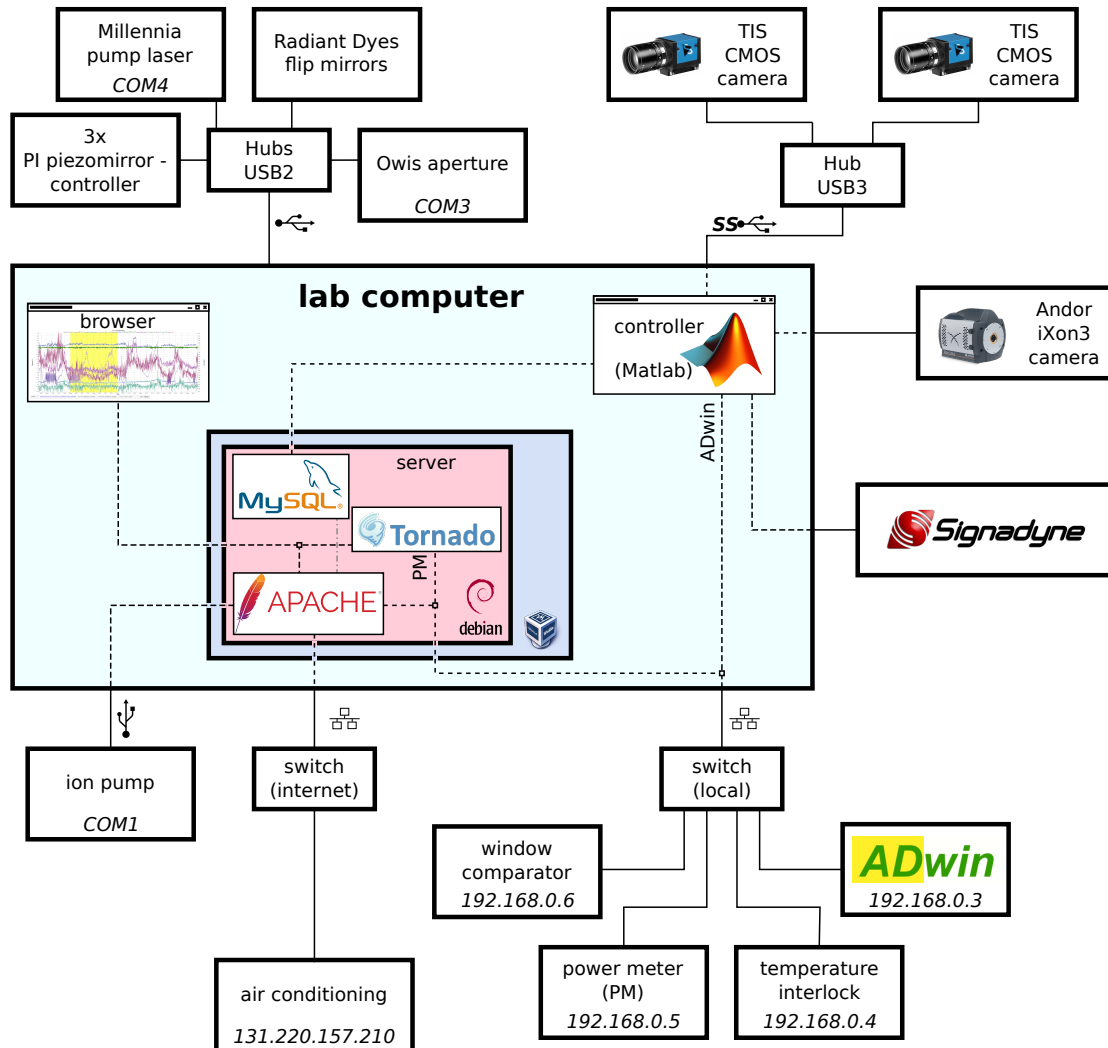


Figure B.1.: Simplified overview of electronic lab equipment used for controlling the experiment and logging of environmental data. The notation COM_x refers to a (virtual) serial port while $x.x.x.x$ indicates an IP address.

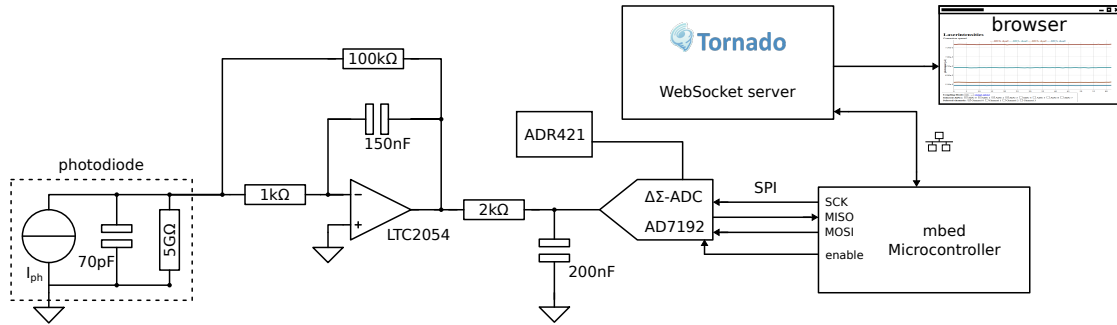


Figure B.2.: Simplified Schematic of the 32 channel power meter circuit.

B.2. Power Meter

The presented experimental setup makes extensive use of fiber connections to guide laser light from different parts of the setup to the vacuum chamber of the experiment. While this modular design enables a high flexibility for tests and repairs it suffers from slow intensity drifts over time, that might eventually degrade the coupling efficiency of the laser light into each fiber. Thus, a power meter is placed behind each fiber output to allow for a fast optimization of the coupling on a daily basis.

Since power meters with many outputs are commercially not available I developed a power meter device with up to 32 channels as sketched in figure B.2. The photocurrent of a BPW-34⁶ photodiode is amplified by gain of $0.1 \text{ V}/\mu\text{A}$ in transimpedance amplifier circuit featuring the operational amplifier LTC2054⁷ adapted from [183]. The additional 150 nF capacitance results in a low-pass filtering to avoid oscillations due to the high gain. The overall bandwidth of this circuit is 10 Hz to match the sampling frequency of the Σ - Δ analog-to-digital (ADC, see [184]) converter AD7192⁸. This chip features four channels with an amplitude resolution of 24 Bit at a sampling rate of up to 4.8 kS/s and an digital notch filter that suppresses 50 Hz oscillations, as well as higher harmonics of the same frequency. However, low-noise operation also demands for a ultra-precision voltage reference at 2.5 V realized with an ADR421⁹.

Eight of these chips are connected via an SPI¹⁰ to an mbed microcontroller board [185], that establishes a bidirectional websocket [186] connection to a tornado web server instance on the lab computer, see B.1, and subsequently transmits the data of all $8 \times 4 = 32$ channels. Tornado is a python web server framework [178] controlled by a self-written python script to receive data from sensors and to distribute the sensor data to web clients. The data is then displayed to the user in real-time using a web browser interface that receives the data through a websocket connection to the tornado server.

The presented system features a measured noise-free resolution of $20.0(5) \text{ Bit}$ at a sampling rate of 10 S/s , which coincides with the specifications of the data sheet of the ADC.

⁶Osram Opto Semiconductors GmbH

⁷Linear Technology Corporation

⁸Analog Devices, Inc

⁹Analog Devices, Inc.

¹⁰Serial Peripheral Interface Bus

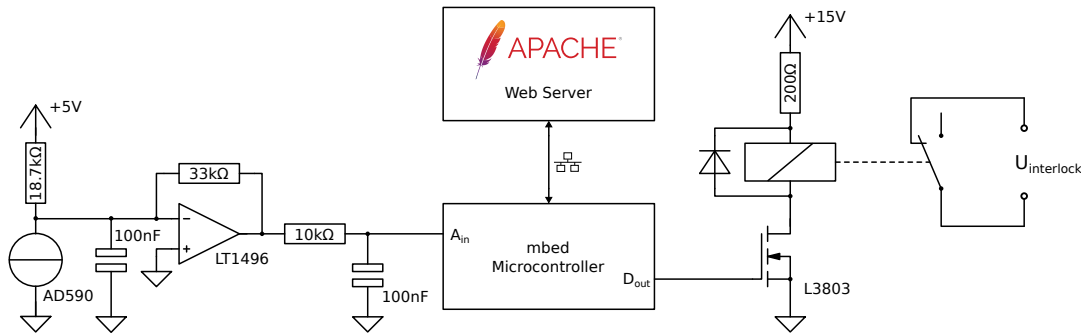


Figure B.3.: Simplified schematic of the temperature interlock circuit for controlling the power supply of the magnetic gradient coils

The dynamic range enables to measure photocurrents up to $25 \mu\text{A}$, that correspond to typical laser powers of up to $42 \mu\text{W}$ at a wavelength of 852 nm and may vary for other wavelengths due to the wavelength-dependent sensitivity curve of the photodiode.

B.3. Temperature Interlock

In the following section, I will provide more details on a safety interlock for the power supply of the magnetic gradient coils, which are presented in section 3.2. This circuit is supposed to prevent overheating of the gradient coils during a failure of the power supply or the water cooling system.

It is based on four AD590¹¹ temperature sensors, that conduct $1 \mu\text{A}/\text{K}$ of current and are attached to each gradient coil and cooling plate. An additional resistor to a voltage reference of 5 V changes the current offset to $0 \mu\text{A}$ at 0°C as depicted in figure B.3. The resulting current is amplified by a transimpedance amplifier stage featuring a LT1496¹² operational amplifier with a gain of $33 \text{ k}\Omega$. This way, the output voltages of this stage for temperatures between 0°C and 100°C cover the full dynamic range $[0 \text{ V}, 3.3 \text{ V}]$ of the successive approximation analog-to-digital converter (12 Bit) integrated in a mbed microcontroller [185].

If one out of the four recorded temperatures is above 35°C a relay will activate the interlock circuit used by the power supply leading to a shutdown of the current. In addition, all temperatures as well as the status of the interlock are sent to the Apache web server interface on the lab computer, where they are stored in a MySQL database. The data is visualized in a web browser, see section B.1.

¹¹Analog Devices, Inc.

¹²Linear Technology Corporation

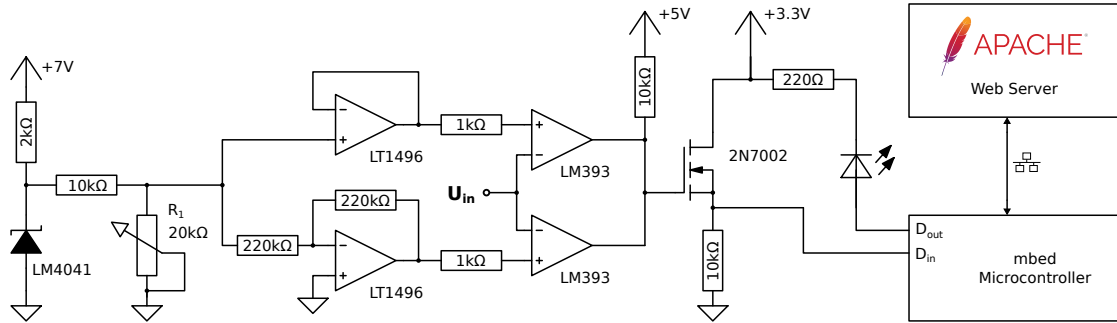


Figure B.4.: Simplified schematic of the window comparator to monitor the error signal of control loops for frequency stabilization of lasers.

B.4. Window Comparator

Besides the temperature of the magnetic coils, the error signal of the proportional-integral controller used for the stabilization of laser frequencies need to be monitored to detect out-of-lock conditions. Although recent improvements in the laser design using interference filters [103] and electronic low pass filters (see section B.8) increased the reliability of the control loops, out-of-loop conditions still appear on a regular basis. The simplified circuit is depicted in figure B.4 and can be divided into an analog and a digital part.

Based on my idea the analogue part of the circuit has already been tested in a smaller version in [95] before I designed a miniaturized version with four channels. The threshold voltage of the window comparator is set by the potentiometer R_1 , that controls the division factor of a shunt voltage reference LM4041¹³ (1.225 V).

The resulting voltage is split into two paths: one for buffering (upper path) and one for inversion (lower path) using LT1496¹⁴ operational amplifiers. These voltages are by definition symmetric around 0 V and define the thresholds for two LM393¹⁵ comparators. Any external signal U_{in} beyond these thresholds increases the gate voltage of a transistor 2N7002 resulting in a 3.3 V input voltage at a digital input pin of the mbed microcontroller [185]. In this case, the microcontroller activates a light-emitting diode for visual feedback and establishes a HTTP¹⁶ connection to the Apache web server (see section B.1) in order to save the state of the window detector and a timestamp in a database. Users can access the database table through a web browser interface or a Matlab script for taking appropriate actions during the execution of a measurement procedure, for instance stopping the execution and informing the staff.

Herr Kalb from our electronic workshop designed a proper housing for the board, see figure B.5, that is fully compatible with 19" rack mounts since its outer dimensions are identical to those of the proportional-integral controller.

¹³Texas Instruments Incorporated

¹⁴Liner Technology, Inc.

¹⁵Texas Instruments Incorporated

¹⁶Hypertext Transfer Protocol



Figure B.5.: Front view of the window comparator device: The window sizes of four channels can be controlled by individual precision potentiometers. Out-of-Range conditions are indicated by light-emitting diodes and send to the lab computer via an Ethernet interface.

B.5. Controlled Vacuum Baking

An ultra-high vacuum at room temperature can be achieved by a thorough cleaning of all vacuum components and a final baking of the assembled vacuum apparatus to assure that all water molecules are desorbed from the chamber walls. This heating is typically realized by heating wires wrapped around the vacuum chamber in combination with a few layers of aluminum foil to insulate the system from the cold environment.

As mentioned in section 2.3, the fragility of the presented UHV glass cell hosting the objective requires to limit the maximum baking temperature, as well as temporal temperature gradients, to about a few Kelvin per second. Furthermore, spatial temperature variations at the glass cell need to be kept at an absolute minimum. This high degree of temperature control and logging has not been available. Hence, I designed and assembled a temperature controller for up to four heating wires with programmable heating profiles and two analog input channels to monitor the vacuum pressure in the system during the heating process.

The two analog inputs include an inverting amplifier with adjustable gain and low-pass filter to map the analog voltage range of the Varian-MultiGauge Controller [187] to the dynamic range ($[0\text{ V}, 3.3\text{ V}]$) of an mbed microcontroller [185], see figure B.6. Up to four cold-junction compensated sensor boards MAX31855¹⁷ for thermocouple sensors are connected to the microcontroller via an SPI¹⁸ interface bus. The sensor boards offer a 14 Bit resolution of the temperature ($0.25\text{ }^{\circ}\text{C}/\text{Bit}$) at a sampling rate of about 1 S/s.

¹⁷Maxim Integrated

¹⁸Serial Peripheral Interface Bus

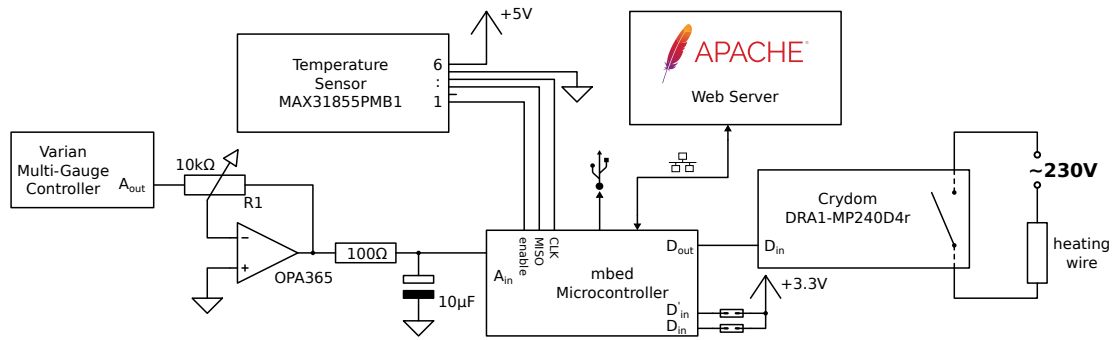


Figure B.6.: Simplified schematic of a temperature control loop used for a single heating wire.

The current of a heating wire is controlled by a pulse-width modulated signal that is transferred to the operating voltage of the wire by means of a solid-state relay DRA1-MP240D4R¹⁹. The resulting peak-to-peak temperature variation depends on the system but is typically in the range of a few Bits. Lowest temperature variations are achieved if the in-loop temperature sensor is placed as close as possible to its heating wire in order to reduce the dead-time in the transfer function of the loop.

All control parameters of four independent loops can be set via a virtual serial interface over a USB connection. In ramp mode, two jumpers indicate whether the heating is decreased (D_{in}) or increased (D'_{in}). The maximum temperature as well as the temperature increase per time can be adjusted to personal needs. Furthermore, the increase of the vacuum pressure due to heating can be limited to certain values if the controller is in ramp mode and the pressure in the system should stay relatively low.

The temperature and pressure data is also logged to an Apache web server on the lab computer, see section B.1 for monitoring purposes.

¹⁹Crydom

B.6. Circuit for Plasma Cleaning

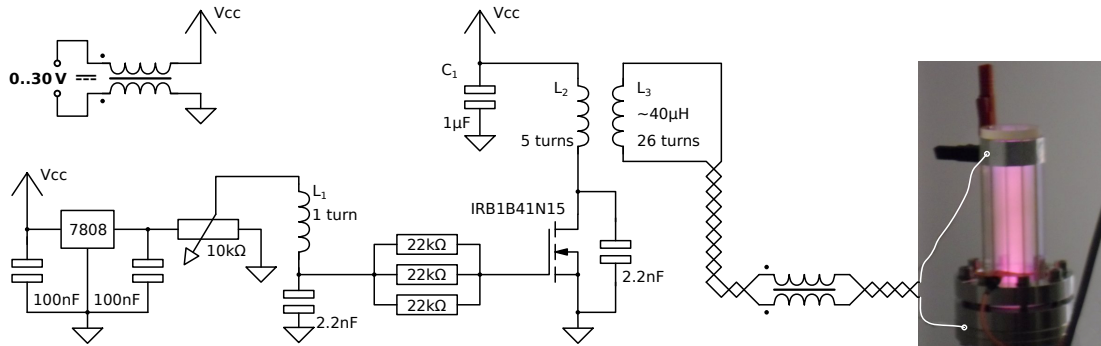


Figure B.7.: Circuit for self-resonant plasma generator to create a cold Argon plasma glow discharge.

Cleaning the vacuum glass cell from absorbed molecules and atoms that are attached to the cell surfaces is done by a cold argon plasma, as mentioned in section 2.3.2. The circuit is based on the idea of a double self-resonant circuit, which is depicted in figure B.7, to drive the glow discharge by a high frequency oscillation at a few megahertz. The circuit is powered using a DC voltage up to 30 V. The power supply is secured against bias current or differential signals by a common mode choke with a 100 kHz limiting frequency, which is significantly smaller than the resonance frequency of the circuit.

Adjusting the trimmer behind a fixed voltage reference (7808) allows to set the gate voltage of the fast MOSFET²⁰ IRF1B41N15²¹, which causes a voltage rise along the winding of the primary side (L_2) of an air-core transformer. This induces a negative voltage to the winding of L_1 which is spatially overlapped with the transformer leading to a voltage drop at the gate, and thus, an oscillation. The amplitude of the voltage oscillation at the MOSFET gate is set by the 2.2 nF capacitor, that forms a voltage divider with the gate capacitance. Yet, a suitable cooling of the MOSFET chip is necessary. The resonance frequency of this oscillator is set by the capacitance C_1 and the effective inductance L_2 .

The voltage at the secondary side of the transformer is amplified by the winding ratio of coil L_2 and L_3 yielding amplification by a factor of five. Subsequently, this voltage is transmitted through a common-mode choke made of N30 material to prohibit the occurrence of bias currents and differential signals. As a result, all the power is guided to the electrodes of the discharge, i.e. the vacuum chamber and an aluminum foil at the top part of the glass cell. For highest transfer efficiency the windings of the transformer need to be chosen such that the secondary side is also operating at its resonance frequency to achieve highest voltage amplitudes.

Note, that all capacitors are taken from the MKP 10 series manufactured by WIMA Spezialvertrieb elektronischer Bauelemente GmbH & CO.KG since these capacitors withstand high voltage peaks.

²⁰Metal–Oxide–Semiconductor Field-Effect Transistor

²¹ International Rectifier Corporation

Higher harmonics of the oscillation frequencies at the gate voltage reduce the transfer efficiency of the incoming power to the plasma. However, these harmonics also exhibit a strong dependence on the dynamics of the plasma, which can lead to different brightness levels and colors of the resulting plasma. The high power $22\text{ k}\Omega$ resistances are capable of thermally dissipating 2 W of power and are used to suppress higher harmonics at the gate resulting in smaller power dissipation at the MOSFET.

A typical supply voltage of 16.5 V at a DC current of 1.44 A) was used to drive an argon plasma discharge. In this setting, the gate voltage is less than 30 V while the drain-to-source voltage amounts to values up to 150 V corresponding to 780 V at the electrodes. Yet, an additional piezoelectric discharge spark is still required to ignite the plasma.

B.7. Amplifier Box for Fast Photodiode

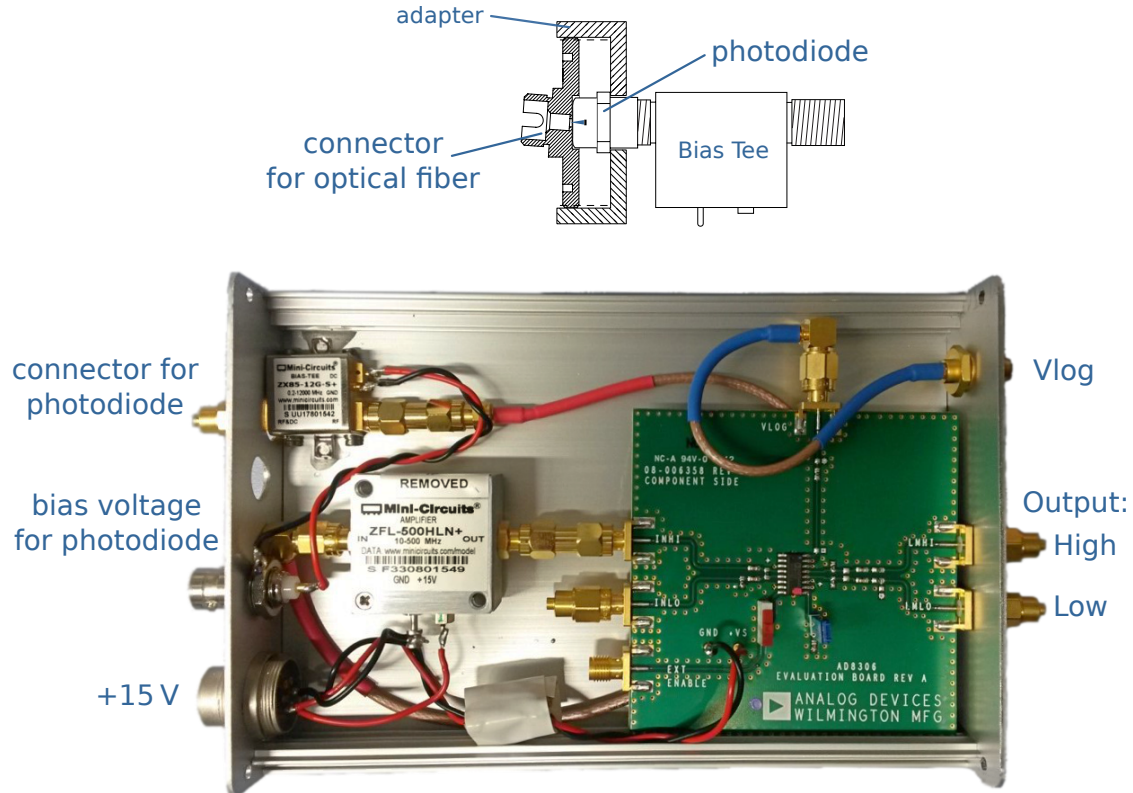


Figure B.8.: Compact box for fiber-coupled, fast photodiode and amplifier stage. The top drawing shows the mounting of a fiber in front of the fast photodiode. See text for circuit description.

Stabilizing the relative phases of the two orthogonal polarization components is a mandatory requirement for the polarization synthesis of the lattice beams for state-dependent transport, see section 5.4. We plan to stabilize each phase of two co-propagating laser beams of orthogonal linear polarization by overlapping an additional reference beam with a shifted frequency. We record beat signals at 80 MHz for each polarization component after separating them at a Wollaston prism. A precise overlap of the reference beam, and thus a large signal-to-noise ratio, is achieved by coupling one polarization component of the synthesized beam and the reference beam into a single mode fiber.

In order to save space on the optical table, the fiber can directly be connected to a fast photodiode attached to an amplifier box as shown in figure B.8. This configuration is realized by a modified holder S1FCA²² for a FC/APC fiber where some metal is removed to allow for a closer proximity between the photodiode and the optical fiber. Due to the small distance between the divergent beam and the photodiode, the total beam power

²²Thorlabs, Inc.

is fully deposited on the sensitive chip area. The fast photodiode G4176-03²³ (response time 30 ps) is held in place by a special adapter plate and is directly connected to a bias tee ZX85-12G-S+²⁴ that provides the bias voltage for the photodiode. An amplifier stage consisting of a 20 dB preamplifier ZFL-500HLN+²⁵ and a limiting-logarithmic amplifier AD8306²⁶ to provide a differential signal with a steep slope at the zero crossing. The signal is forwarded to a FPGA with high speed analog front-end (H3336F modules²⁷), that is internally configured to realize a phase-frequency detector and a proportional-integral controller for stabilization of the polarization phases. The “Vlog” output port can be used to measure the DC offset of the signal. A further integration of the amplifier circuit could provide an even larger sensitivity [188]. However, the presented components have already been used successfully in a different experiment [75] and are known to work for an optical lattice experiment.

In total, I built and tested four boxes for the polarization synthesis of the state-dependent optical lattice.

²³Hamamatsu Photonics K.K.

²⁴Mini Circuits, Inc.

²⁵Mini Circuits, Inc.

²⁶Analog Devices, Inc.

²⁷Signadyne Spain S.L.U., merged with Keysight Technologies, Inc. on 2016-07-04

B.8. Modulation Board for Interference Filter Laser

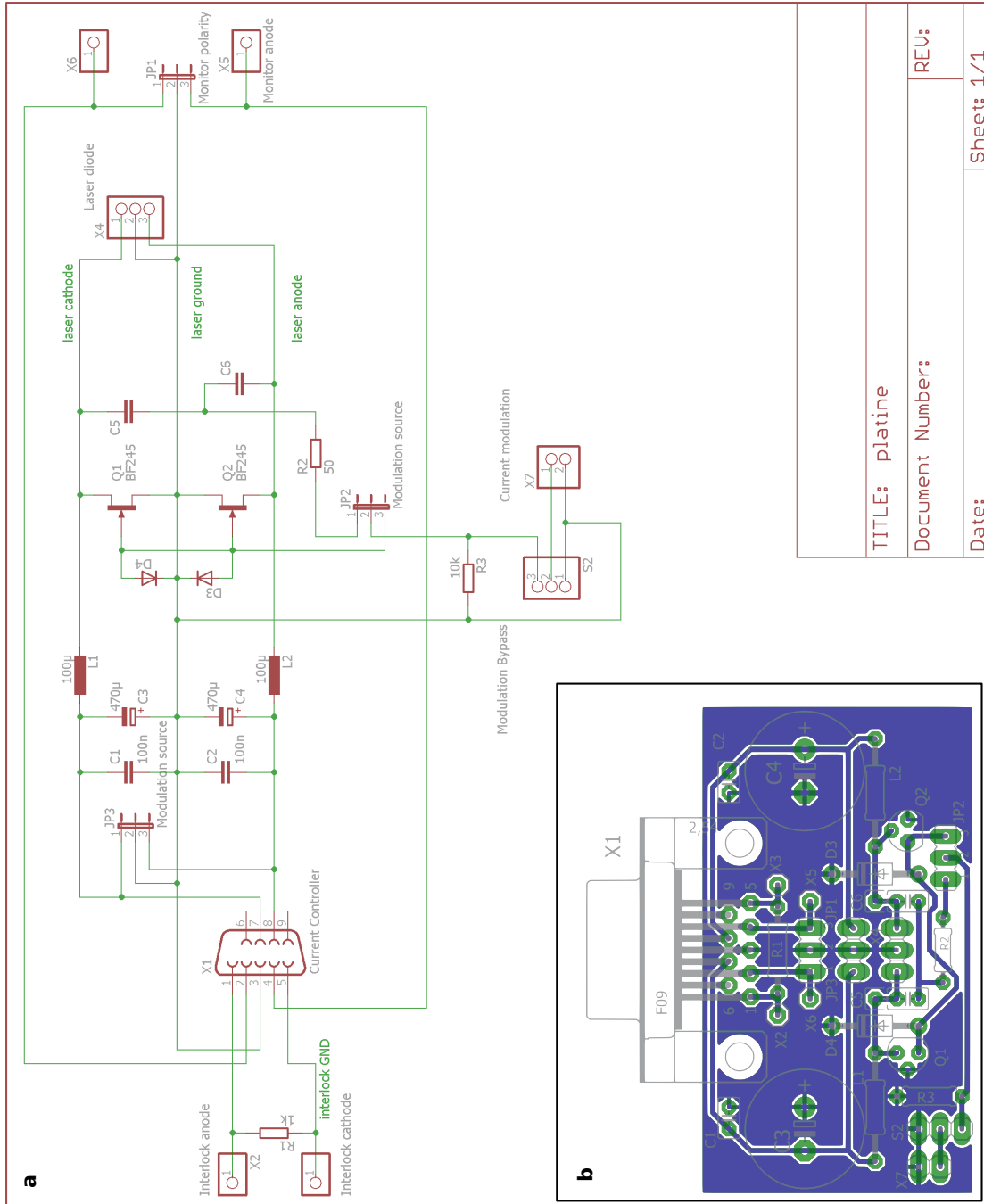


Figure B.9.: Schematic (a) and printed circuit board (b) for ITC102 laser diode Controller from Thorlabs, Inc.

Bibliography

- [1] de Touzalin, Aymard, Charles Marcus, Freeke Heijman, Ignacio Cirac, Richard Murray, and Tommaso Calarco: *Quantum manifesto*. http://qurope.eu/system/files/u7/93056_Quantum%20Manifesto_WEB.pdf, May 2016. Accessed 22-July-2016.
- [2] Gibney, Elizabeth: *Europe plans giant billion-euro quantum technologies project*. *Nature*, 532:426, 2016. <http://www.nature.com/news/europe-plans-giant-billion-euro-quantum-technologies-project-1.19796>.
- [3] Engineering and Physical Sciences Research Council: *Uk national quantum technologies programme*, 2014. https://www.gov.uk/government/uploads/system/uploads/attachment_data/file/470243/InnovateUK_QuantumTech_C0004_final.pdf, Accessed 22-July-2016.
- [4] Investments, Quantum Valley: *Quantum valley investment funds*. <http://www.quantumvalleyinvestments.com/>, Accessed 16-June-2016.
- [5] Merali, Zeeya: *The quantum space race*. *Nature*, 492:22–25, 2012. <http://www.nature.com/news/data-teleportation-the-quantum-space-race-1.11958>.
- [6] Qiu, Jane: *Quantum communications leap out of the lab*. *Nature*, 508:441–442, 2014. <http://www.nature.com/news/quantum-communications-leap-out-of-the-lab-1.15093>.
- [7] Feynman, Richard P.: *Simulating physics with computers*. *International Journal of Theoretical Physics*, 21(6):467–488, 1982, ISSN 1572-9575. <http://dx.doi.org/10.1007/BF02650179>.
- [8] Lloyd, Seth: *Universal quantum simulators*. *Science*, 273(5278):1073–1078, 1996, ISSN 0036-8075. <http://science.sciencemag.org/content/273/5278/1073>.
- [9] Aspuru-Guzik, Alan and Philip Walther: *Photonic quantum simulators*. *Nat. Phys.*, 8:285–291, 2012. <http://dx.doi.org/10.1038/nphys2253>.
- [10] Blatt, R. and C. F. Roos: *Quantum simulations with trapped ions*. *Nat. Phys.*, 8:277–284, 2012. <http://dx.doi.org/10.1038/nphys2252>.
- [11] O’Malley, P. J. J., R. Babbush, I. D. Kivlichan, J. Romero, J. R. McClean, R. Barends, J. Kelly, P. Roushan, A. Tranter, N. Ding, B. Campbell, Y. Chen, Z. Chen, B. Chiaro, A. Dunsworth, A. G. Fowler, E. Jeffrey, E. Lucero, A. Megrant, J. Y.

- Mutus, M. Neeley, C. Neill, C. Quintana, D. Sank, A. Vainsencher, J. Wenner, T. C. White, P. V. Coveney, P. J. Love, H. Neven, A. Aspuru-Guzik, and J. M. Martinis: *Scalable quantum simulation of molecular energies*. Phys. Rev. X, 6:031007, Jul 2016. <http://link.aps.org/doi/10.1103/PhysRevX.6.031007>.
- [12] Bloch, Immanuel, Jean Dalibard, and Sylvain Nascimbene: *Quantum simulations with ultracold quantum gases*. Nat. Phys., 8:267–276, 2012. <http://dx.doi.org/10.1038/nphys2259>.
- [13] Kempe, J.: *Quantum random walks: An introductory overview*. Contemporary Physics, 44(4):307–327, 2003. <http://dx.doi.org/10.1080/00107151031000110776>.
- [14] Ahlbrecht, Andre, Andrea Alberti, Dieter Meschede, Volkher B Scholz, Albert H Werner, and Reinhard F Werner: *Molecular binding in interacting quantum walks*. New Journal of Physics, 14(7):073050, 2012. <http://stacks.iop.org/1367-2630/14/i=7/a=073050>.
- [15] Groh, T., S. Brakhane, W. Alt, D. Meschede, J. Asbóth, and A. Alberti: *Robustness of topologically protected edge states in quantum walk experiments with neutral atoms*. Physical Review A (editor’s suggestion), 94:013620, 2016.
- [16] Shenvi, Neil, Julia Kempe, and K. Birgitta Whaley: *Quantum random-walk search algorithm*. Phys. Rev. A, 67:052307, May 2003. <http://link.aps.org/doi/10.1103/PhysRevA.67.052307>.
- [17] Jessen, P. S., I. H. Deutsch, and R. Stock: *Quantum Information Processing with Trapped Neutral Atoms*, pages 91–103. Springer US, Boston, MA, 2005, ISBN 978-0-387-27732-5. http://dx.doi.org/10.1007/0-387-27732-3_7.
- [18] Karski, Michal, Leonid Förster, Jai Min Choi, Andreas Steffen, Wolfgang Alt, Dieter Meschede, and Artur Widera: *Quantum walk in position space with single optically trapped atoms*. Science, 325(5937):174–177, 2009, ISSN 0036-8075. <http://science.sciencemag.org/content/325/5937/174>.
- [19] Sherson, Jacob F., Christof Weitenberg, Manuel Endres, Marc Cheneau, Immanuel Bloch, and Stefan Kuhr: *Single-atom-resolved fluorescence imaging of an atomic mott insulator*. Nature, pages 68–72, 2011. <http://dx.doi.org/10.1038/nature09378>.
- [20] Preiss, Philipp M., Ruichao Ma, M. Eric Tai, Alexander Lukin, Matthew Rispoli, Philip Zupancic, Yoav Lahini, Rajibul Islam, and Markus Greiner: *Strongly correlated quantum walks in optical lattices*. Science, 347(6227):1229–1233, 2015, ISSN 0036-8075. <http://science.sciencemag.org/content/347/6227/1229>.
- [21] Schreiber, Andreas, Aurél Gábris, Peter P. Rohde, Kaisa Laiho, Martin Štefaňák, Václav Potoček, Craig Hamilton, Igor Jex, and Christine Silberhorn: *A 2d quantum walk simulation of two-particle dynamics*. Science, 336(6077):55–58, 2012, ISSN 0036-8075. <http://science.sciencemag.org/content/336/6077/55>.

-
- [22] Nitsche, Thomas, Fabian Elster, Jaroslav Novotný, Aurél Gábris, Igor Jex, Sonja Barkhofen, and Christine Silberhorn: *Quantum walks with dynamical control: graph engineering, initial state preparation and state transfer*. New Journal of Physics, 18(6):063017, 2016. <http://stacks.iop.org/1367-2630/18/i=6/a=063017>.
- [23] Zähringer, F., G. Kirchmair, R. Gerritsma, E. Solano, R. Blatt, and C. F. Roos: *Realization of a quantum walk with one and two trapped ions*. Phys. Rev. Lett., 104:100503, Mar 2010. <http://link.aps.org/doi/10.1103/PhysRevLett.104.100503>.
- [24] Schmitz, H., R. Matjeschk, Ch. Schneider, J. Glueckert, M. Enderlein, T. Huber, and T. Schaetz: *Quantum walk of a trapped ion in phase space*. Phys. Rev. Lett., 103:090504, Aug 2009. <http://link.aps.org/doi/10.1103/PhysRevLett.103.090504>.
- [25] Jaksch, D., H. J. Briegel, J. I. Cirac, C. W. Gardiner, and P. Zoller: *Entanglement of atoms via cold controlled collisions*. Phys. Rev. Lett., 82:1975–1978, Mar 1999. <http://link.aps.org/doi/10.1103/PhysRevLett.82.1975>.
- [26] Dür, W., R. Raussendorf, V. M. Kendon, and H. J. Briegel: *Quantum walks in optical lattices*. Phys. Rev. A, 66:052319, Nov 2002. <http://link.aps.org/doi/10.1103/PhysRevA.66.052319>.
- [27] Robens, Carsten: *Testing the Quantumness of Atomic Trajectories*. PhD thesis, Universität Bonn, 2016.
- [28] Soltan-Panahi, P., J. Struck, P. Hauke, A. Bick, W. Plenkers, G. Meineke, C. Becker, P. Windpassinger, M. Lewenstein, and K. Sengstock: *Multi-component quantum gases in spin-dependent hexagonal lattices*. Nature Physics, 7:434–440, 2011. <http://www.nature.com/nphys/journal/v7/n5/abs/nphys1916.html#supplementary-information>.
- [29] Bakr, Waseem S., Jonathon I. Gillen, Amy Peng, Simon Fölling, and Markus Greiner: *A quantum gas microscope for detecting single atoms in a hubbard-regime optical lattice*. Nature, pages 74–77, 2009. <http://dx.doi.org/10.1038/nature08482>.
- [30] Yamamoto, Ryuta, Jun Kobayashi, Takuma Kuno, Kohei Kato, and Yoshiro Takahashi: *An ytterbium quantum gas microscope with narrow-line laser cooling*. New Journal of Physics, 18(2):023016, 2016. <http://stacks.iop.org/1367-2630/18/i=2/a=023016>.
- [31] Haller, Elmar, James Hudson, Andrew Kelly, Dylan A. Cotta, Bruno Peaudecerf, Graham D. Bruce, and Stefan Kuhr: *Single-atom imaging of fermions in a quantum-gas microscope*. Nat Phys, 11(9):738–742, Sep 2015, ISSN 1745-2473. <http://dx.doi.org/10.1038/nphys3403>, Letter.

- [32] Miranda, Martin, Ryotaro Inoue, Yuki Okuyama, Akimasa Nakamoto, and Mikio Kozuma: *Site-resolved imaging of ytterbium atoms in a two-dimensional optical lattice*. Phys. Rev. A, 91:063414, Jun 2015. <http://link.aps.org/doi/10.1103/PhysRevA.91.063414>.
- [33] Cheuk, Lawrence W., Matthew A. Nichols, Melih Okan, Thomas Gersdorf, Vinay V. Ramasesh, Waseem S. Bakr, Thomas Lompe, and Martin W. Zwierlein: *Quantum-gas microscope for fermionic atoms*. Phys. Rev. Lett., 114:193001, May 2015. <http://link.aps.org/doi/10.1103/PhysRevLett.114.193001>.
- [34] Huang, Bo, Hazen Babcock, and Xiaowei Zhuang: *Breaking the diffraction barrier: Super-resolution imaging of cells*. Cell, 143(7):1047–1058, August 2016, ISSN 0092-8674. <http://dx.doi.org/10.1016/j.cell.2010.12.002>.
- [35] Alberti, A., C. Robens, W. Alt, S. Brakhane, M. Karski, R. Reimann, A. Widera, and D. Meschede: *Super-resolution microscopy of single atoms in optical lattices*. New J. Phys., 18:053010, 2016.
- [36] Kuhr, S., W. Alt, D. Schrader, I. Dotsenko, Y. Miroshnychenko, W. Rosenfeld, M. Khudaverdyan, V. Gomer, A. Rauschenbeutel, and D. Meschede: *Coherence properties and quantum state transportation in an optical conveyor belt*. Phys. Rev. Lett., 91:213002, Nov 2003. <http://link.aps.org/doi/10.1103/PhysRevLett.91.213002>.
- [37] Alberti, Andrea, Wolfgang Alt, Reinhard Werner, and Dieter Meschede: *Decoherence models for discrete-time quantum walks and their application to neutral atom experiments*. New Journal of Physics, 16(12):123052, 2014. <http://stacks.iop.org/1367-2630/16/i=12/a=123052>.
- [38] Kuhr, S., W. Alt, D. Schrader, I. Dotsenko, Y. Miroshnychenko, A. Rauschenbeutel, and D. Meschede: *Analysis of dephasing mechanisms in a standing-wave dipole trap*. Phys. Rev. A, 72:023406, Aug 2005. <http://link.aps.org/doi/10.1103/PhysRevA.72.023406>.
- [39] Li, Xiao, Theodore A. Corcovilos, Yang Wang, and David S. Weiss: *3d projection sideband cooling*. Phys. Rev. Lett., 108:103001, Mar 2012. <http://link.aps.org/doi/10.1103/PhysRevLett.108.103001>.
- [40] Gröbner, Oswald: *LHC vacuum system*. CERN, (CERN-OPEN-2000-288), 1999. <https://cds.cern.ch/record/455985>.
- [41] Mandel, Olaf, Markus Greiner, Artur Widera, Tim Rom, Theodor W Hänsch, and Immanuel Bloch: *Controlled collisions for multi-particle entanglement of optically trapped atoms*. Nature, 425:937, 2003.
- [42] Steffen, A, A Alberti, W Alt, N Belmechri, S. Hild, M Karski, A Widera, and D Meschede: *Digital atom interferometer with single particle control on a discretized space-time geometry*. Proc. Natl. Acad. Sci. U.S.A., 109:9770, 2012.

-
- [43] Deutsch, Ivan H. and Poul S. Jessen: *Quantum-state control in optical lattices*. Phys. Rev. A, 57:1972–1986, Mar 1998. <http://link.aps.org/doi/10.1103/PhysRevA.57.1972>.
- [44] Mathur, B. S., H. Tang, and W. Happer: *Light shifts in the alkali atoms*. Phys. Rev., 171:11–19, Jul 1968. <http://link.aps.org/doi/10.1103/PhysRev.171.11>.
- [45] Zhu, Kunyan, Neal Solmeyer, Cheng Tang, and David S. Weiss: *Absolute polarization measurement using a vector light shift*. Phys. Rev. Lett., 111:243006, Dec 2013. <http://link.aps.org/doi/10.1103/PhysRevLett.111.243006>.
- [46] Brakhane, Stefan, Wolfgang Alt, Dieter Meschede, Carsten Robens, Geol Moon, and Andrea Alberti: *Note: Ultra-low birefringence dodecagonal vacuum glass cell*. Review of Scientific Instruments, 86(12), 2015. <http://scitation.aip.org/content/aip/journal/rsi/86/12/10.1063/1.4938281>.
- [47] Schott North America, Inc.: *IE-27: Stress in optical glass, Technical Note*, 2004.
- [48] International Organization for Standardization: *Optics and optical instruments – Preparation of drawings for optical elements and systems – Part 2: Material imperfections – Stress birefringence*. Iso 10110-2:2000-02, International Organization for Standardization, Geneva, Switzerland, 2000.
- [49] Steffen, Andreas, Wolfgang Alt, Maximilian Genske, Dieter Meschede, Carsten Robens, and Andrea Alberti: *Note: In situ measurement of vacuum window birefringence by atomic spectroscopy*. Review of Scientific Instruments, 84(12), 2013. <http://scitation.aip.org/content/aip/journal/rsi/84/12/10.1063/1.4847075>.
- [50] Solmeyer, Neal, Kunyan Zhu, and David S. Weiss: *Note: Mounting ultra-high vacuum windows with low stress-induced birefringence*. Rev. Sci. Instrum., 82:066105, 2011. <http://scitation.aip.org/content/aip/journal/rsi/82/6/10.1063/1.3606437>.
- [51] Studna, A. A., D. E. Aspnes, L. T. Florez, B. J. Wilkens, J. P. Harbison, and R. E. Ryan: *Low-retardance fused quartz window for real-time optical applications in ultrahigh vacuum*. J. Vac. Sci. Technol., A, 7:3291, 1989. <http://scitation.aip.org/content/avs/journal/jvsta/7/6/10.1116/1.576138>.
- [52] Joiner, R. E., J. Marburger, and W. H. Steier: *Elimination of stress-induced birefringence effects in single-crystal high-power laser windows*. App. Phys. Lett., 30:485, 1977. <http://scitation.aip.org/content/aip/journal/apl/30/9/10.1063/1.89458>.
- [53] Meier, G. and H. Kriegs: *A high pressure cell for dynamic light scattering up to 2 kbars with conservation of plane of polarization*. Rev. Sci. Instrum., 79, 2008.
- [54] Chin, Cheng, Rudolf Grimm, Paul Julienne, and Eite Tiesinga: *Feshbach resonances in ultracold gases*. Rev. Mod. Phys., 82:1225–1286, Apr 2010. <http://link.aps.org/doi/10.1103/RevModPhys.82.1225>.

- [55] Hellma GmbH & Co. KG, Klosterrunsstraße 5, D-79379 Müllheim, Germany: . <http://www.hellma-analytics.com/>.
- [56] Precision GlassBlowing, Inc., 14775 E. Hinsdale Ave, Centennial, CO 80112: . <http://www.precisionglassblowing.com/optical-glassware/>.
- [57] ColdQuanta, Inc., 3030 Sterling Circle, Boulder, CO 80301: . <http://www.coldquanta.com/products/ar-coated-glass-cells/>.
- [58] Japan Cell Co., Ltd., Machida Technopark, 2-2-5-11, Oyamagaoka, Machida-shi, Tokyo 194-0215, Japan: . <http://www.jpcell.co.jp/en/>.
- [59] Bach, H. and N. Neuroth: *The Properties of Optical Glass*. Schott Series on Glass and Glass Ceramics. Springer Berlin Heidelberg, 1998, ISBN 9783540583578. <https://books.google.de/books?id=J0RX1mbhzAEC>.
- [60] European Parliament: *Directive 2011/65/eu of the european parliament and of the council on the restriction of the use of certain hazardous substances in electrical and electronic equipment*. Official Journal of the European Union, L(174), 2011. <http://eur-lex.europa.eu/legal-content/EN/TXT/?qid=1399998664957&uri=CELEX:02011L0065-20140129>.
- [61] Jousten, Karl: *Handbook of Vacuum Technology*. Wiley-VCH Verlag GmbH & Co. KGaA, Weinheim, 2008.
- [62] Holynski, Michael: *Creating a two dimensional cold mixture experiment*. PhD thesis, The University of Birmingham, 2012.
- [63] Anderson, D.Z. and J.G.J. Reichel: *Cold atom system with atom chip wall*, 2006. <http://www.google.ch/patents/W02005086946A3?cl=en>, WO Patent App. PC-T/US2005/008,128.
- [64] Epoxy Technology, Inc., 14 Fortune Drive, Billerica, MA 01821-3972 USA: *Removing Bubbles from Epoxy*.
- [65] Schott North America, Inc., 400 York Avenue, Duryea, PA 18642: *Optical Glass - Data Sheets*, 2012.
- [66] Campbell, Flake C.: *Elements of Metallurgy and Engineering Alloys*. ASM International, Materials Park, OH 44073-0002, 2008. <http://www.asminternational.org>.
- [67] Noble, A. and M. Kasevich: *Uhv optical window seal to conflata) knife edge*. Review of Scientific Instruments, 65(9):3042–3043, 1994. <http://scitation.aip.org/content/aip/journal/rsi/65/9/10.1063/1.1144604>.
- [68] Akaishi, K., K. Ezaki, Y. Kubota, and O. Motojima: *Reduction of water outgassing and uhv production in an unbaked vacuum chamber by neon gas discharge*. Vacuum, 53(1):285 – 289, 1999, ISSN 0042-207X. <http://www.sciencedirect.com/science/article/pii/S0042207X98003765>.

-
- [69] Beletic, J.E., J.W. Beletic, and P. Amico: *Scientific Detectors for Astronomy 2005: Explorers of the Photon Odyssey*. Astrophysics and Space Science Library. Springer Netherlands, 2006, ISBN 9781402043307. https://books.google.de/books?id=w0QW3_ErDsQC.
- [70] Alberti, Andrea: *Is it true that a arbitrary 3D rotation can be composed with two rotations constrained to have their axes in the same plane?* Mathematics Stack Exchange, 2014. <http://math.stackexchange.com/q/1021727>.
- [71] Kaminow, Ivan P.: *An Introduction to Electrooptic Devices*. Academic Press, New York, 1974.
- [72] Schäfer, M.M, C Seidel, H Fuchs, and M Voetz: *The suppression of water-diffusion in polycarbonate through ar- and he-plasma as a new model for the origin of improved adhesion of al.* Applied Surface Science, 173(1-2):1 – 7, 2001, ISSN 0169-4332. <http://www.sciencedirect.com/science/article/pii/S0169433200008436>.
- [73] Epoxy Technology, Inc., 14 Fortune Drive, Billerica, MA 01821-3972 USA: *Fresh water absorption test - optical epoxies*.
- [74] Carcia, P. F., R. S. McLean, M. D. Groner, A. A. Dameron, and S. M. George: *Gas diffusion ultrabarrriers on polymer substrates using al2o3 atomic layer deposition and sin plasma-enhanced chemical vapor deposition*. Journal of Applied Physics, 106(2), 2009. <http://scitation.aip.org/content/aip/journal/jap/106/2/10.1063/1.3159639>.
- [75] Robens, Carsten, Jonathan Zopes, Wolfgang Alt, Stefan Brakhane, Dieter Meschede, and Andrea Alberti: *Low-entropy states of neutral atoms in polarization-synthesized optical lattices*. arXiv:1608.02410, 2014.
- [76] Karski, M., L. Förster, J. Choi, A. Steffen, N. Belmechri, W. Alt, D. Meschede, and A. Widera: *Imprinting Patterns of Neutral Atoms in an Optical Lattice using Magnetic Resonance Techniques*. New J. Phys., 12:065027, 2010.
- [77] Fölling, Simon, Artur Widera, Torben Müller, Fabrice Gerbier, and Immanuel Bloch: *Formation of spatial shell structure in the superfluid to mott insulator transition*. Phys. Rev. Lett., 97:060403, Aug 2006. <http://link.aps.org/doi/10.1103/PhysRevLett.97.060403>.
- [78] Edge, G. J. A., R. Anderson, D. Jervis, D. C. McKay, R. Day, S. Trotzky, and J. H. Thywissen: *Imaging and addressing of individual fermionic atoms in an optical lattice*. Phys. Rev. A, 92:063406, Dec 2015. <http://link.aps.org/doi/10.1103/PhysRevA.92.063406>.
- [79] Chin, Cheng, Rudolf Grimm, Paul Julienne, and Eite Tiesinga: *Feshbach resonances in ultracold gases*. Rev. Mod. Phys., 82:1225–1286, Apr 2010. <http://link.aps.org/doi/10.1103/RevModPhys.82.1225>.

- [80] Phillips, William D.: *Nobel lecture: Laser cooling and trapping of neutral atoms*. Rev. Mod. Phys., 70:721–741, Jul 1998. <http://link.aps.org/doi/10.1103/RevModPhys.70.721>.
- [81] Metcalf, H.J. and P. van der Straten: *Laser Cooling and Trapping*. Graduate Texts in Contemporary Physics. Springer New York, 2001, ISBN 9780387987286. <https://books.google.co.uk/books?id=i-40VaXqrj0C>.
- [82] Haubrich, D., A. Höpe, and D. Meschede: *A simple model for optical capture of atoms in strong magnetic quadrupole fields*. Optics Communications, 102(3):225 – 230, 1993, ISSN 0030-4018. <http://www.sciencedirect.com/science/article/pii/003040189390387K>.
- [83] Greiner, Markus, Immanuel Bloch, Theodor W. Hänsch, and Tilman Esslinger: *Magnetic transport of trapped cold atoms over a large distance*. Phys. Rev. A, 63:031401, Feb 2001. <http://link.aps.org/doi/10.1103/PhysRevA.63.031401>.
- [84] Nakagawa, K., Y. Suzuki, M. Horikoshi, and J.B. Kim: *Simple and efficient magnetic transport of cold atoms using moving coils for the production of bose-einstein condensation*. Applied Physics B, 81(6):791–794, 2005, ISSN 1432-0649. <http://dx.doi.org/10.1007/s00340-005-1953-8>.
- [85] Ludlow, Andrew D., Martin M. Boyd, Jun Ye, E. Peik, and P. O. Schmidt: *Optical atomic clocks*. Rev. Mod. Phys., 87:637–701, Jun 2015. <http://link.aps.org/doi/10.1103/RevModPhys.87.637>.
- [86] Blakestad, R. B, C. Ospelkaus, A. P VanDevender, J. H Wesenberg, M. J Biercuk, D. Leibfried, and D. J Wineland: *Near-ground-state transport of trapped-ion qubits through a multidimensional array*. Phys. Rev. A, 84:032314, Sep 2011. <http://link.aps.org/doi/10.1103/PhysRevA.84.032314>.
- [87] Geremia, J. M., John K. Stockton, and Hideo Mabuchi: *Tensor polarizability and dispersive quantum measurement of multilevel atoms*. Phys. Rev. A, 73:042112, Apr 2006. <http://link.aps.org/doi/10.1103/PhysRevA.73.042112>.
- [88] Smith, A, B E Anderson, S Chaudhury, and P S Jessen: *Three-axis measurement and cancellation of background magnetic fields to less than 50 μ g in a cold atom experiment*. Journal of Physics B: Atomic, Molecular and Optical Physics, 44(20):205002, 2011. <http://stacks.iop.org/0953-4075/44/i=20/a=205002>.
- [89] Dedman, C. J., R. G. Dall, L. J. Byron, and A. G. Truscott: *Active cancellation of stray magnetic fields in a bose-einstein condensation experiment*. Review of Scientific Instruments, 78(2), 2007. <http://scitation.aip.org/content/aip/journal/rsi/78/2/10.1063/1.2472600>.
- [90] GmbH, Sekels: *Magnetische Abschirmungen*, 2016. http://www.sekels.de/fileadmin/PDF/Deutsch/30_Broschuere_Magnetische_Abschirmungen.pdf, Accessed 2016-09-02.

-
- [91] Affolderbach, Christoph: *Dark State Magnetometers and Gradiometers*. PhD thesis, Universität Bonn, 2002.
- [92] Sabulsky, Dylan O., Colin V. Parker, Nathan D. Gemelke, and Cheng Chin: *Efficient continuous-duty bitter-type electromagnets for cold atom experiments*. Review of Scientific Instruments, 84(10), 2013. <http://scitation.aip.org/content/aip/journal/rsi/84/10/10.1063/1.4826498>.
- [93] Ricci, Leonardo, Luca Matteo Martini, Matteo Franchi, and Andrea Bertoldi: *A current-carrying coil design with improved liquid cooling arrangement*. Review of Scientific Instruments, 84(6), 2013. <http://scitation.aip.org/content/aip/journal/rsi/84/6/10.1063/1.4811666>.
- [94] Martines Dorantes, Miguel: *Non-destructive internal state detection of a small atomic ensemble of neutral atoms*. PhD thesis, Universität Bonn, 2016.
- [95] Schilling, Volker: *A magnetic elevator for neutral atoms into a 2d state-dependent optical lattice experiment*. Master's thesis, Universität Bonn, 2015.
- [96] Meyrath, T. P.: *Electromagnet design basics for cold atom experiments*, 2003.
- [97] Raab, E. L., M. Prentiss, Alex Cable, Steven Chu, and D. E. Pritchard: *Trapping of neutral sodium atoms with radiation pressure*. Phys. Rev. Lett., 59:2631–2634, Dec 1987. <http://link.aps.org/doi/10.1103/PhysRevLett.59.2631>.
- [98] Steck, DA: *Cesium D line data*. Los Alamos Natl. Lab., 2010. <http://steck.us/alkalidata>.
- [99] Alt, Wolfgang: *Optical control of single neutral atoms*. PhD thesis, Universität Bonn, 2004.
- [100] Baillard, X., A. Gauguet, S. Bize, P. Lemonde, Ph. Laurent, A. Clairon, and P. Rosenbusch: *Interference-filter-stabilized external-cavity diode lasers*. Optics Communications, 266(2):609 – 613, 2006, ISSN 0030-4018. <http://www.sciencedirect.com/science/article/pii/S0030401806004561>.
- [101] Thompson, Daniel J. and Robert E. Scholten: *Narrow linewidth tunable external cavity diode laser using wide bandwidth filter*. Review of Scientific Instruments, 83(2), 2012. <http://scitation.aip.org/content/aip/journal/rsi/83/2/10.1063/1.3687441>.
- [102] Ricci, L., M. Weidemüller, T. Esslinger, A. Hemmerich, C. Zimmermann, V. Vuletic, W. König, and T.W. Hänsch: *A compact grating-stabilized diode laser system for atomic physics*. Optics Communications, 117(5):541 – 549, 1995, ISSN 0030-4018. <http://www.sciencedirect.com/science/article/pii/S003040189500146Y>.
- [103] Reimann, Rene: *Cooling and Cooperative Coupling of Single Atoms in an Optical Cavity*. PhD thesis, Universität Bonn, 2014.

- [104] Harris, M. L., C. S. Adams, S. L. Cornish, I. C. McLeod, E. Tarleton, and I. G. Hughes: *Polarization spectroscopy in rubidium and cesium*. Phys. Rev. A, 73:062509, Jun 2006. <http://link.aps.org/doi/10.1103/PhysRevA.73.062509>.
- [105] Wieman, C. and T. W. Hänsch: *Doppler-free laser polarization spectroscopy*. Phys. Rev. Lett., 36:1170–1173, May 1976. <http://link.aps.org/doi/10.1103/PhysRevLett.36.1170>.
- [106] Bauer, Michael, Philipp Pierre Franzreb, Nicolas Spethmann, and Artur Widera: *Note: Reliable low-vibration piezo-mechanical shutter*. Review of Scientific Instruments, 85(9), 2014. <http://scitation.aip.org/content/aip/journal/rsi/85/9/10.1063/1.4894205>.
- [107] Meschede, D.: *Optik, Licht und Laser*. Lehrbuch Physik. Teubner, 2005, ISBN 9783519132486.
- [108] Flemming, J., A.M. Tuboy, D.M.B.P. Milori, L.G. Marcassa, S.C. Zilio, and V.S. Bagnato: *Magneto-optical trap for sodium atoms operating on the d1 line*. Optics Communications, 135(4):269 – 272, 1997, ISSN 0030-4018. <http://www.sciencedirect.com/science/article/pii/S0030401896006608>.
- [109] Marcassa, L G, K Helmersson, A M Tuboy, D M B P Milori, S R Muniz, J Flemming, S C Zilio, and V S Bagnato: *Collisional loss rate of sodium atoms in a magneto-optical trap operating on the d1 line*. Journal of Physics B: Atomic, Molecular and Optical Physics, 29(14):3051, 1996. <http://stacks.iop.org/0953-4075/29/i=14/a=017>.
- [110] Wu, Saijun, Thomas Plisson, Roger C. Brown, William D. Phillips, and J. V. Porto: *Multiphoton magneto-optical trap*. Phys. Rev. Lett., 103:173003, Oct 2009. <http://link.aps.org/doi/10.1103/PhysRevLett.103.173003>.
- [111] Yang, Baodong, Qiangbing Liang, Jun He, and Junmin Wang: *Background-free fluorescence detection of cold atoms in a two-color magneto-optical trap*. Opt. Express, 20(11):11944–11952, May 2012. <http://www.opticsexpress.org/abstract.cfm?URI=oe-20-11-11944>.
- [112] Arpornthip, T., C. A. Sackett, and K. J. Hughes: *Vacuum-pressure measurement using a magneto-optical trap*. Phys. Rev. A, 85:033420, Mar 2012. <http://link.aps.org/doi/10.1103/PhysRevA.85.033420>.
- [113] Grimm, Rudolf, Matthias Weidemüller, and Yurii B. Ovchinnikov: *Optical dipole traps for neutral atoms*. Advances In Atomic, Molecular, and Optical Physics, 42:95 – 170, 2000. <http://www.sciencedirect.com/science/article/pii/S1049250X0860186X>.
- [114] Schrader, D., S. Kuhr, W. Alt, M. Müller, V. Gomer, and D. Meschede: *An optical conveyor belt for single neutral atoms*. Appl. Phys. B, 73:819, 2001.

-
- [115] Thompson, Russell E., Daniel R. Larson, and Watt W. Webb: *Precise nanometer localization analysis for individual fluorescent probes*. Biophysical Journal, 82(5):2775 – 2783, 2002, ISSN 0006-3495. <http://www.sciencedirect.com/science/article/pii/S000634950275618X>.
- [116] Barredo, Daniel, Sylvain de Léséleuc, Vincent Lienhard, Thierry Lahaye, and Antoine Browaeys: *An atom-by-atom assembler of defect-free arbitrary 2d atomic arrays*, 2016.
- [117] Endres, Manuel, Hannes Bernien, Alexander Keesling, Harry Levine, Eric R. Anschuetz, Alexandre Krajenbrink, Crystal Senko, Vladan Vuletic, Markus Greiner, and Mikhail D. Lukin: *Cold matter assembled atom-by-atom*, 2016.
- [118] Kleiβler, Felix: *Assembly and characterization of a high numerical aperture microscope for single atoms*. Master's thesis, Universität Bonn, 2014.
- [119] Epoxy Technology, Inc., 14 Fortune Drive, Billerica, MA 01821-3972: *Epo-Tek H77 Technical Data Sheet*, Apr 2010.
- [120] AZoNetwork Ltd.: *Alumina - aluminium oxide - al_2o_3 - a refractory ceramic oxide*, 2001. <http://www.azom.com/article.aspx?ArticleID=52>.
- [121] Robens, Carsten, Stefan Brakhane, Wolfgang Alt, Felix Kleiβler, Geol Moon, Gautam Ramola, Dieter Meschede, and Andrea Alberti: *A high-numerical-aperture ($na = 0.92$) microscope objective for optical imaging and addressing of cold atoms*. in preparation, 2016.
- [122] Juškaitis, Rimas: *Measuring the Real Point Spread Function of High Numerical Aperture Microscope Objective Lenses*, pages 239–250. Springer US, Boston, MA, 2006, ISBN 978-0-387-45524-2. http://dx.doi.org/10.1007/978-0-387-45524-2_11.
- [123] Obermüller, Christian and Khaled Karrai: *Far field characterization of diffracting circular apertures*. Applied Physics Letters, 67(23):3408–3410, 1995. <http://scitation.aip.org/content/aip/journal/apl/67/23/10.1063/1.115262>.
- [124] Sheppard, C.J.R. and Min Gu: *Imaging by a high aperture optical system*. Journal of Modern Optics, 40(8):1631–1651, 1993. <http://dx.doi.org/10.1080/09500349314551641>.
- [125] Coherent, Inc.: *Efficient transformation of gaussian beams into uniform, rectangular intensity distributions*. http://www.coherent.com/downloads/Transformation_GaussianBeams.pdf. Accessed: 2016-07-27.
- [126] Karski, M., L. Förster, J. M. Choi, W. Alt, A. Widera, and D. Meschede: *Nearest-neighbor detection of atoms in a 1d optical lattice by fluorescence imaging*. Phys. Rev. Lett., 102:053001, Feb 2009. <http://link.aps.org/doi/10.1103/PhysRevLett.102.053001>.

- [127] Ashida, Yuto and Masahito Ueda: *Precise multi-emitter localization method for fast super-resolution imaging*. Opt. Lett., 41(1):72–75, Jan 2016. <http://ol.osa.org/abstract.cfm?URI=ol-41-1-72>.
- [128] Nelson, Karl D., Xiao Li, and David S. Weiss: *Imaging single atoms in a three-dimensional array*. Nat Phys, 3(8):556–560, 2007. <http://dx.doi.org/10.1038/nphys645>.
- [129] Neuzner, A., M. Körber, O. Morin, S. Ritter, and G. Rempe: *Interference and dynamics of light from a distance-controlled atom pair in an optical cavity*. Nat. Photonics, pages 303–306, 2016. <http://dx.doi.org/10.1038/nphoton.2016.19>.
- [130] Natan, Adi: *Fast 2d peak finder*. <https://www.mathworks.com/matlabcentral/fileexchange/37388-fast-2d-peak-finder>, 2012. Accessed: 2016-07-31.
- [131] Zhang, Bo, Josiane Zerubia, and Jean Christophe Olivo-Marin: *Gaussian approximations of fluorescence microscope point-spread function models*. Appl. Opt., 46(10):1819–1829, Apr 2007. <http://ao.osa.org/abstract.cfm?URI=ao-46-10-1819>.
- [132] Preiss, Philipp M., Ruichao Ma, M. Eric Tai, Jonathan Simon, and Markus Greiner: *Quantum gas microscopy with spin, atom-number, and multilayer readout*. Phys. Rev. A, 91:041602, Apr 2015. <http://link.aps.org/doi/10.1103/PhysRevA.91.041602>.
- [133] Lee, P. J., M. Anderlini, B. L. Brown, J. Sebby-Strabley, W. D. Phillips, and J. V. Porto: *Sublattice addressing and spin-dependent motion of atoms in a double-well lattice*. Phys. Rev. Lett., 99:020402, Jul 2007. <http://link.aps.org/doi/10.1103/PhysRevLett.99.020402>.
- [134] Lee, J. H., E. Montano, I. H. Deutsch, and P. S. Jessen: *Robust site-resolvable quantum gates in an optical lattice via inhomogeneous control*. Nat Commun, 2013. <http://dx.doi.org/10.1038/ncomms3027>.
- [135] Weitenberg, Christof, Manuel Endres, Jacob F. Sherson, Marc Cheneau, Peter Schausz, Takeshi Fukuhara, Immanuel Bloch, and Stefan Kuhr: *Single-spin addressing in an atomic mott insulator*. Nature, 471(7338):319–324, Mar 2011, ISSN 0028-0836. <http://dx.doi.org/10.1038/nature09827>.
- [136] Zhang, Chuanwei, S. L. Rolston, and S. Das Sarma: *Manipulation of single neutral atoms in optical lattices*. Phys. Rev. A, 74:042316, Oct 2006. <http://link.aps.org/doi/10.1103/PhysRevA.74.042316>.
- [137] Wang, Yang, Xianli Zhang, Theodore A. Corcovilos, Aishwarya Kumar, and David S. Weiss: *Coherent addressing of individual neutral atoms in a 3d optical lattice*. Phys. Rev. Lett., 115:043003, Jul 2015. <http://link.aps.org/doi/10.1103/PhysRevLett.115.043003>.

-
- [138] Xia, T., M. Lichtman, K. Maller, A. W. Carr, M. J. Piotrowicz, L. Isenhower, and M. Saffman: *Randomized benchmarking of single-qubit gates in a 2d array of neutral-atom qubits*. Phys. Rev. Lett., 114:100503, Mar 2015. <http://link.aps.org/doi/10.1103/PhysRevLett.114.100503>.
- [139] Omran, Ahmed, Martin Boll, Timon A. Hilker, Katharina Kleinlein, Guillaume Salomon, Immanuel Bloch, and Christian Gross: *Microscopic observation of pauli blocking in degenerate fermionic lattice gases*. Phys. Rev. Lett., 115:263001, Dec 2015. <http://link.aps.org/doi/10.1103/PhysRevLett.115.263001>.
- [140] Pavani, Sri Rama Prasanna, Michael A. Thompson, Julie S. Biteen, Samuel J. Lord, Na Liu, Robert J. Twieg, Rafael Piestun, and W. E. Moerner: *Three-dimensional, single-molecule fluorescence imaging beyond the diffraction limit by using a double-helix point spread function*. Proceedings of the National Academy of Sciences, 106(9):2995–2999, 2009. <http://www.pnas.org/content/106/9/2995.abstract>.
- [141] Pavani, Sri Rama Prasanna and Rafael Piestun: *Three dimensional tracking of fluorescent microparticles using a photon-limited double-helix response system*. Opt. Express, 16(26):22048–22057, Dec 2008. <http://www.opticsexpress.org/abstract.cfm?URI=oe-16-26-22048>.
- [142] Bloch, Immanuel: *Ultracold quantum gases in optical lattices*. Nat Phys, 1(1):23–30, Oct 2005, ISSN 1745-2473. <http://dx.doi.org/10.1038/nphys138>.
- [143] DePue, Marshall T., Colin McCormick, S. Lukman Winoto, Steven Oliver, and David S. Weiss: *Unity occupation of sites in a 3d optical lattice*. Phys. Rev. Lett., 82:2262–2265, Mar 1999. <http://link.aps.org/doi/10.1103/PhysRevLett.82.2262>.
- [144] Bishop, C.M.: *Pattern Recognition and Machine Learning*. Information Science and Statistics. Springer, 2006, ISBN 9780387310732. <https://books.google.de/books?id=kTNoQgAACAAJ>.
- [145] Belmechri, N., L. Förster, W. Alt, A. Widera, D. Meschede, and A. Alberti: *Microwave control of atomic motional states in a spin-dependent optical lattice*. J. Phys. B: At. Mol. Opt. Phys., 46:104006, 2013.
- [146] Bjorkholm, J. E.: *Collision-limited lifetimes of atom traps*. Phys. Rev. A, 38:1599–1600, Aug 1988. <http://link.aps.org/doi/10.1103/PhysRevA.38.1599>.
- [147] Mandel, Olaf, Markus Greiner, Artur Widera, Tim Rom, Theodor W. Hänsch, and Immanuel Bloch: *Coherent transport of neutral atoms in spin-dependent optical lattice potentials*. Phys. Rev. Lett., 91:010407, Jul 2003. <http://link.aps.org/doi/10.1103/PhysRevLett.91.010407>.
- [148] Lühmann, Dirk Sören, Ole Jürgensen, Malte Weinberg, Juliette Simonet, Parvis Soltan-Panahi, and Klaus Sengstock: *Quantum phases in tunable state-dependent hexagonal optical lattices*. Phys. Rev. A, 90:013614, Jul 2014. <http://link.aps.org/doi/10.1103/PhysRevA.90.013614>.

- [149] Shankar, R.: *Principles of Quantum Mechanics*. Springer, 1994, ISBN 9780306447907.
- [150] Messiah, A.: *Quantum mechanics*, volume 2 of *Quantum Mechanics*. North-Holland Pub. Co., 1962. <https://books.google.de/books?id=8LPvAAAAMAAJ>.
- [151] Schrader, D.: *A Neutral Atom Quantum Register*. PhD thesis, Universität Bonn, 2004.
- [152] Döring, D.: *Ein Experiment zum zustandsabhängigen Transport einzelner Atome*. Master's thesis, Universität Bonn, 2007.
- [153] McKeever, J., J. R. Buck, A. D. Boozer, A. Kuzmich, H. C. Nägerl, D. M. Stamper-Kurn, and H. J. Kimble: *State-insensitive cooling and trapping of single atoms in an optical cavity*. Phys. Rev. Lett., 90:133602, Apr 2003. <http://link.aps.org/doi/10.1103/PhysRevLett.90.133602>.
- [154] Safronova, M. S., U. I. Safronova, and Charles W. Clark: *Magic wavelengths for optical cooling and trapping of lithium*. Phys. Rev. A, 86:042505, Oct 2012. <http://link.aps.org/doi/10.1103/PhysRevA.86.042505>.
- [155] Goldschmidt, E. A., D. G. Norris, S. B. Koller, R. Wyllie, R. C. Brown, J. V. Porto, U. I. Safronova, and M. S. Safronova: *Magic wavelengths for the $5s \sim 18s$ transition in rubidium*. Phys. Rev. A, 91:032518, Mar 2015. <http://link.aps.org/doi/10.1103/PhysRevA.91.032518>.
- [156] Bergmann, Klaas, Nikolay V. Vitanov, and Bruce W. Shore: *Perspective: Stimulated raman adiabatic passage: The status after 25 years*. The Journal of Chemical Physics, 142(17), 2015. <http://scitation.aip.org/content/aip/journal/jcp/142/17/10.1063/1.4916903>.
- [157] Negretti, A., T. Calarco, J. Zopes, C. Robens, W. Alt, D. Meschede, and A. Alberti: *Optimal control analysis for fast state-dependent transport of neutral atoms*. in preparation, 2016.
- [158] Kobayakov, Andrey, Michael Sauer, and Dipak Chowdhury: *Stimulated brillouin scattering in optical fibers*. Adv. Opt. Photon., 2(1):1–59, Mar 2010. <http://aop.osa.org/abstract.cfm?URI=aop-2-1-1>.
- [159] Kittel, Charles: *Introduction to Solid State Physics*. John Wiley & Sons, Inc., 6th edition, 1986.
- [160] Windpassinger, Patrick and Klaus Sengstock: *Engineering novel optical lattices*. Reports on Progress in Physics, 76(8):086401, 2013. <http://stacks.iop.org/0034-4885/76/i=8/a=086401>.
- [161] Werner, R.: *Notes on: Spin dependent transport in 2d optical lattices*. unpublished, 2012.

-
- [162] Förster, Leonid, Michał Karski, Jai Min Choi, Andreas Steffen, Wolfgang Alt, Dieter Meschede, Artur Widera, Enrique Montano, Jae Hoon Lee, Worawarong Rakreungdet, and Poul S. Jessen: *Microwave control of atomic motion in optical lattices*. Phys. Rev. Lett., 103:233001, Dec 2009. <http://link.aps.org/doi/10.1103/PhysRevLett.103.233001>.
- [163] Hambitzer, A.: *Direct synthesis of light polarization for state-dependent transport*. Master's thesis, Universität Bonn, 2012.
- [164] Kuhr, Stefan: *A controlled quantum system of individual neutral atoms*. PhD thesis, Universität Bonn, 2003.
- [165] Robens, Carsten, Jonathan Zopes, Wolfgang Alt, Stefan Brakhane, Dieter Meschede, and Andrea Alberti: *Low-entropy states of neutral atoms in polarization-synthesized optical lattices*, 2016.
- [166] Lee, H. J., C. S. Adams, M. Kasevich, and S. Chu: *Raman cooling of atoms in an optical dipole trap*. Phys. Rev. Lett., 76:2658–2661, Apr 1996. <http://link.aps.org/doi/10.1103/PhysRevLett.76.2658>.
- [167] Perrin, H., A. Kuhn, I. Bouchoule, and C. Salomon: *Sideband cooling of neutral atoms in a far-detuned optical lattice*. EPL (Europhysics Letters), 42(4):395, 1998. <http://stacks.iop.org/0295-5075/42/i=4/a=395>.
- [168] Li, Xiao, Theodore A. Corcovilos, Yang Wang, and David S. Weiss: *3d projection sideband cooling*. Phys. Rev. Lett., 108:103001, Mar 2012. <http://link.aps.org/doi/10.1103/PhysRevLett.108.103001>.
- [169] Sajid, Muhammad, Pablo Arnault, Rheinhard F. Werner, Dieter Meschede, and Andrea Alberti: *Topological edge modes of discrete-time quantum walks in synthetic magnetic fields*. in preparation, 2016.
- [170] Wosnitza, J., A.D. Bianchi, J. Freudenberger, J. Haase, T. Herrmannsdörfer, N. Kozlova, L. Schultz, Y. Skourski, S. Zherlitsyn, and S.A. Zvyagin: *Dresden pulsed magnetic field facility*. Journal of Magnetism and Magnetic Materials, 310(2, Part 3):2728 – 2730, 2007, ISSN 0304-8853. <http://www.sciencedirect.com/science/article/pii/S0304885306021731>, Proceedings of the 17th International Conference on Magnetism The International Conference on Magnetism.
- [171] Ku, H. H.: *Notes on the use of propagation of error formulas*. Journal of Research of the National Bureau of Standards. Section C: Engineering and Instrumentation, 70C(4):263–273, October 1966, ISSN 0022-4316.
- [172] Geary, R. C.: *The frequency distribution of the quotient of two normal variates*. Journal of the Royal Statistical Society, 93(3):442–446, 1930, ISSN 09528385. <http://www.jstor.org/stable/2342070>.
- [173] Ogilvie, J. F.: *A monte-carlo approach to error propagation*. Computers & Chemistry, 8(3):205 – 207, 1984, ISSN 0097-8485. <http://www.sciencedirect.com/science/article/pii/0097848584800078>.

- [174] Robens, Carsten and Stefan Brakhane: *Monte carlo error propagation*. <http://www.mathworks.com/matlabcentral/fileexchange/57672-monte-carlo-error-propagation>, 2016. Accessed: 2016-06-16.
- [175] Debian: *Debian — the universal operating system*. <https://www.debian.org/>. Accessed: 2016-06-16.
- [176] VirtualBox: *Virtual machines*. <https://www.virtualbox.org/wiki/Virtualization>. Accessed: 2016-06-16.
- [177] Wikipedia: *Virtualization — wikipedia, the free encyclopedia*, 2016. <https://en.wikipedia.org/w/index.php?title=Virtualization&oldid=721688053>, Accessed 2016-06-16.
- [178] The Tornado Authors: *Tornado — a python web framework and asynchronous networking library*. <http://www.tornadoweb.org/>. Accessed: 2016-06-17.
- [179] The Apache Software Foundation: *The apache http server project*. <https://httpd.apache.org/>. Accessed: 2016-06-17.
- [180] PHP: *PHP — a general-purpose scripting language*. <http://www.php.net>. Accessed: 2016-06-17.
- [181] Oracle Corporation: *MySQL — the world's most popular open source database*. <https://httpd.apache.org/>. Accessed: 2016-06-17.
- [182] Dygraphs: *Dygraphs — a fast, flexible open source javascript charting library*. <http://dygraphs.com/>. Accessed: 2016-09-05.
- [183] Linear Technology Corporation: *Ltc2054 ultra-precision, wide dynamic range 10hz bandwidth photodiode amplifier*. <http://www.linear.com/solutions/1209>. Accessed: 2016-06-18.
- [184] Tietze, Ulrich, Christoph Schenk, and Eberhard Gamm: *Halbleiter - Schaltungstechnik. Neuer Teil: Nachrichtentechnische Schaltungen*. Springer, Berlin, 14. auflage edition, 2012, ISBN 978-3-642-31025-6.
- [185] ARM Ltd.: *Arm mbed iot device platform*. <https://www.mbed.com/en/>. Accessed: 2016-06-18.
- [186] Wikipedia: *Websocket — wikipedia, the free encyclopedia*, 2016. <https://en.wikipedia.org/w/index.php?title=WebSocket&oldid=725645473>, Accessed 2016-06-18.
- [187] Varian Vacuum Technologies, 121 Hartwell Avenue, Lexington, Massachusetts 02421: *Multi-Gauge Controller – Instruction Manual*, w edition, February 2001.
- [188] Shestovyy, S.: *Entwicklung eines hochstabilen optischen Phasendetektors für Licht-Polarisationssynthese*. Master's thesis, Universität Bonn, 2014.

Danksagung

Mein Dank ist an diejenigen Menschen gerichtet, ohne die ein derart zeitaufwendiges Projekt nicht möglich gewesen wäre: Ich danke meiner Familie für den Rückhalt über die ganzen letzten Jahre - im Besonderen meiner Frau Almut, die mich immer wieder aufgebaut hat, meiner kleinen Tochter Pia, die charmant aufzeigt, dass es möglicherweise auch ein Leben außerhalb der Physik geben kann, und meinen Eltern.

Weiterhin gilt ein sehr großer Dank Herrn Prof. Dr. Meschede für die Möglichkeit meine Arbeit an einem sehr interessanten Experiment in seiner Forschungsgruppe anfertigen zu können. Im Besonderen bin ich ihm für die ermöglichte außergewöhnliche Flexibilität in einer schwierigen Zeit dankbar. Ebenso danke ich Herrn Prof. Dr. Linden für die Übernahme des Zweitgutachtens. Der Bonn-Cologne Graduate School danke ich für die finanzielle Unterstützung. Mein Dank geht ebenfalls an Andrea Alberti mit seinem tiefgreifenden Verständnis für theoretische Physik und seiner großartigen Beharrlichkeit im Hinblick auf eine weitere Verwertung der Glaszelle. Mit seiner technischen und physikalischen Expertise hat Wolfgang Alt entscheidend zum Gelingen dieser Arbeit beigetragen. Mit Carsten Robens verbindet mich eine lange sowohl konstruktive als auch freundschaftliche Zusammenarbeit über einen wesentlichen Zeitraum dieser Arbeit - im Besonderen bezüglich des Objektivs und diverser sehr bedeutender Subprojekte elektronischer Natur. I thank Geol Moon for his endless efforts on realizing this cold atom lattice experiment and the current team of the experiment: Gautam Ramola and Max Werninghaus.

Außerdem sei den aktuellen und ehemaligen Mitgliedern der Arbeitsgruppe Meschede für eine nette Arbeitsatmosphäre gedankt. Ich erinnere mich gerne an die abendlichen Nerf-Schlachten und Gaming-Sessions in unserem Büro. Mit Jose Gallego Fernández, René Reimann, Miguel Martinez-Dorantes gab es daneben immer Gelegenheit wichtige Dinge auszudiskutieren um mit neuen Ideen voranzuschreiten.

Stefanie Bauer, Jose Gallego-Fernández, Miguel Martinez-Dorantes, René Reimann, Gautam Ramola, Max Werninghaus, Geol Moon, Felix Kleißler, Wolfgang Alt und Andrea Alberti sei für ihre Anmerkungen zu dieser Arbeit gedankt.

Ein experimenteller Aufbau ist immer mit Versuchen und Fehlschlägen verbunden um Neues zu erreichen. Bei diesem Unterfangen wurde ich freundlicherweise unterstützt von der Arbeitsgruppe von Prof. Dr. Linden (Physikalisches Institut) und Herr Kant (HISKP) mit Goldbeschichtungen sowie Johannes Overbuschmann und Angelika Sehrbrock (beide vom Institut Caesar) mit Goldbeschichtungen und Nanolöchern. Der Zusammenbau des Objektivs und eine erste Charakterisierung im Reinraum wurde ermöglicht durch Sigfried Steltenkamp, Peter Schoslik, Sam Schmitz und Georg Siebke vom Institut Caesar. Der Zusammenbau der Glaszelle und das Ausglühen der Vakuumteile wären ohne die Öfen von Herrn Brock (Physikalisches Institut) unmöglich gewesen. Ihnen allen sei hiermit herzlichst gedankt. Ein weiterer Dank gilt Herrn Prof. Dr. Köhl für ein Ersatzvakuumeckventil, ohne welches wir unsere Leckage erst nach zwei Monaten in den Griff bekommen hätten. Sowie der Arbeitsgruppe Weitz für diverse Vakuumteile einer Testkammer. Im Rahmen dieser Arbeit wurden zahlreiche Aufträge mitsamt schnell zu erledigender Sonderwünsche an die Werkstätten der Universität vergeben: Hier sei den aktuellen und ehemaligen Mitarbeitern der hauseigenen Elektronik- und Feinmechanikwerkstatt, für eine (meistens) zügige Bearbeitung gedankt. Auch geht mein Dank an die

Zentralwerkstatt der Physik für diverse Halbwerkzeuge, der Feinmechanikwerkstatt IAP für Kühlplatten, der Glasbläserei des Chemischen Instituts für verschiedene Glasarbeiten, der Werkstatt der Physikalischen Chemie für die Benutzung eines Hochtemperaturofens, dem Oberflächenlabor des Physikalischen Instituts für Glasteile eines ersten Prototyps der Glaszelle sowie dem Schreiner des Physikalischen Instituts Herrn Lenz.

Während dieser Arbeit hatte ich zusätzlich das Vergnügen Sebastian Arnold, Martin Link, Simon Reichelt, Weiqi Thou, Jana Huisman, Felix Kleißler, Stanislav Shestovy, Jonathan Zopes, Isabelle Boventer, Volker Schilling und Max Werninghaus betreuen zu dürfen.

Eidesstattliche Erklärung

Diese Dissertation wurde im Sinne der Promotionsordnung vom 17.06.2011 am Institut für Angewandte Physik der Universität Bonn unter der Leitung von Prof. Dr. Dieter Meschede angefertigt. Hiermit versichere ich, dass ich die vorgelegte Arbeit selbständig verfasst und keine anderen als die angegebenen Quellen und Hilfsmittel benutzt sowie die Zitate kenntlich gemacht habe.

Ort, Datum

Stefan Brakhane

Lebenslauf

Persönliche Daten

Name: Stefan Brakhane
Geburtsdatum: 1985-10-15
Geburtsort: Bad Driburg

Schule

Juni 2005 Abitur (Note 1,2)
1996 – 2005 Gymnasium St. Xaver, Bad Driburg
1992 – 1996 Kath. Grundschule Bad Driburg

Studium

seit 2011-05-30 Doktorarbeit am Institut für Angewandte Physik der Universität Bonn in der Arbeitsgruppe von Prof. Dr. Dieter Meschede
Okt. 2005 – Studium der Physik an der Rheinischen Friedrich-Wilhelms-Universität Bonn
Jan. 2011 Diplomarbeit in der Arbeitsgruppe von Prof. Dr. Meschede
Thema: „Kontrolle der Atom-Resonator Wechselwirkung mit Hilfe einer Regelschleife“

Stipendien und Förderungen

2012 – 2014 Teilstipendium der Bonn-Cologne Graduate School of Physics and Astronomy (Honors Program)

Veröffentlichungen

- C. Robens, J. Zopes, W. Alt, S. Brakhane, D. Meschede, A. Alberti, *Low-entropy states of neutral atoms in polarization-synthesized optical lattices*, arXiv:1608.02410
- T. Groh, S. Brakhane, W. Alt, D. Meschede, J. Asbóth and A. Alberti, *Robustness of topologically protected edge states in quantum walk experiments with neutral atoms*, Physical Review A **94**, 013620 (2016)
- A. Alberti, C. Robens, W. Alt, S. Brakhane, M. Karski, R. Reimann, A. Widera and D. Meschede, *Super-resolution microscopy of single atoms in optical lattices*, New J. Phys., (2016)
- S. Brakhane, W. Alt, D. Meschede, C. Robens, G. Moon and A. Alberti, *Ultra-low birefringence dodecagonal vacuum glass cell*, Rev. Sci. Instrum. **86**, 126108 (2015)
- S. Brakhane, W. Alt, D. Meschede, C. Robens and A. Alberti, *Polarisationserhaltende Vakuum-Zelle zur Anwendung oder Messung elektromagnetischer Wellen im Vakuum*, zum Patent angemeldet, (2015)

- C. Robens, S. Brakhane, D. Meschede and A. Alberti, *Quantum Walks With Neutral Atoms: Quantum Interference Effects of One and Two Particles*, Proceedings of the XXII International Conference ICOLS, (2015)
- S. Brakhane, W. Alt, K. Kampschulte, M. Martinez-Dorantes, R. Reimann, S. Yoon, A. Widera, D. Meschede, *Bayesian Feedback Control of a Two-Atom Spin-State in an Atom-Cavity System*, Phys. Rev. Lett. **109**, 173601 (2012)
- T. Kampschulte, W. Alt, S. Brakhane, M. Eckstein, R. Reimann, A. Widera, and D. Meschede, *Optical control of the refractive index of a single atom*, Phys. Rev. Lett. **105**, 153603 (2010)